Behaviour of fracture process zones in concrete influenced by simultaneously applied normal and shear displacements

Hassanzadeh, Manouchehr

1992

Division of Building Materials

Lund Institute of Technology

Behaviour of fracture process zones in concrete influenced by simultaneously applied normal and shear displacements

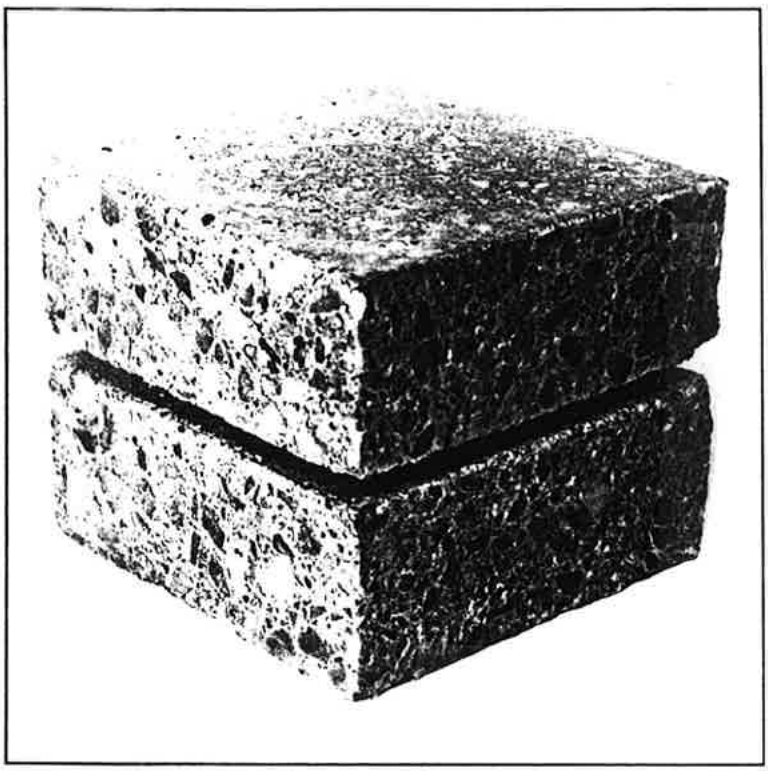

Manouchehr Hassanzadeh

Report TVBM - 1010

Lund Sweden 1992

CODEN: LUTVDG/(TVBM-1010)/1-105/(1992)

Behaviour of fracture process zones in concrete influenced by simultaneously applied normal and shear displacements

Manouchehr Hassanzadeh

To Farzad

Preface

This investigation has been carried out at the Division of Building Materials at the Lund Institute of Technology in Lund, Sweden, and has been financially supported by grants from the Swedish Board for Technical Development and the Foundation for Swedish Concrete Research.

I wish to express my gratitude to Professor Arne Hillerborg for his valuable guidance and encouragement throughout the course of my education and this investigation. I also wish to express my gratitude to his successor, Professor Göran Fagerlund, who has facilitated my work.

I wish to thank all the members of the Division of Building Materials, especially Britt Andersson, Bo Johansson, Lars Boström and Per Johan Gustafsson (former member) for their help during this work.

In addition, I wish to express my gratitude to the members of the Laurell family for helping me to feel at home in Swedish society.

Lund, October 1991

Manouchehr Hassanzadeh

Contents

Notations

All symbols are explained where they first appear. However, some symbols will briefly be presented here.

A	Area of the cross section of the specimen
A_0	Area of the fracture surface
A_x	Contact surface between matrix and aggregates projected on xz-plane
A_y	Contact surface between matrix and aggregates projected on yz-plane
a	Crack length
b	Width of the specimen
b_0	Width of the specimen excluding notches
C_{ij}	Elements of the stiffness matrix of the fracture process zone
D	Size of aggregate, diameter
D_{max}	Maximum aggregate size, maximum diameter
d	Width of the specimen
d_0	Width of the specimen excluding notches
E	Modulus of elasticity
f_t	Tensile strength
f_c	Compressive strength
G	Energy release rate
G_c	Critical energy release rate
G_F	Fracture energy
h	Length of the specimen between supports
I	Moment of inertia of the specimen
I_0	Moment of inertia of the specimen excluding notches
K_m	Mode m stress intensity factor, m= I, II and III
K_{mc}	Critical stress intensity factor in mode m
K_e	Effective stress intensity factor
$K_{e\theta}$	Effective stress intensity factor for the cases when crack kinking occurs
L	Length of the beam
l_{ch}	Characteristic length $= EG_F/(f_t)^2$
r	Radial distance to the crack tip
S_n	Translational stiffness, spring stiffness
S_r	Rotational stiffness
w	Normal displacement within fracture process zone
w_c	Critical w
$\overline{w}$	Average w
α	Angle of inclination of the linear displacement path

β	Parabola factor for parabolic displacement path
γ	Displacement in general and total displacement, for instance sum of the displacements inside and outside of the fracture process zone
Δ	Increment
δ	Shear displacement within fracture process zone
ϵ	Strain
ϵ_0	Strain at maximum tensile stress
η	Strain energy density
η_0	Strain energy density at maximum tensile stress
θ	Angle between radial direction and x-axis
θ_0	Kink angle
μ	Coefficient of friction
σ	Normal stress
σ_{pu}	Yielding stress of matrix
σ_{rr}	Stress component in polar coordinates
$\sigma_{\theta\theta}$	Stress component in polar coordinates
τ	Shear stress
$\tau_{r\theta}$	Stress component in polar coordinates

Summary

The major goal of this investigation has been determination of the behaviour of a fracture process zone in concrete, formed under pure tensile stress conditions, which later becomes subjected to simultaneously imposed normal and shear displacements. The properties of interest are the variations of the normal and shear stresses as functions of both normal and shear displacements inside the fracture process zone. The properties and the theoretical background of the investigation are described in Chapter 2.

A test arrangement has been developed in order to accomplish the above-mentioned goal. The arrangement is capable of introducing a tensile fracture process zone and thereafter simultaneously imposing both normal and shear displacements. The arrangement is thoroughly described in Chapter 3, where the design considerations of the arrangement are also discussed. One very important matter associated with designing similar arrangements is the prevention of the "bumps" due to rotational instability of the specimens. A bump is a sudden variation of the slope of the tensile stress - displacement curve which is an indication of the uneven distribution of the normal displacement along the fracture process zone. The reason for occurrence and the consequences of a bump are discussed. In the same chapter, test methods developed by other investigators for determination of the properties of the fracture process zone under combined normal and shear displacements are presented.

In Chapter 4 the results of the tests are presented. The tests are performed in displacement control. The tests are governed by means of functions on δw-plane (δ and w are shear and normal displacements within the fracture zone), viz rates of the shear displacements are adjusted so that the relation between δ and w satisfies a function. Two types of functions have been tested, namely linear functions defined by $w=(\tan\alpha)\delta$ and parabolic functions defined by $w=\beta\delta^{1/2}$. By varying α and β a set of functions have been obtained which are denoted displacement paths. Some other complementary paths are also used in order to better understand the observed phenomena. The results of the different paths are compared with each other, which leads to the following conclusions:

Behaviour of the fracture process zone is path dependent, i.e. to approach a point on the δw-plane along two different paths leads to different stresses (both normal and shear stresses). Furthermore, the shape of the stress - displacement curves depends upon the displacement path.

The results demonstrate that in the case of $\alpha\geq75°$ and $\beta\geq0.7$ mm$^{1/2}$, the tensile stress - displacement curve (σw-curve) is not influenced by the shear and the final shear and compressive stresses are low. Furthermore, in the case of high shear rate ($d\delta/dw$), for instance $\alpha\leq30°$ the tensile normal stress decreases abruptly and

ends up as a relatively high compressive stress.

Test results show that for the cases $\alpha \leq 45°$ and $\beta \leq 0.3$ mm$^{1/2}$ the specimen in spite of the notches may include several crack systems, i.e. several fracture process zones. This event, however, confines the capacity of the testing method.

The experimental results are compared by the micro mechanical model developed by Walraven which explains some of the phenomena observed in the tests.

Finally in Chapter 4 a mathematical expression is fitted to the results of the parabolic paths, which facilitates the derivation of the required material properties. The mathematical expressions obtained in this investigation are also compared with the expressions reported by other investigators, which reveals the following:

The final stresses observed in this investigation are normally lower than those in the other investigations which, to some extent may be due to the fact that simultaneously increasing displacements leads to lower stresses compared with the case when displacements are increased one at a time, i.e. stepwise increasing displacements.

Finally Chapter 5 is dedicated to the conclusions and the future studies which the author wishes to undertake.

1 Introduction

1.1 Application of fracture mechanics to concrete

Applications of fracture mechanics to concrete have been going on since the early sixties. The applications started by introducing the linear elastic fracture mechanics models to the field of concrete. Linear elastic fracture mechanics models were the only available models which treated crack stability and crack growth in concrete until the mid-seventies when models based on tensile-softening were developed within the field of the fracture mechanics of concrete. During the eighties the tensile-softening models played a central role in the field of fracture mechanics of concrete. The major fracture mechanics research activities were aimed at further development of tensile-softening models, determination of the requisite material properties and applications of the models to structures with various geometry and size.

It has been demonstrated, see for instance Petersson 81, that propagation of a real crack in cementitious materials is preceded by formation of a tensile fracture process zone which possesses such properties that it governs the structural behaviour of concrete. Furthermore, it has been demonstrated that the effects of the tensile fracture process zone cannot be omitted from the fracture mechanics analyses as far as structures of medium size are concerned.

Discoveries regarding the significant role which a tensile fracture process zone plays in controlling the structural behaviour of concrete have focused the fracture mechanics research on determination of various properties of the tensile fracture process zone and implementation of the properties in the analyses.

During the past decade applications of tensile-softening models have been extended to more complicated failure types such as shear failure of concrete structures; see also RILEM report 1989, which shows various examples of such applications. Successful applications of tensile-softening models to shear failure of concrete structures require well-grounded knowledge on softening processes of concrete when both normal and shear displacements occur in the fracture process zone. At the present time, such knowledge does not exist. This investigation, and the other investigations which are going on in other laboratories, are attempts to gain more knowledge on the softening process of concrete under the influence of combined normal and shear displacement.

1.2 Introduction of the present project

The investigation which is presented in this report deals with determination of some of the properties of the fracture process zone, which will successively be presented. This

investigation is based on the fracture mechanics model of Hillerborg, the "Fictitious Crack Model", which was developed during the seventies. The concepts and applications of the model have comprehensively been demonstrated in three theses presented by Modéer 1979, Petersson 1981 and Gustafsson 1985.

The major parts of the aforementioned theses deal with mode I applications of the Fictitious Crack Model to concrete. However, in the work of Modéer and Gustafsson some parts have been devoted to the shear strength analyses of reinforced concrete, which have further extended the applications of the model.

The comprehensive, theoretical work of Gustafsson clearly demonstrates the size-dependent shear performance of longitudinally reinforced concrete beams. Gustafsson concludes that the size-dependent shear performance of the reinforced concrete beams studied can be attributed to displacement localization due to the softening behaviour of concrete. As far as comparison with respect to the relative influence of the beam depth on shear strength is concerned, applications of the Fictitious Crack Model showed good agreement with the experimental results of some other investigators. However, as far as comparison of the absolute values of shear strength are concerned, the results of Gustafsson underestimate the shear strength. Gustafsson has discussed the causes of the underestimation. One of the possible causes, which also concerns the present investigation, was that in the material model of Gustafsson the influence of the shear on the fracture process zone after its formation was neglected. It is not known to what extent the described approximation of the fracture process zone affected the results reported by Gustafsson. However, after successful applications of the Fictitious Crack Model to concrete in general, and based on the theoretical results of Gustafsson, Hillerborg and Gustafsson outlined the present project which the author has carried out since 1986.

In the project description it is stated that more accurate applications of the Fictitious Crack Model to the shear fracture of concrete structures demand better knowledge about the behaviour of the fracture process zone under the influence of both normal and shear displacement. The following examples further elucidate the aim of the investigation.

Fig. 1.1 illustrates two cases of crack propagation. Figs. 1.1a and 1.1b illustrate the first case, i.e. straight-linear crack propagation, while Figs. 1.1c and 1.1d illustrate the second case, i.e. curve-linear crack propagation. According to the Fictitious Crack Model, in both cases and at any load level, a fracture process zone is initiated perpendicular to the first principal tensile stress, and the crack trajectory follows the direction which is perpendicular to the first principal stress direction at the instant when the fracture process zone is initiated. However, the difference between the two cases is that, in the first case, the directions of the principal stresses are constant during the crack propagation, whereas in the second case the directions are changed during the crack propagation. According to the Fictitious Crack Model, shear displacement and shear stresses do not occur inside the fracture process zone,

unless the direction of the first principal tensile stress is changed during the crack propagation. Consequently, in the first case there will be no shear stresses or shear displacements inside the fracture process zone whereas in the second case shear stresses and shear displacements will occur inside the fracture process zone. From the modelling point of view the major difference between the two cases is that in the first case the behaviour of the fracture process zone can be described by means of a single normal stress - normal displacement relationship, while in the second case the behaviour of the fracture process zone is described by means of stress - displacement relations, where both normal and shear stresses are simultaneously influenced by normal and shear displacements.

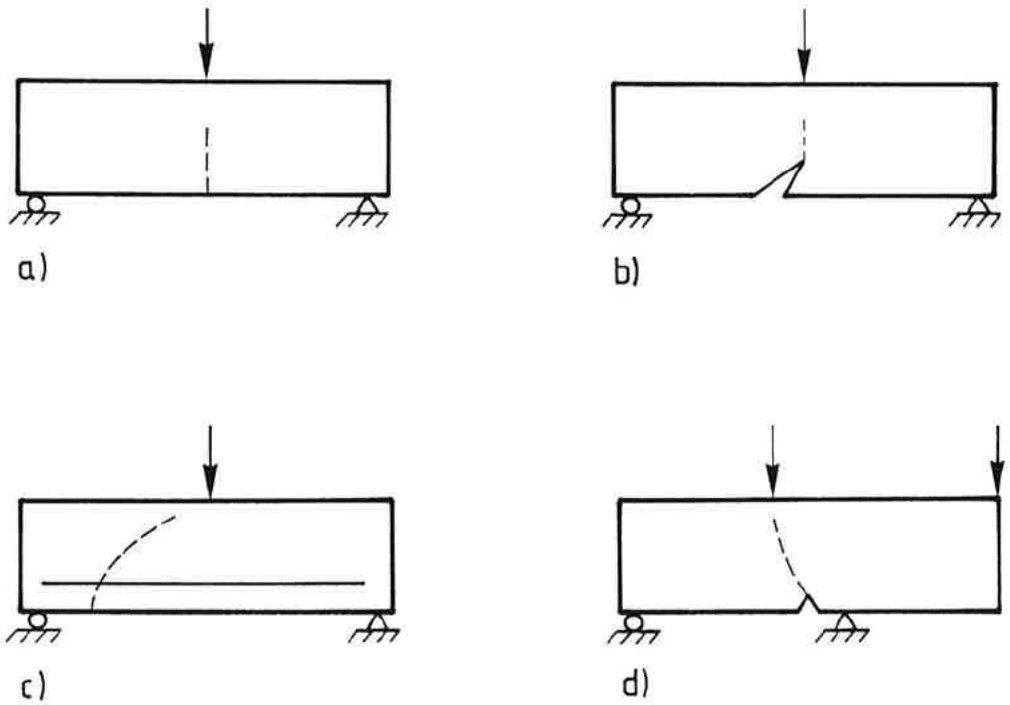

Fig. 1.1. Different cases of crack propagation.

The intention of this investigation is to develop a test method to determine the stress - displacement relations for fracture process zones which are initiated by tensile stresses and later on become influenced by simultaneous normal and shear displacements.

1.3 General limitations

This investigation deals with determination of material properties intended to be used by the Fictitious Crack Model in the cases of curve-linear crack propagation. Thus concepts of the

model have defined the intention of the investigation.

No considerations have been taken of other failure types. In this investigation, it is assumed that development of a real crack is preceded by formation of a fracture process zone, which in turn is initiated under pure tensile conditions. Furthermore, it has been assumed that in the case of varying first principal tensile stress direction, shear displacement and shear stress occur inside the fracture process zone.

Since this investigation is an experimental study, no emphasis has been placed on theories of fracture mechanics, nor has any consideration been taken of other fracture mechanics models. Nevertheless, some models are briefly described in order to clarify the author's position.

It has not been my intention to come up with a universal formula which describes the behaviour of fracture process zones under the influence of simultaneous normal and shear displacements.

The investigation concerns only the macroscopical properties of concrete and assumes concrete to be a homogenous material at the same structural level. However, a micro-mechanical model has been utilized in order to explain some of the phenomena observed in the tests.

In this investigation concrete is considered to be a non-yielding material which fails due to micro-cracking. Furthermore, in this investigation no distinction is made between plane strain and plane stress states.

All tests are performed in a displacement-controlled and monotonic manner.

2 Introduction to fracture mechanics

2.1 Introduction

Crack propagation in concrete structures is preceded by formation of a thin but extended fracture process zone, also called fracture zone and damage zone. Material inside the fracture process zone softens and acquires properties which differ from the remaining parts of the structure. Applications of models which take into account the effects of the fracture process zone have demonstrated the very important role which softening of concrete plays in governing the failure process of concrete structures of medium size. It is now widely agreed that an appropriate fracture mechanics model should take into account the effects of the softening behaviour of concrete.

A fracture process zone is modelled according to the two different major approaches, namely discrete crack approach and smeared crack approach. Both approaches are based on the same macroscopic behaviour and utilize the same basic material properties, but they differ in finite element implementation of the observed behaviour. However, since the Fictitious Crack Model is the basic model of this investigation, it is appropriate to present the theoretical framework of this report through the concepts of the discrete crack approach. Nevertheless, concepts of either of the approaches can be used in order to define the physical basis of the strain-softening models.

Since this report deals with fracture properties of concrete, the material concrete will be presented followed by brief discussion with regard to the basic factors which have greater impacts on the strength of the concrete.

Despite the limited range of this report, it has been found appropriate to give a brief introduction to the Linear Elastic Fracture Mechanics, in order to elucidate some of the fracture mechanics terminologies and the differences between the Fictitious Crack Model and Linear Elastic Fracture Mechanics Models.

A section is dedicated to the Fictitious Crack Model. The section presents the physical basis of the model and defines the material properties which are necessary for the applications of the Fictitious Crack Model.

In the last section the plausible mechanisms of the fracture are discussed.

2.2 Concrete

Concrete is made of ordinary portland cement or other hydraulic cement, aggregates and water. When cement reacts chemically with water it hardens and binds the aggregate particles together. Besides the above mentioned constituents, some other components and admixtures are also incorporated in order to control properties of both fresh and hardened concrete.

Conventional normal weight and normal strength concrete, standard concrete, has been manufactured with ordinary portland cement and natural or crushed stone and sand as aggregates. Classification of concrete by strength is done by means of its characteristic compressive strength, which in most standards varies between 12 and 80 MPa. The mean strengths of the standard concretes vary between 20 and 88 MPa, see for instance CEB-FIP Model Code. The water-cement ratios of the standard concretes vary between 1.1 and 0.4. In the literature, standard concrete is sometimes divided into three groups where concretes with compressive strengths 20 to 40, 40 to 60 and 60 to 70 are denoted low, medium and high strength concretes. These intervals are approximative and may vary widely in the literature. In the following parts of the report the term concrete alone denotes normal-weight normal-strength concrete, i.e. standard concrete. Furthermore, the term high strength concrete should not be confused with the other type of high strength concrete which has compressive strength higher than 90 MPa. These concrete qualities are denoted here as high-performance concrete.

Strength of concrete is basically governed by strength of the cement paste, which in turn is controlled by porosity of cement paste, i.e. it is controlled by water-cement ratio and air-entrainment. Water-cement ratios higher than 0.6, corresponding to compressive strengths lower than 40 MPa, result normally in a weak cement paste with poor bond properties which is not able to mobilize the strength of the aggregates. Consequently, strength of low-strength concrete is determined by strength of the cement paste, see Alexanderson (1982). Decreased water-cement ratio strengthens cement paste and the bond between cement paste and the aggregates, which leads to improved mobilization of the aggregate strength. Consequently, decreased water cement ratio increases influence of the aggregates on the strength of the concrete.

Beside the water-cement ratio, there are several other factors which have more or less influence on the strength of concrete. To discuss all these factors is out of the range of this report. However, there is another important factor, namely size of aggregate which also influences the bond between cement paste and aggregates. It has been demonstrated that for a given concrete quality the bond between fine aggregates and cement paste is normally stronger than the bond between coarse aggregates and cement paste. The reasons for this are stress concentrations, existing cracks caused by drying and chemical shrinkages and differences in thermal expansion of the cement paste and aggregates. Furthermore,

insufficient compaction may cause air bubbles to be locked up under coarse aggregates, and too long compaction in combination with high water-cement ratio may cause water separation under coarse aggregates. These effects increase the porosity of the interface region between coarse aggregates and cement paste, which leads to decreased bond strength. The above mentioned effects gradually lose their influence as water-cement ratio decreases. For instance in high performance concrete the strength of the cement paste and the interface region is such that they are able to mobilize total strength of the coarse aggregates. A detailed discussion of the microstructure of the interface region is given by Fagerlund (1982), to which the reader is referred.

From the fracture mechanics point of view, it is important to determine whether crack propagation avoids aggregates or not. It is difficult to point out the aggregate fractions which will be crossed by the crack. However, it can be said that, in low quality normal concrete, the coarse aggregates are avoided by the cracks while in the high performance concrete the cracks run through the coarse aggregates as well. In the intermediate range the amount of broken coarse aggregates increases with increased strength, which leads to more brittle structural behaviour of concrete. The measure of brittleness is described in section 2.5. Since the bond strength is influenced by many factors, it is not easy to determine the size which may cause aggregate fracture. However, evaluation of the amount of the fractured aggregates when the test is completed is a valuable instrument in order to explain phenomena observed in a test series.

2.3 Assumed structural levels

In macro-level, for instance structural level where the strength analyses are applied, hardened concrete is considered as a homogeneous material. This is due to the fact that the size of biggest inclusions of concrete usually are several times smaller than the size of the structure being studied. This assumption is also employed when fracture mechanics applications to concrete and determination of fracture parameters are involved. Due to stability requirements the direct tensile test specimens are usually small. However, insofar as they satisfy requirements of the continuum mechanics, the material which they are made of can be considered homogeneous. According to continuum mechanics, a material is considered homogeneous when the smallest section of the structure, made of the same material, is at least three times greater than the biggest inclusion inside the material.

Since macroscopic behaviour of concrete is governed by the properties of its components, it is essential that the composite structure of concrete also be examined in order to better understand the observed macroscopic phenomenon. The composite structure of concrete is very complex and can be subdivided into many phases. In order to achieve simplicity it is

beneficial to subdivide the structure of concrete into a few phases which, in turn, can also be regarded as composites. However, for the purposes of this report it is sufficient to consider concrete as a two-phase composite, where coarse aggregates are embedded in a homogeneous matrix of mortar. This model is sufficient in the sense that it distinguishes the events which control crack-line path, which in turn influences the macroscopic mechanical parameters.

In the following sections when determination of fracture mechanics parameters are concerned, concrete is considered as a homogenous material. Furthermore, when mechanisms of cracking are concerned, concrete is considered as a two phase composite as described above.

2.4 Linear Elastic Fracture Mechanics (LEFM)

2.4.1 Modes of fracture

In fracture mechanics three basic modes of failure are distinguished, namely mode I, often denoted as opening or tensile mode, mode II, also denoted as sliding or shear mode, and mode III or tearing mode. The basic modes are defined with respect to the geometrical separation of a body in two pieces, and are demonstrated in Fig. 2.1, see Hellan (1984).

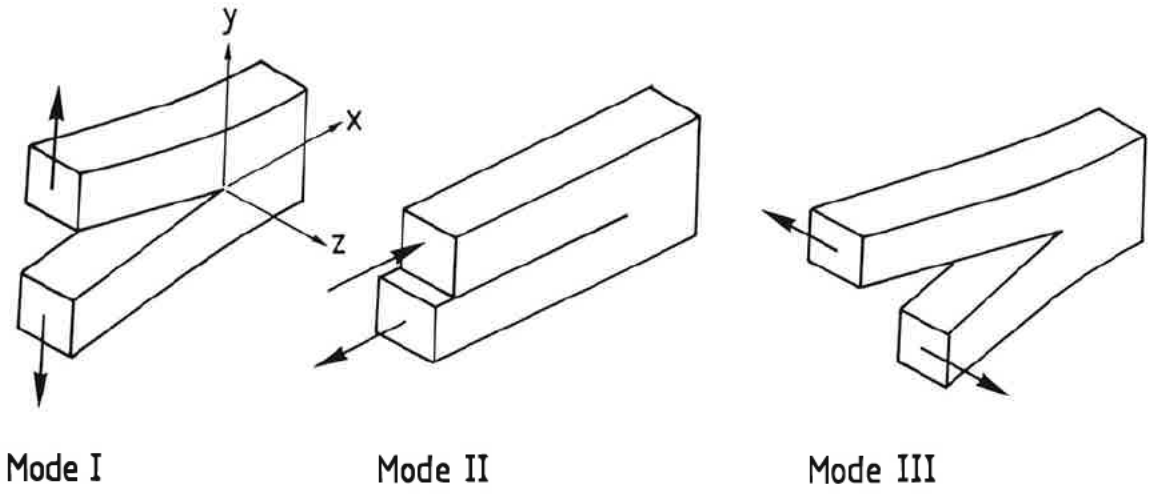

Fig. 2.1. Basic modes of fracture, Hellan (1984).

As far as fractures of homogeneous and isotropic materials are concerned, it is in practice difficult, if not impossible, to develop pure mode II or mode III. Therefore, besides pure mode I, modes of failure are often a combination of the basic modes which are called mixed

mode. A special case of mixed mode fracture, which will be described here, is mixed mode I and II, i.e. a combination of tensile and shear mode. Since among the mixed mode cases only mixed mode I and II will be discussed in this report, in the following sections the term mixed mode refers to mixed mode I and II.

2.4.2 Linear elastic crack propagation

In a linear elastic and isotropic material, the in plane stress state close to the crack tip in polar coordinates can be expressed by means of equation 2.1, see Carlsson (1976).

$$\begin{bmatrix} \sigma_{rr} \\ \sigma_{\theta\theta} \\ \tau_{r\theta} \end{bmatrix} = \frac{K_I}{\sqrt{2\pi r}} \begin{bmatrix} +\frac{5}{4}\cos\frac{\theta}{2} - \frac{1}{4}\cos\frac{3\theta}{2} \\ +\frac{3}{4}\cos\frac{\theta}{2} + \frac{1}{4}\cos\frac{3\theta}{2} \\ +\frac{1}{4}\sin\frac{\theta}{2} + \frac{1}{4}\sin\frac{3\theta}{2} \end{bmatrix} + \frac{K_{II}}{\sqrt{2\pi r}} \begin{bmatrix} -\frac{5}{4}\sin\frac{\theta}{2} + \frac{3}{4}\sin\frac{3\theta}{2} \\ -\frac{3}{4}\sin\frac{\theta}{2} - \frac{3}{4}\sin\frac{3\theta}{2} \\ +\frac{1}{4}\cos\frac{\theta}{2} + \frac{3}{4}\cos\frac{3\theta}{2} \end{bmatrix} + \ldots \qquad 2.1$$

In the equation, K is the stress intensity factor ($N/m^{3/2}$) and the indices denote the mode of the stress state. The other terms are described in Fig. 2.2.

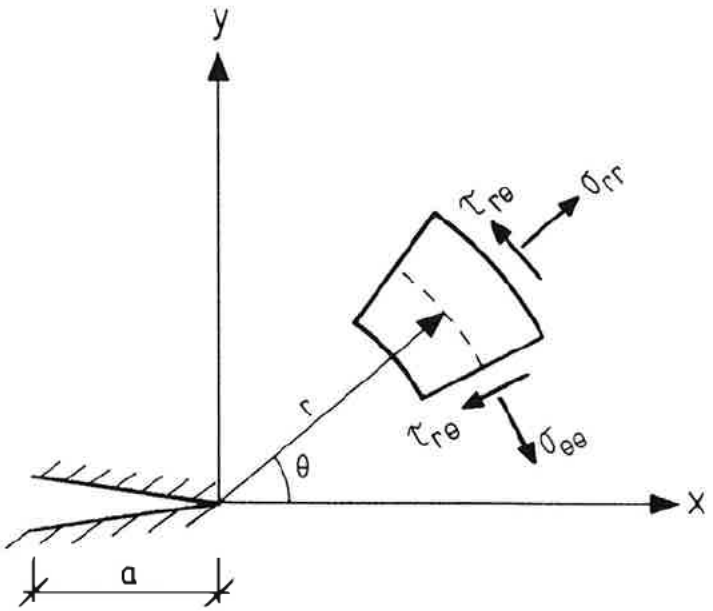

Fig. 2.2. Stress state close to the crack tip.

As can be observed, since stresses approach infinity with decreasing distance (r) to the crack tip, the strength criterion cannot be utilized in order to define conditions for crack propagation. Instead, in LEFM a stress intensity criterion is utilized.

In pure mode I, $K_{II}=0$, and pure mode II, $K_I=0$, the condition for crack propagation is fulfilled when the stress intensity factor assumes a critical value, which is denoted K_{Ic} in mode I and K_{IIc} in mode II.

For a structure (specimen) with given geometry and loading condition, the relation between remote stress and stress intensity factor is given by the following equation.

$$\sigma_\infty = \frac{K}{\sqrt{\pi a} f} \qquad 2.2$$

where σ_∞ is either remote tensile stress or remote shear stress, calculated according to the linear elastic theory for the case of a non-cracked body, K is either mode I or mode II stress intensity factor, a is crack length and f is a factor which is a function of the loading condition and the geometry of the body. Expressions for f, for simple loading conditions and geometries, can be derived analytically, whereas other methods should be utilized for complicated cases, see for instance Bäcklund (1982).

Besides the stress intensity criterion, the energy release rate is also utilized. When the energy release rate criterion is utilized, the condition for crack propagation is fulfilled when the energy release rate (G) assumes a critical value denoted as G_c. The relation between energy release rate and stress intensity factor for pure mode I and pure mode II in plane stress conditions is given by the following equation.

$$G = \frac{K^2}{E} \qquad 2.3$$

In mixed mode I and II, i.e. cases where none of the stress intensity factors are zero, two cases are distinguished, namely the case when the crack is self-similar, i.e. when the direction of the crack propagation is constant, and the case when crack kinking occurs.

In the first case, an effective stress intensity factor (K_e) is utilized which is a function of both mode I and mode II stress intensity factors, see equation 2.4. In practice, K_e is normally equated to the K_{Ic} in order to define conditions for self-similar mixed mode crack propagation.

$$K_e^2 = EG = K_I^2 + K_{II}^2 \qquad 2.4$$

In the second case it is also possible to derive an effective stress intensity factor. However, in this case, the effective stress intensity factor ($K_{e\theta}$) is not only a function of K_I and K_{II} but also a function of the crack kink angle (θ_0).

Several different theories, see for instance Ingraffea and Saouma (1985), have been proposed in order to determine the effective stress intensity factor and the crack branching angle. Since as far as this report is concerned it would be to no purpose to describe all the theories, only one will be mentioned, in order to demonstrate the basics of the linear elastic mixed mode crack propagation. The theory which will be described here is called "the Maximum Tangential Stress Theory" formulated by Erdogan and Sih in 1963. According to this theory cracks propagate in the direction along which $\sigma_{\theta\theta}$ is maximum and $\sigma_{r\theta}$ is zero. Furthermore, crack propagation is initiated when $K_{e\theta}=(2\pi r)^{1/2}\sigma_{\theta\theta}$ assumes a critical value, which is equated to K_{Ic}. With regard to the noted conditions and equation 2.1, the following equations are obtained.

$$K_I\left(\frac{1}{4}\sin\frac{\theta}{2}+\frac{1}{4}\sin\frac{3\theta}{2}\right)+K_{II}\left(\frac{1}{4}\cos\frac{\theta}{2}+\frac{3}{4}\cos\frac{3\theta}{2}\right)=0 \qquad 2.5$$

$$K_{e\theta}=\sqrt{2\pi r}\,\sigma_{\theta\theta}=K_I\left(\frac{3}{4}\cos\frac{\theta}{2}+\frac{1}{4}\cos\frac{3\theta}{2}\right)-K_{II}\left(\frac{3}{4}\sin\frac{\theta}{2}+\frac{3}{4}\sin\frac{3\theta}{2}\right)=K_{Ic} \qquad 2.6$$

Equations 2.5 and 2.6 are the governing equations in the maximum tangential stress theory. The first equation gives the crack kink angle (θ_0) for a given crack tip location and loading conditions, whereas the second one defines the criteria for the initiation of crack propagation. The crack will propagate, if the calculated parameters satisfy equation 2.6, see Ingraffea et.al. (1985) and Hellan (1984).

The maximum tangential stress theory is reduced to the pure mode I case if the kink angle is equated to zero, because K_{II} should be zero in order to satisfy equation 2.5. Therefore, according to this theory, self-similar crack propagation is not a mixed mode crack propagation which contradicts the assumptions of equation 2.4.

This describes briefly the modes of fracture and criteria for crack propagation. Nevertheless, the reader is referred to references which are given in the text for detailed descriptions of Linear Elastic Fracture Mechanics.

2.5 Fictitious Crack Model (FCM)

2.5.1 Physical basis - pure tensile crack propagation

The Fictitious Crack Model is a discrete crack model based on the tensile softening of cementitious materials. The physical basis of FCM is most simply described by the results of a stable displacement-controlled tension test conducted on a concrete bar, under ideal conditions. Test setup is illustrated in Fig. 2.3a. Two segments (A and B) are demarcated on the bar where two identical displacement transducers are attached. On the assumptions that the bar possesses the same properties everywhere, that the displacement is evenly distributed and that final separation of the bar will occur inside the segment A, the result of the complete test will be as shown in Fig. 2.3b, where curve A displays results for segment A and curve B displays results for segment B.

Test results show that the segments behave in the same manner in the pre-peak region while they behave differently in the post-peak region. Besides the differences between curves A and B, each curve is composed of several regions which display differing material behaviour, which will be discussed in section 2.6. The reason for the differing behaviour of the segments is that at peak a fracture process zone (damage zone) is formed inside segment A, where the additional displacement takes place, while the other sections of the bar, which are not damaged, experience unloading, i.e. decreased displacement. Decrease of displacement is caused by reduction of stress due to softening of the material inside the fracture process zone. The characteristic of the fracture process zone is that it has a small extension in the direction of the stress while it involves entire breadths of the bar in the direction perpendicular to the stress direction, see Fig. 2.3c.

In the following parts, Fig. 2.3b is used in order to introduce the material properties which are utilized by FCM. The fracture process zone is modeled by means of a stress-displacement curve which can be derived by subtracting the descending branch of curve B from curve A, Fig. 2.3d. The other parts of the structure (undamaged sections) are modeled by means of a stress-strain curve which can be derived from curve B.

The area beneath the stress-displacement curve is the fracture energy denoted G_F (N/m). Another important parameter which can be derived from the test results is the characteristic length denoted l_{ch} (m), see equation 2.7.

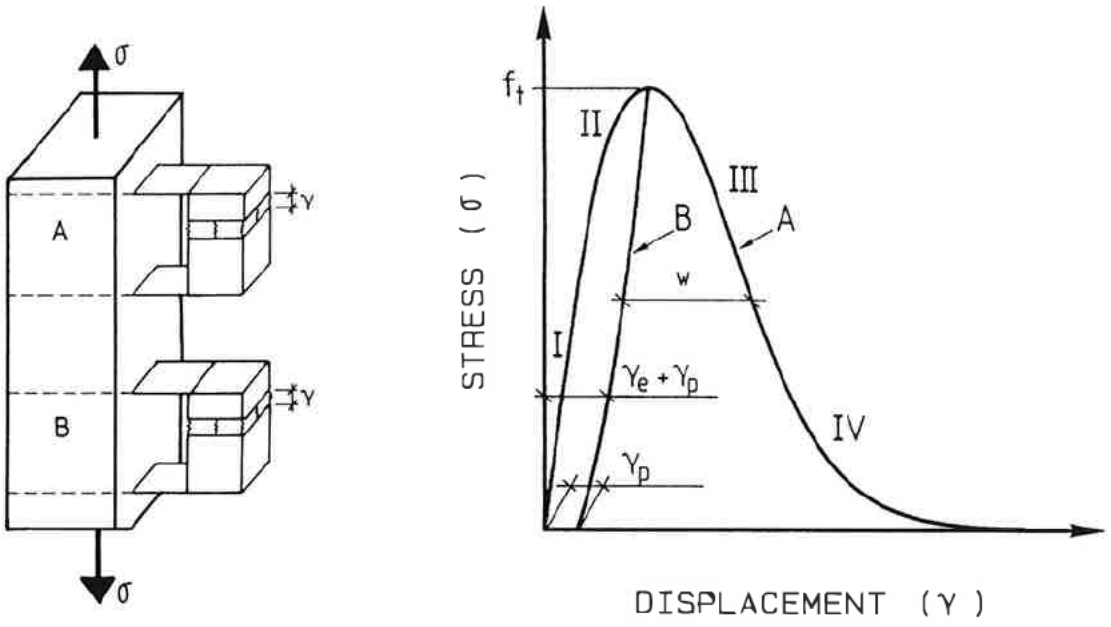

a) Test setup

b) Test results

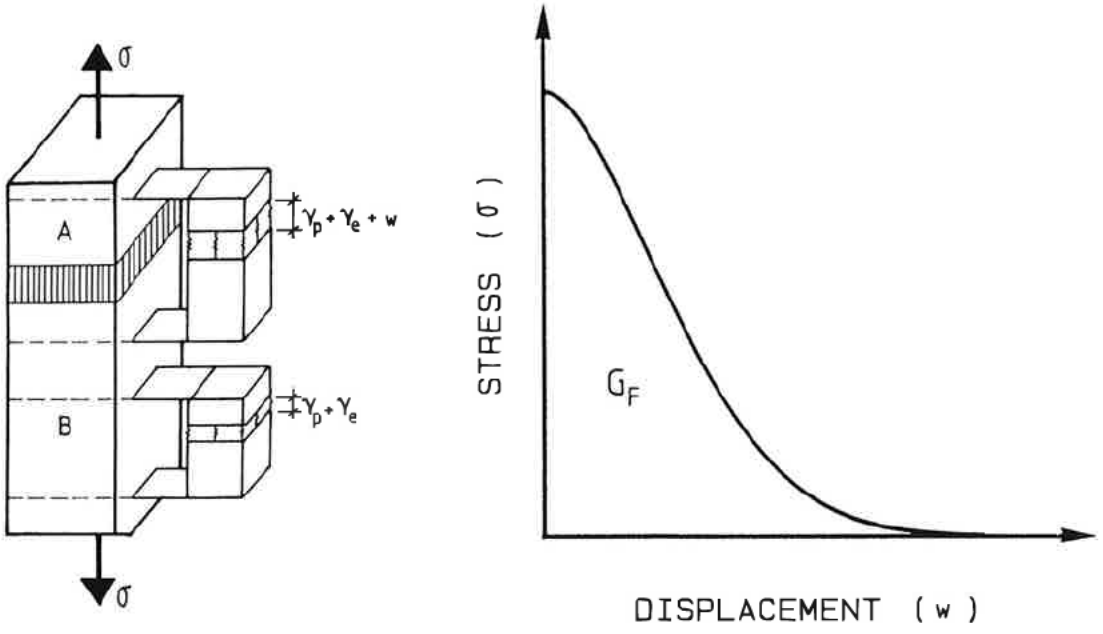

c) Additional displacement due to the formation of the fracture zone.

d) Stress - displacement curve of the fracture zone.

Fig. 2.3. Physical basis of the Fictitious Crack Model.

$$l_{ch} = \frac{EG_F}{f_t^2} \qquad 2.7$$

E is modulus of elasticity and f_t is tensile strength. According to the FCM, l_{ch} is a material parameter which controls the extension of the fracture process zone. On the assumption of linear elastic bulk behaviour, equation 2.7 can be rewritten in the following ways:

$$l_{ch} = \frac{1}{2}\frac{2E}{f_t f_t} G_F = \frac{1}{2}\frac{2}{\epsilon_o f_t} G_F = \frac{1}{2}\frac{G_F}{\eta_o} \qquad 2.8$$

$$l_{ch} = \frac{E}{f_t}\frac{G_F}{f_t} = \frac{\overline{w}}{\epsilon_o} \qquad 2.9$$

where ϵ_0 (m/m) is strain at maximum tensile stress, and η_0 (Nm/m^3) is strain energy density at maximum tensile stress, i.e. elastic energy per unit volume. Thus, l_{ch} is proportional to the ratio between the fracture energy and the maximum elastic energy which can be stored per unit volume of the material. $\overline{w}$ is average displacement in the fracture process zone. Thus, l_{ch} is the ratio between average displacement inside the fracture process zone and the maximum strain of the material, see also Chapter 7 in RILEM-report (1989).

FCM defines a brittleness number d/l_{ch}, where d is the characteristic size of the structure. Since l_{ch} controls size of the fracture process zone, the ratio d/l_{ch} is indirectly a comparison between the size of the structure, for instance depth of a beam, and the extension of the fracture process zone. It has been demonstrated that when the brittleness number approaches infinity, i.e. a small fracture process zone compared to the size of the structure, the structural behaviour becomes linear elastic, and when the number approaches zero, the structural behaviour becomes elastic-plastic, see Petersson (1981) and Gustafsson (1985). Furthermore, since the brittleness number indirectly relates the displacement and the stored elastic energy of the bulk to the displacement and fracture energy of the fracture process zone, the brittleness number is a measure of brittleness of the structure. A low brittleness number means extended fracture process zone and ductile fracture behaviour.

In the Fictitious Crack Model, tensile crack growth, straight-linear crack growth, is described in the following manner. When the first principal tensile stress reaches the tensile strength of the material, a fracture process zone starts to develop perpendicular to the direction of the first principal tensile stress. The stress state inside the fracture zone is pure tensile and it is

maintained as long as the direction of the first principal stress remains constant. The incremental relationship between the tensile stress and the displacement is as follows:

$$d\sigma = C(w) \cdot dw \qquad 2.10$$

σ is the stress and w is the displacement inside the fracture process zone. C is the slope of the curve in Fig. 2.3d. C is negative, which indicates that the tensile stress decreases when displacement increases.

Finite element implementation of FCM and algorithms for simulations of crack propagation under mode I conditions have been comprehensively discussed by Petersson (1981), and Gustafsson (1985). Nevertheless, some of the assumptions are reviewed below. The assumptions are as follows.

The discrete crack approach is utilized, viz width of the fracture process zone is equated to the additional displacements within the fracture process zone. Consequently, the fracture process zone has zero extension at the instant of the formation. Furthermore, it has the extension w_c, critical crack opening displacement, at the instant of complete separation.

Material located inside the fracture process zone is modelled by means of a stress-displacement curve which is normally simplified by means of linear segments.

Material located outside the fracture process zone is as a rule modelled by means of a linear stress-strain curve.

The described assumptions are visualized in Fig. 2.4.

2.5.2 Curve-linear crack propagation

In the previous section the physical basis of the Fictitious Crack Model was described. In this section, development and growth of the fracture process zone during curve-linear crack propagation will be presented.

Since concrete is considered as a homogeneous and isotropic material with a tensile strength much lower than its compressive strength, it is assumed that a fracture process zone will be formed in the same way as in the pure tensile case. This in spite of the prevailing stress state which normally is not considered as a pure tensile stress state. The statement is visualized in Fig. 2.5.

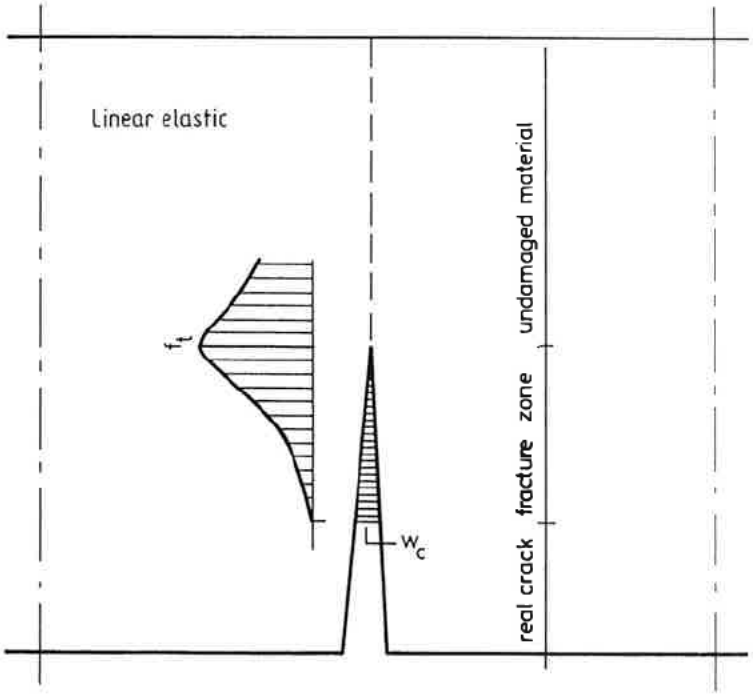

a) Crack propagation.

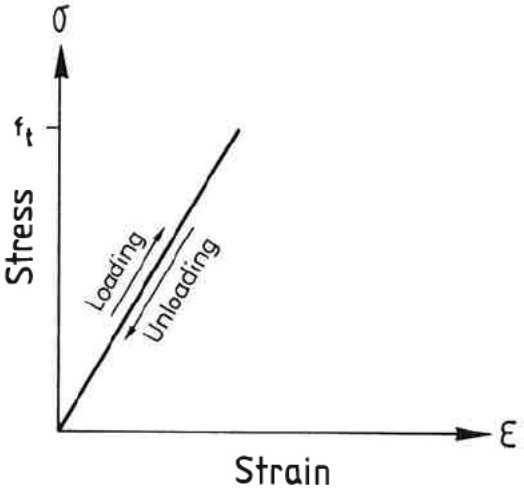

b) Properties of the linear elastic section.

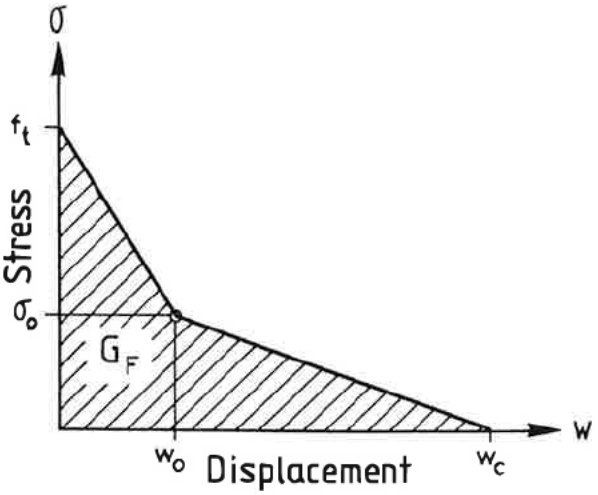

c) Properties of the fracture process zone.

Fig. 2.4. Visualization of the assumed material behaviour according to the Fictitious Crack Model.

Consider an infinitesimal two dimensional section of the loaded body with the stresses acting on it and assume that the prevailing stress state causes first and second principal stresses σ_1 and σ_2 with the direction indicated in Fig. 2.5b. According to FCM, a fracture process zone, on the plane of the second principal stress, will be initiated when the first principal tensile stress approaches the tensile strength of the material. Neglecting the influence of the second principal stress, this case is identical with the tensile loading of the concrete bar described in the previous section. On the assumption of the unchanged principal stress direction, the further development of the fracture process zone continues in the same way as described previously. In this case, normal stress (σ) and normal displacement (w) are the only occurring stress and displacement inside the fracture process zone. However, if during the subsequent stages the direction of the first principal stress varies, shear stress (τ) and shear displacement (δ) will also occur inside the fracture process zone, see Fig. 2.5c.

The curve-linear crack propagation cases which are illustrated in Fig. 1.1 are often referred to as mixed-mode crack propagation. In this report it is preferred not to use this term in combination with the FCM-description of the curve-linear crack propagation in order to avoid misunderstanding, especially with the description given by LEFM. However, for a short period assume that the term mixed-mode is also utilized by FCM; the following few paragraphs will elucidate the differences between FCM-description and LEFM-description of mixed-mode crack propagation.

LEFM equations have been derived on the assumption of existing sharp cracks. Therefore, applications of the LEFM are limited to cases with preexisting cracks or notches, while existence of cracks and notches is not necessary for the applications of FCM. Since LEFM application requires preexisting cracks and notches, the differences between the models are discussed for the cases with preexisting cracks and notches.

Fig. 2.6 illustrates two different cases of crack propagation initiated from sharp notches. Assume that the crack trajectories are perpendicular to the first principal stresses and σ_1^i and σ_2^i are principal stresses during the crack propagation, which have constant direction in case (a) and varying direction in case (b).

In case (a), since directions of the principal stresses are constant, no shear stresses (shear displacements) will occur inside the fracture process zone. Therefore, this case despite the kink (θ_0) is considered as mode I crack propagation by FCM. In case (b), on the contrary, shear stresses, shear displacements, will occur inside the fracture process zone because, in this case, the directions of the principal stresses are not constant during crack propagation. Therefore, this case is considered as mixed mode crack propagation. However, in contrast with FCM, both cases are considered as mixed mode crack propagation by LEFM. It should be noted that in case (a) when the crack growth is well started, the condition will be changed to mode I crack propagation, because the crack growth will be self-similar, see section 2.4.

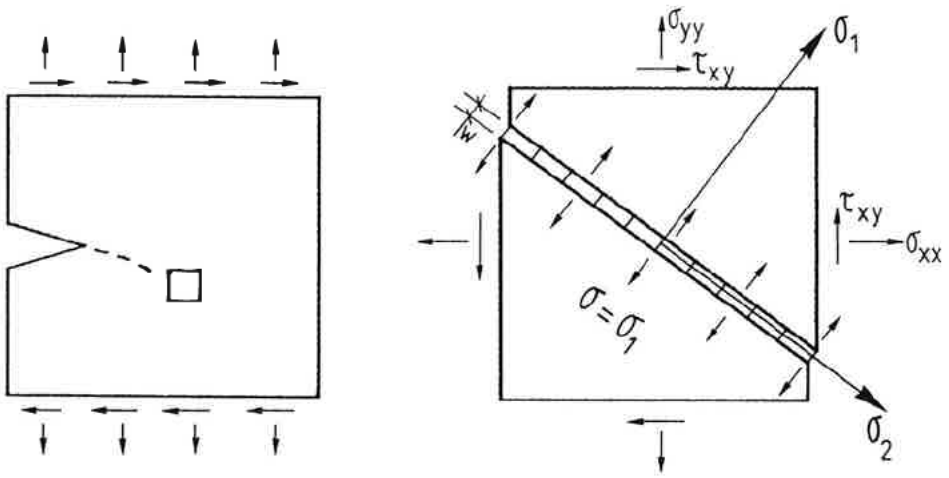

a) Loaded body. *b) Formation of the fracture zone.*

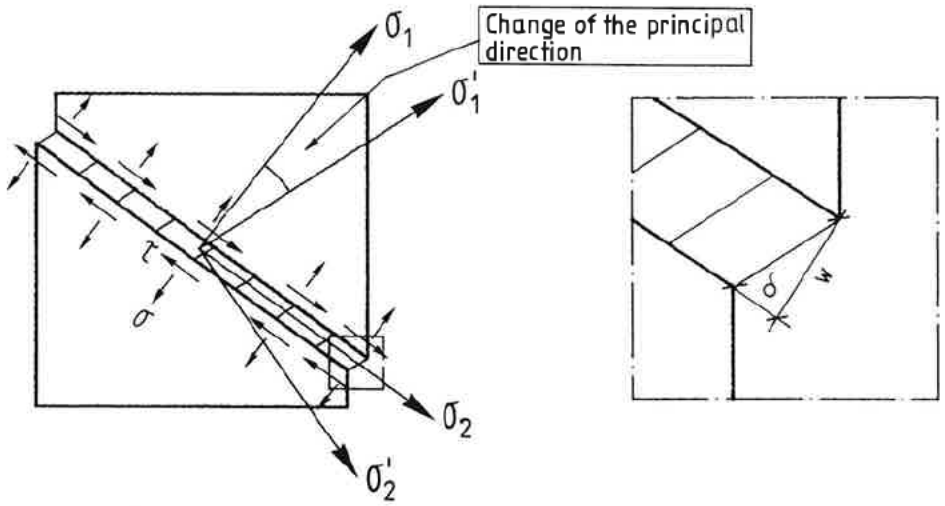

c) Occurrence of the shear stress and shear displacement inside the fracture zone.

Fig. 2.5. Visualization of the stress state within the fracture zone due to the curve-linear crack propagation, according to FCM.

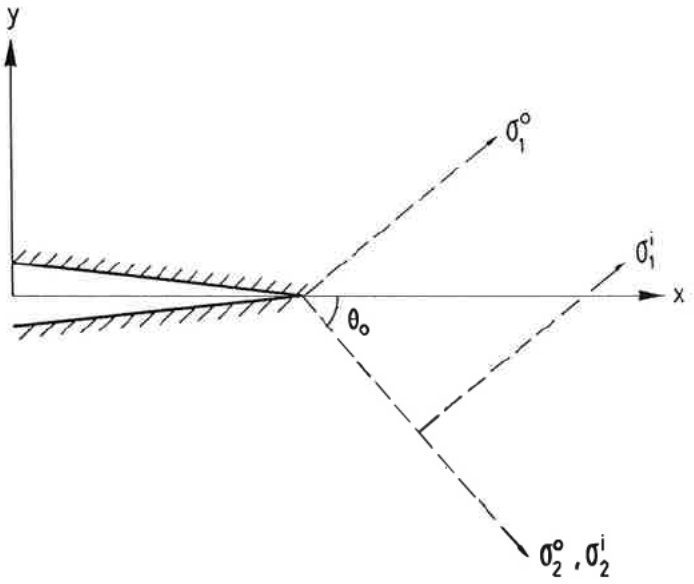

a) Propagation of a crack with constant direction.

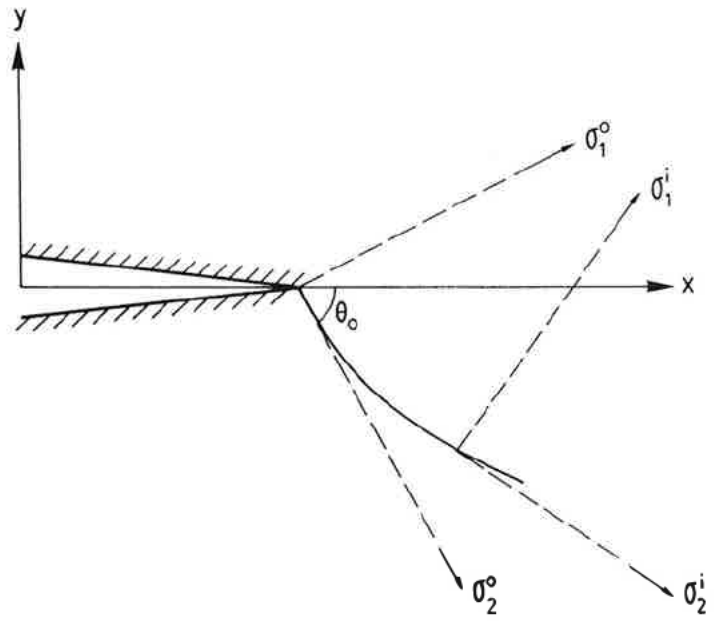

b) Propagation of a crack with varying direction.

Fig. 2.6. Two cases of crack propagation.

Linear elastic analyses show that the stress approaches infinity when the distance to the sharp cracks approaches zero. Consequently, since FCM assumes finite stresses anywhere inside a loaded body and as a rule linear elastic bulk behaviour, a fracture process zone will be initiated as soon as the load starts to increase. The structural response is linear in the beginning and differs gradually from linearity due to further widening and extension of the fracture process zone, which lead to continuous variation of the stress field inside the body, especially close to the notch tip prior to the peak load. Fig. 2.7a shows schematically a load - displacement response of a notched body which can be calculated by means of the Fictitious Crack Model. The figure also illustrates feasible stress fields close to the notch tip at two different load levels for both cases described in Fig. 2.6. Analysis by means of LEFM , for instance equations 2.5 and 2.6, may give a result similar to the curve illustrated in Fig. 2.7b. As is demonstrated, behaviour of the structure is linear up to the maximum load level. At this load level a real crack starts to propagate which gradually increases the compliance of the structure. In contrast with the FCM, the stress field inside the body is constant prior to the initiation of the crack propagation.

As can be seen, the stress fields predicted by the models may differ completely from each other, which may have great influence on the calculation of the crack trajectory as the crack propagates.

The above-mentioned description indicates that FCM does not make any distinctions between mode I and mixed mode conditions where initiation of the fracture process zone (localization of the displacements) is concerned. Furthermore, mixed mode conditions appear locally, inside the fracture process zone, and do not concern the undamaged part of the structure. In the LEFM, the term mixed mode is utilized in cases when both K_I and K_{II} are non-zero or in cases when the direction of the developing real crack deviates from the direction of the pre-existing crack or notch. Utilizing this definition, crack propagation in Figs. 1.1b, c and d becomes mixed mode crack propagation, whereas according to FCM, only the cases in Figs. 1.1c and d are mixed-mode crack propagation.

In Fig. 2.5c an infinitesimal part of a fracture process zone is illustrated. In the figure, stresses acting on the crack are indicated, where σ is normal stress and τ is shear stress. w and δ denote the normal- and shear-displacements of the fracture process zone. It should be noted that the fracture process zone is illustrated as a discrete fictitious crack, i.e. the width of the fracture zone has been equated to the crack opening displacement. Modelling of the fracture process zone under such conditions requires knowledge about the relation between the stresses and the displacements. The incremental relationship between stresses and displacement is given by equation 2.11.

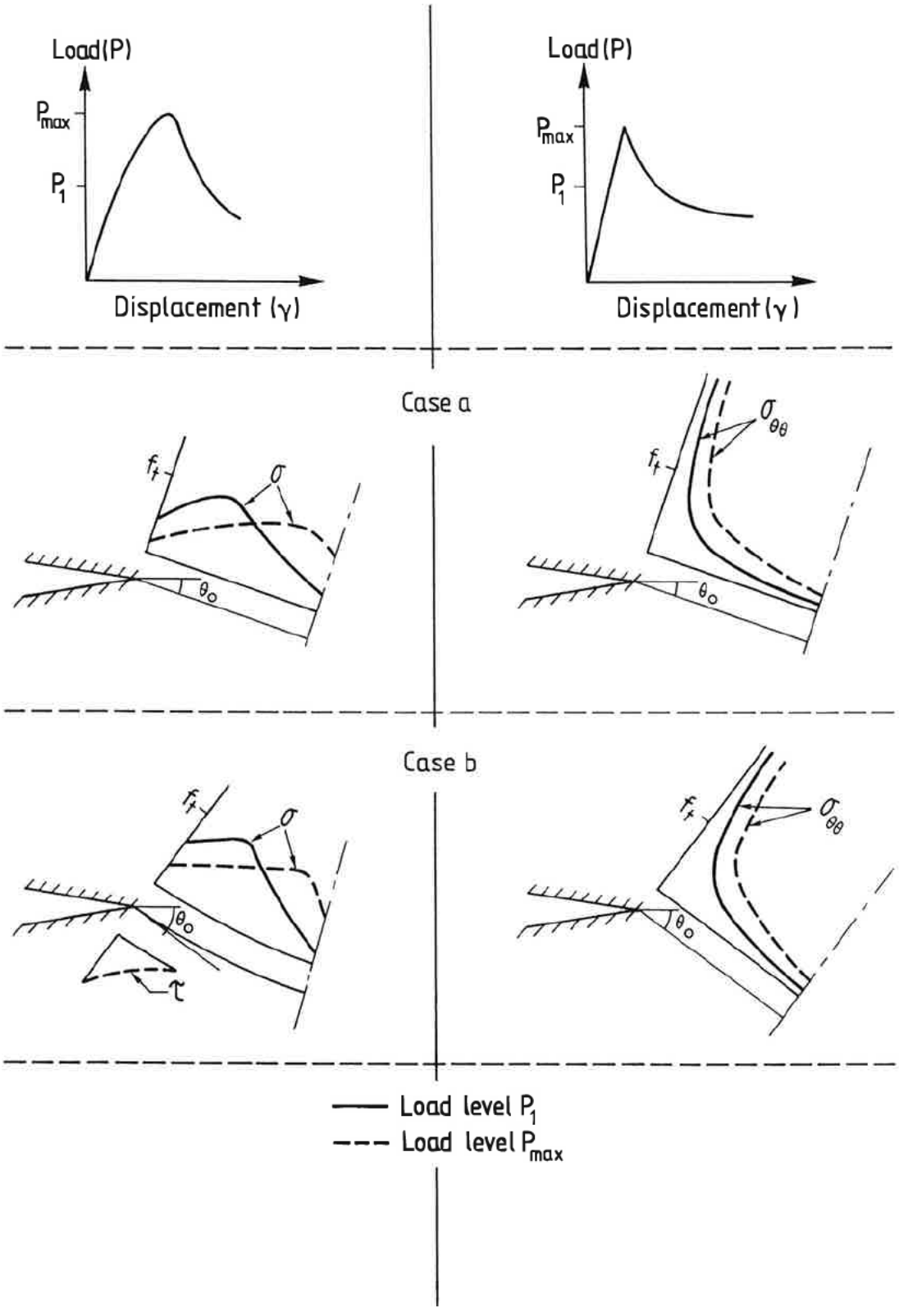

Fig. 2.7a. Feasible stress fields along the crack path, according to FCM.

Fig. 2.7b. Feasible stress fields in the direction of kink, according to LEFM.

$$\begin{bmatrix} d\sigma \\ d\tau \end{bmatrix} = \begin{bmatrix} C_{11} & C_{12} \\ C_{21} & C_{22} \end{bmatrix} \begin{bmatrix} dw \\ d\delta \end{bmatrix} \qquad 2.11$$

in which the square matrix is the crack stiffness matrix and C_{11}, ..., C_{22} are crack stiffness coefficients which depend on normal- and shear-displacements. Furthermore they depend on the history of the displacement, i.e. the displacement path on the plane of the normal- and shear-displacement. There is experimental evidence, see for instance Walraven (1980), which shows that the crack stiffness matrix is not symmetric, $C_{12} \neq C_{21}$.

Similar relationships can be formulated for the smeared crack models by smearing out the crack displacement over a certain length.

To date, there is no adequate knowledge about the stiffness coefficients described in equation 2.11. In spite of this, several applications have been reported where the constitutive relation of the fracture process zone has been approximated. Below, some of the approximations are reviewed.

The stiffness matrix is reduced to a pure tensile stiffness matrix if all terms except the normal crack-stiffness (C_{11}) are equated to zero. In this case no shear transfer occurs across the fracture zone, i.e. the behaviour of the fracture process zone is modeled by a stress-displacement curve as in the ordinary FCM. This consideration, but with some modifications, has been utilized by Gustafsson (1985) in the shear strength analyses of longitudinally reinforced concrete beams. In the material model of Gustafsson the shear inside the fracture process zone is neglected. However, since in the finite element applications Gustafsson prescribed the crack path, he modified the stress - displacement curve (σw-curve) for those cases where the prescribed crack path did not coincide with the actual crack path. The same material model has also been utilized by Rots (1988) in discrete crack analyses of the Crack-Line-Wedge-Loaded Double-Cantilever-Beam and Single Notched Shear Beam. In these analyses the cracks were modelled as a tensile fracture zone.
In the discrete model of Ingraffea and Saouma (1985), the off diagonal term (C_{12}) in the crack stiffness matrix is equated to zero, while the normal crack stiffness (C_{11}) is equated to the crack stiffness as in the pure tensile case. Hence, in this model the normal stress is a function of solely normal displacement (w). In this model, shear within the fracture process zone is modeled by means of a relationship developed by Fenwick and Paulay, see Chapter 3. In that relationship the shear stress is a non-linear function of normal displacement (w) and a linear function of shear displacement (δ), viz $C_{21} \neq 0$ and $C_{22} \neq 0$.

In the smeared crack applications the off diagonal stiffness coefficients are normally equated to zero, while the shear crack stiffness is modelled by a decreasing shear modulus which is

obtained by multiplying the elastic shear modulus with a factor between 0 and 1, usually referred as shear retention factor. Shear retention factors which are used in practice are either constants or a function of the normal strain. In Hordijk et.al. (1989) some expressions for shear retention factor are given.

The drawback of the two latter approximations is that the effect of the shear displacement on the normal stress is neglected. If the concepts of curve-linear crack propagation which previously were defined are correct, the stress condition in the fracture process zone is predominately pure tensile at the instant of formation of the zone. In the following stages when both normal- and shear- displacements continuously increase, the tensile normal stress decreases, and in some cases may even become compressive. It is important to recognize what happens to the normal crack coefficients (C_{11} and C_{12}) during the transition from the tensile stress state to the compressive stress state. To date, there are no constitutive crack models which describe the normal stress transfer across the fracture process zone as a continuous function of both normal and shear displacements simultaneously. The existing constitutive crack models consider the existing normal stress conditions as a pure tensile stress condition which is not affected by shear displacements. Nevertheless models based on the aggregate interlock relate the normal stress to the shear displacement as well. However, in these models the normal stress is assumed to be compressive stress affected by the shear displacement. These models neglect the tensile history of the fracture process zone and consider the fracture process zone as a rough crack, which does not fit the definition of a fictitious crack, see also Chapter 3.

Finally, it is appropriate to describe the primary objectives of this investigation once again. The primary objectives of this investigation have been development of a test method and performance of tests in order to determine the crack stiffness coefficients which are defined in equation 2.11.

2.6 Mechanisms of fracture

The events associated with the process of tensile fracture of concrete have been intensively studied since the development of tensile-softening models and recognition of the decisive role of the fracture process zone. Extensive work has been carried out in order to identify the events and relate them to the sections on the tensile stress - displacement curve. In spite of the complex nature of concrete and experimental difficulties, valuable information about the microscopic tensile behaviour of concrete has been gained. By support of the results published during the last decade it is now possible to describe the microscopic tensile behaviour of concrete in an approximate manner, while a precise description requires further research. Below, a description of the microscopic tensile behaviour of concrete will be given which is

generally accepted.

It is wellknown that failure of concrete is caused by formation of micro-cracks which gradually increase in number and coalesce prior to the final separation of the concrete specimen into two pieces. It has been demonstrated that the micro-cracks start to develop at stress levels approximately 50-80 percent of the tensile strength, at locations where the material is weakened, normally at coarse aggregate-mortar interface, i.e. bond cracks.

At higher stress levels micro-cracks also occur in the mortar primarily as bridging cracks, i.e. combined cracks, connecting the bond cracks, and secondly as dispersed mortar cracks, Mindess 1983, Smadi and Slate 1989. At this stage, micro-cracks are distributed over a large volume of the body. After a certain strain, the process of micro cracking becomes localized within a fracture process zone, inside which additional development and coalescence of micro-cracks takes place. As a rule the strain at which the localization occurs is equated to the strain at peak stress, because this is the only well defined point on the stress-strain curve. After peak stress, material located inside the fracture process zone gradually softens, which in a displacement-controlled direct tensile test leads to unloading of the entire specimen.

As it is illustrated in Fig. 2.3d, the stress-displacement curve of the fracture process zone consists of two sections, where the first section is much steeper than the second section. The reason for this is given by Hordijk et.al. (1989), who explain that in the upper section growth and coalescence of micro-cracks are dominating events, whereas in the lower section the sliding friction between the crack surfaces and extraction of the aggregates from the mortar are the dominating events.

The described tensile fracture process is a general description of some events which occur during tensile fracture of concrete and does not discuss the influence of the concrete quality and properties of its components on the cracking process, which in turn has great influence on mechanical parameters. Mechanical properties of concrete such as tensile and compressive strength, modulus of elasticity, fracture energy and characteristic length, are determined by the mechanical properties of the cement paste, aggregates and the interaction between them. Tab. 2.1 demonstrates some examples of the mechanical properties of concrete with varying water-cement ratio and maximum aggregate size. The first part of the table shows the influence of the water-cement ratio on the mechanical properties of the normal concrete, Petersson (1981). The second part of the table shows the influence of the aggregate size on the mechanical properties, Wolinski et.al. (1988). The third part of the table shows the mechanical properties of high performance concrete with silica-fume admixture. It should be noted that the mechanical properties of concrete are not unambiguously determined by the mentioned parameters, viz water-cement-ratio and aggregate size, but there are several other parameters which may have great influence on the mechanical properties of concrete.

w/c	d_{max} mm	f_c MPa	f_t MPa	E GPa	G_F N/m	l_{ch} mm	References
0.3	12	86	4.5	48	113	283	
0.4	12	74	4.3	44	117	300	Petersson
0.5	12	54	3.8	42	103	300	
0.7	12	30	2.4	36	80	508	
0.5	2	42	2.3	33	76	469	
0.5	4	47	2.4	33	85	489	
0.5	8	47	2.8	32	108	437	Wolinski
0.5	16	52	2.9	34	109	435	
0.5	32	48	2.9	33	112	437	
-	16	122	5.2	43	137	224	Remmel
0.3	8	114	6.0	51	98	138	Hassanzadeh

Tab. 2.1. Mechanical properties of concrete with varying water-cement ratio and maximum aggregate size.

Data on the mechanical properties of aggregates are scarce. However, Tab. 2.2 demonstrates the mechanical properties of some rock types. The table has been complied by means of the data reported by Ouchterlony (1981). It should be noted that in the table, G_F has been equated to $(K_{Ic})^2/E$. The properties of the rocks demonstrated in the table vary over a wide range, both within individual groups of rocks and between the groups. Therefore, it is difficult to point out typical mechanical properties for aggregates. However, in order to simplify the discussions the rocks have been divided into two groups. The first group includes granite, basalt and quartzite which are denoted here as normal aggregates. The second group includes sandstone and limestone which are denoted here as weak aggregates. The mean value of the mechanical properties of each group is calculated and shown in the table. The mean values are regarded in this report as typical mechanical properties for normal aggregates and weak aggregates respectively.

Data on the mechanical properties of the cement paste are also scarce. The author has not been able to find any complete data on the above-mentioned properties, for cement pastes with varying water-cement ratio. However, in the end of the Tab. 2.2 mechanical properties of one quality cement paste are given.

Tab. 2.1 shows that the strength and the modulus of elasticity of the concrete increase with decreasing water-cement ratio. The reason is that cement paste and its bond to aggregates becomes stronger and stiffer as water-cement ratio decreases, which leads to more efficient utilization of the strength and stiffness of the aggregates.

The material data in Tabs. 2.1 and 2.2 demonstrate that the average fracture energy and characteristic length of normal concrete is much higher than its components. The following description may explain some of the differences. Fig. 2.8 shows crack propagation in a normal concrete. In the figure the path of the arising real crack and the crack path for the case of homogeneous material are indicated. As is shown in the figure, considerable micro-cracking and bridging cracks may take place outside the propagating real crack, which leads to increased energy dissipation and increased deformability of the fracture process zone. Furthermore, the deviation of the crack path from its intended trajectory leads to increased energy dissipation caused by extraction of the aggregates and increased total fracture surface.

Tab. 2.1 shows that fracture energy of normal strength concrete increases with decreased water-cement ratio. Since the fracture energy of aggregates is relatively low, reduction of the fracture energy is theoretically expected for concrete with very low water-cement ratio, i.e. theoretically much lower fracture energy is expected for high performance concrete compared to normal concrete. As is demonstrated in Tab. 2.1, fracture energy of high performance concrete has almost the same magnitude as fracture energy of normal concrete. Since fracture properties of cement paste and its bond to the aggregates are not known, it is difficult to explain the observed behaviour. However, in spite of stiff and strong cement paste and bond between cement paste and aggregates, micro-cracking and bridging of the cracks may take place.

Tab. 2.1 shows that characteristic length of concrete decreases with decreasing water-cement ratio, i.e. increased strength leads to more brittle behaviour in spite of increased fracture energy.

Besides water-cement ratio there are several other factors which have great influence on the mechanical properties of concrete. It is beyond the scope of this report to discuss all the influencing factors. The data reported by Wolinsky are presented in order to demonstrate the differences between mortar (maximum aggregate size smaller than 4 mm) and concrete (maximum aggregate size greater than 4 mm). According to Wolinsky concrete is slightly stronger than mortar, and the fracture energy of concrete is greater than that of mortar. Furthermore, there is no difference in brittleness between the materials.

Another important issue is the behaviour of the fracture process zone and micro-cracking when it is subjected to combined normal and shear displacements. This issue will be discussed in Chapter 4.

Material	f_t MPa	E GPa	G_F N/m	l_{ch} mm
Chelmsford granite	7	45	7	6
Fichtelgebrige granite	22	41	62	5
Westerly granite	14	63	114	37
Dresser basalt	22	86	50	8
Sioux quartzite	9	70	89	77
Normal aggregate	15	61	64	27
Arizona sandstone	6	8	273	61
Boise sandstone	2	5	87	109
Colorado sandstone	8	33	192	99
Milsap sandstone	3	10	227	252
Ruhr sandstone	21	36	54	4
Austin limestone	2	11	15	41
Carthage limestone	5	32	77	99
Indiana limestone	4	19	84	100
Leuders limestone	4	19	38	45
Weak aggregate	6	19	116	90
Cement paste, w/c = 0.35	4	7	20	10

Tab. 2.2. Mechanical properties of rock and cement paste.

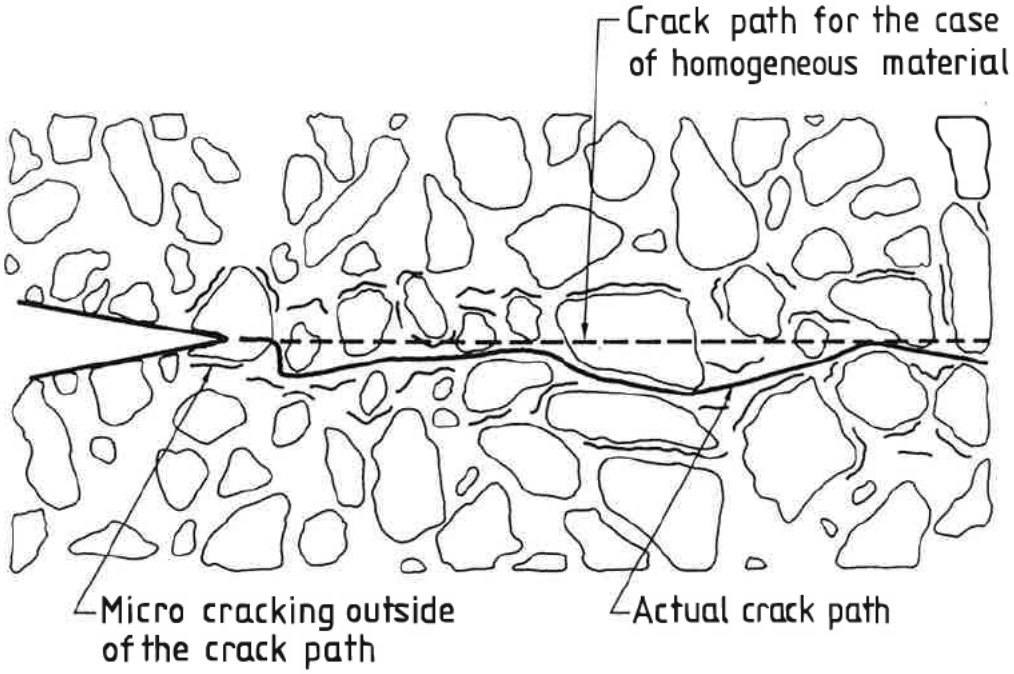

Fig. 2.8. Schematic description of crack propagation in concrete.

3 Determination of the fracture mechanics parameters

3.1 Introduction

In the previous chapter, the physical basis of FCM and the material properties required by the model were described. In this chapter the methods by which the properties are determined will be presented.

3.2 Determination of tensile properties

3.2.1 Introduction

The usual applications of FCM to pure tensile crack propagation require material properties such as modulus of elasticity, tensile strength and the stress - displacement relationship of the fracture process zone. In the next section some considerations regarding determination of the tensile strength and the stress - displacement relationships by means of direct tensile tests on notched concrete prisms will be discussed, while no attention will be paid to the determination of the modulus of elasticity. Furthermore, no attention will be paid to the alternative methods for determination of the tensile strength of concrete. However, for more information the reader is referred to Modéer (1979), Petersson (1981) and Gustafsson (1985).

3.2.2 Direct tensile test on notched concrete prisms

Tensile strength and stress - displacement relationships of the fracture process zone can be determined by means of displacement-controlled, direct tension tests on notched concrete prisms. Fig. 3.1 displays schematically a test setup and the result of such a test. The specimen is glued in between two attachments which in turn are connected to the testing machine. The springs and spirals in the figure, with the translational stiffness S_{nm} (N/m) and the rotational stiffness S_{rm} (N/m), characterize the properties of the testing arrangement outside the specimens, which may have great influence on the test results. These will be discussed later in section 3.2.4.

Displacement (γ) is the mean value of two gauges placed on either side of the specimen. In practice, several types of gauges are utilized, for instance clip gauges, transducers, strain gauges and LVDT (linear variable differential transformers). In this investigation only clip gauges have been used. Therefore in the following, the term "gauge" refers to clip gauge, and by displacement is meant the displacement measured by the clip gauges placed inside the

notches. In the absence of the unloading branch (see curve B in Fig. 2.3b) it is normally assumed that unloading of the material outside of the fracture process zone takes place along a straight line as is indicated in Fig. 3.1b. The line has the same slope as the initial slope of the stress - displacement curve (σ-γ curve). The stress - displacement curve of the fracture process zone (σ-w curve) is obtained by subtracting the unloading line from the stress - displacement curve (σ-γ curve) of the specimen.

3.2.3 Stability requirements of the tensile tests

In direct tensile tests, two types of instabilities are distinguished. The first type of instability occurs when the release of the stored elastic energy in the specimen and the testing arrangements is greater than the energy which can be consumed by the specimen. In a symmetric tensile test setup, for instance the setup in Fig. 3.1, with a conventional testing machine without any feedback and fast regulating system, the criterion for stability is formulated as below, see Hillerborg (1984) and (1989):

$$S_{ntot} = \frac{1}{2\left(\frac{1}{S_{nm}} + \frac{1}{S_{ns}}\right)} > A_0\left(-\frac{d\sigma}{dw}\right), \qquad S_{ns} = \frac{2EA}{h} \tag{3.1}$$

S_{nm} (N/m) is translational stiffness of the devices outside the specimen and S_{ns} (N/m) is translational stiffness of the specimen, with regard to the symmetry of the test setup. $d\sigma/dw$ (N/m^3) is the slope of the stress - displacement curve of the fracture process zone, i.e. the slope of the σ-w curve; A_0 (m^2) is the fracture surface, A (m^2) is the area of the section outside the fracture zone and h (m) is the length of the specimen between the supports. However, this kind of instability has been overcome by the development of modern closed-loop testing machines which possess quick feedback and regulating systems.

The second type of instability occurs when two parts of the specimen, on both sides of the fracture process zone, rotate with respect to each other, i.e. rotational instability. Rotation of the parts of the specimen causes uneven displacement distribution along the fracture zone, which has been observed experimentally by Hordijk et.al. (1987), van Mier and Nooru-Mohamed (1988), Raiss et.al. (1990) and van Mier (1991). Occurrence of the rotational instability has, in some cases, considerable impact on the results of tensile tests, which has theoretically been treated by Hassanzadeh et.al. (1987), Hillerborg (1989a) and Zhou (1988). Below, some parts of their work are reviewed.

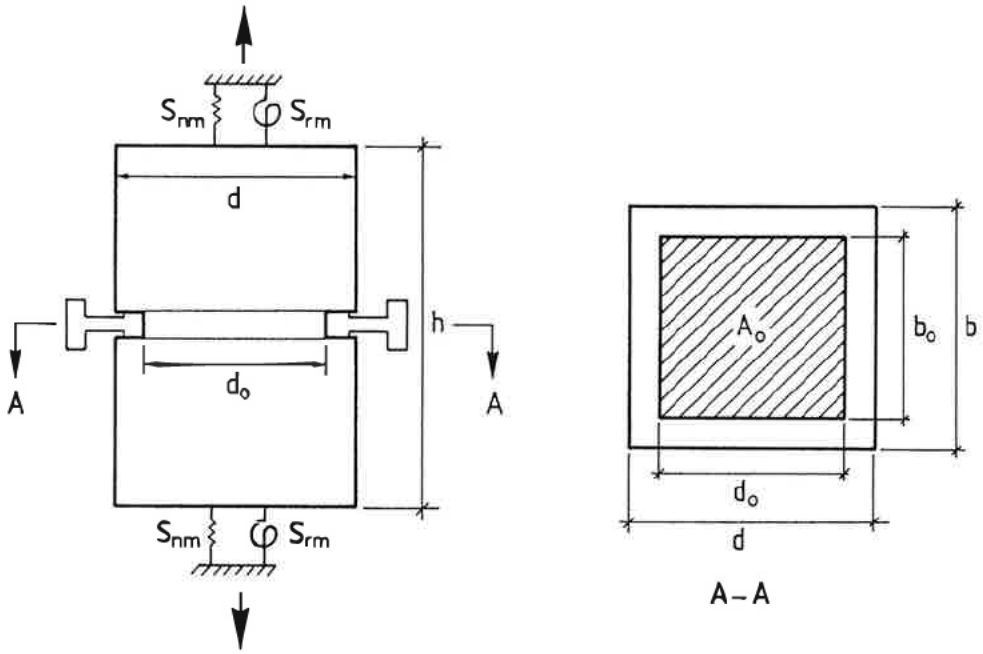

a) Test setup and specimen cross-section.

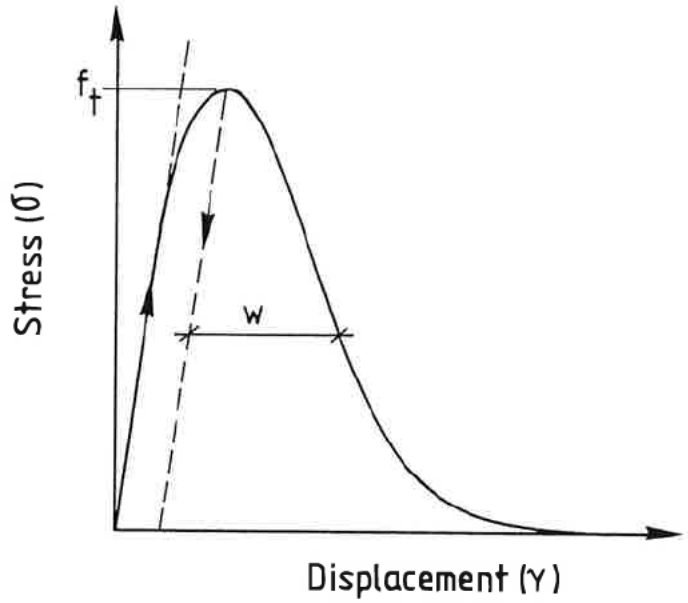

b) Test result.

Fig. 3.1. Schematic description of a tensile test setup and result.

The reason for occurrence of the rotational instability has been discussed by Hillerborg (1989a). According to Hillerborg, the rotational instability in a tension test is the same phenomenon as the buckling of a column in compression, but with the difference that in the first case the stress is tensile and the stiffness of the body is negative, while in the second case the stress is compressive and the stiffness of the body is positive. Furthermore, according to Hillerborg, instability may occur even though the load is perfectly centric. Based on the assumptions of symmetrical test arrangement, see Fig. 3.1, linearly distributed normal displacements along the fracture zone and small difference between highest and lowest displacements inside the fracture process zone, Hillerborg has derived the following rotational stability criterion:

$$S_{rtot} = \frac{1}{2\left(\frac{1}{S_{rm}} + \frac{1}{S_{rs}}\right)} > I_0\left(-\frac{d\sigma}{dw}\right), \qquad S_{rs} = \frac{2EI}{h} \tag{3.2}$$

S_{rm} (Nm/rad) is rotational stiffness of the test arrangement outside the specimen, S_{rs} (Nm/rad) is the rotational stiffness of the specimen outside the fracture process zone, h (m) is length of the specimen between the supports, I_0 (m^4) and I (m^4) are moment of inertia of the specimen inside and outside of the fracture zone.

According to equation 3.2, a stable tensile test requires sufficient total, rotational stiffness, S_{rtot}. If the stiffness is not sufficient, the parts of the specimen on either side of the fracture process zone will rotate with respect to each other. Hillerborg also calculated the impacts of the different S_{rtot} on the stress-displacement curves of the fracture process zone, for the perfectly centric loading condition. Hillerborg's calculations show that if the total stiffness is not sufficient, rotational instability occurs during the tensile tests, which in some cases is revealed by "bumps" on the stress - displacement curve (σ-γ curve), see Fig. 3.2. However, no exitance of bumps on the stress - displacement curves does not necessarily mean that the test is stable. According to the analyses the bump is most pronounced within a certain interval of S_{rtot} which is 0.05-0.4 times the value of $I_0(-d\sigma/dw)$ at $w=0$. According to the analyses the bump moves upward on the curve and the impact of the rotational instability on the curve diminishes by increased rotational stiffness. Furthermore, Hillerborg shows that the bump disappears in the case of zero rotational stiffness (free rotation) while the uneven displacement distribution within the fracture zone remains.

Hillerborg's analyses were based on the condition of perfect centric loading. However, in practice unintended eccentricity may occur due to imperfect attachment of the specimen, non-centric induction of the notches and uneven distribution of the material properties within the specimen. The existence of eccentricity increases the impact of the rotational instability on

the results of the tension tests. Zhou (1988) has, by means of the finite element method, calculated the impact of the eccentricity on the results of the tension tests. Fig. 3.3 shows results of the analyses and the test setup. The results show that the instability caused by eccentricity reduces the measured tensile strength and distorts the shape of the stress - displacement curve (σ-γ curve). Zhou has also analyzed the impacts of the rotational stiffness on the stress - displacement curve (σ-γ curve), with the same test setup as above. The results are displayed in Fig. 3.4, and demonstrate that the curves obtained in a tension test are smooth when the rotational stiffness is zero or sufficiently low. Furthermore, the results show that the bumps on the stress - displacement curve appear when the rotational stiffness increases and disappear again when the rotational stiffness has become sufficiently high. The results also demonstrate that the calculated stress - displacement curve approaches the true curve by increasing rotational stiffness, compare Figs. 3.3 and 3.4.

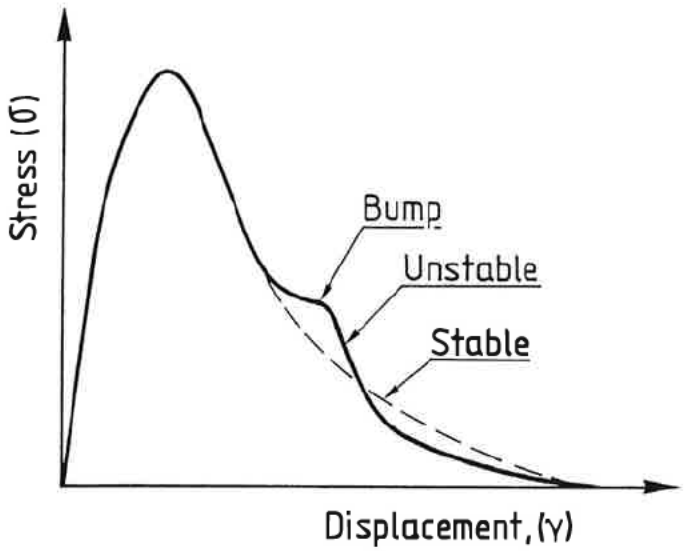

Fig. 3.2. Illustration of a bump.

The work of Hillerborg and Zhou clearly demonstrates that the rotational instability should be considered in determination of tensile properties of the fracture process zone. In this project, efforts have been made to develop a testing method which can prevent the rotational instability. The equipment will be presented in the next section.

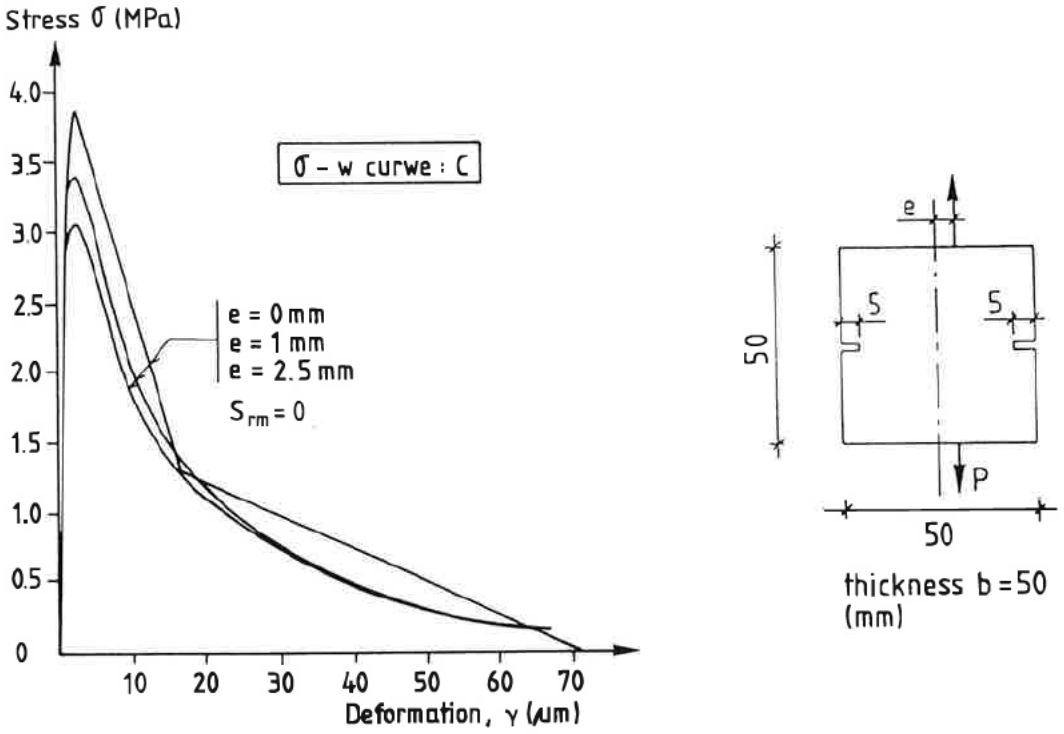

Fig. 3.3. Impact of eccentricity on the tensile stress - displacement curves, theoretical analyses by Zhou (1988).

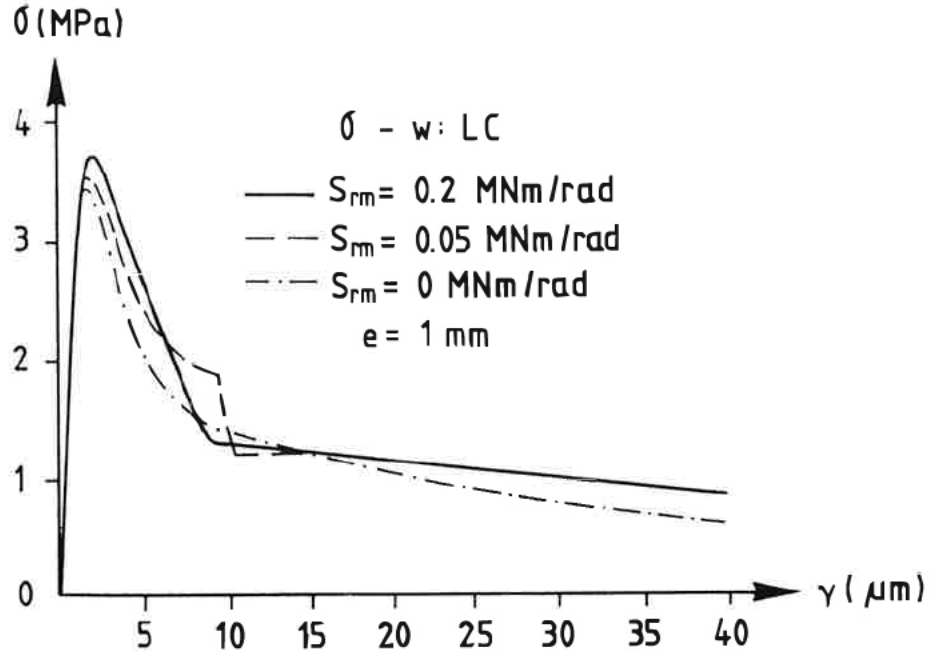

Fig. 3.4. Impact of rotational stiffness on the tensile stress - displacement curves, theoretical analyses by Zhou (1988).

3.2.4 Testing equipment for direct tension tests

At the start of this project, under the supervision of Hillerborg, the author became aware of the phenomenon of the rotational instability and was recommended to consider the solution which is sketched in Fig. 3.5. The equipment consists of two beams which are connected in their end points (points A and B) by a thin steel sheet. The equipment is connected by hinges to a servo-controlled closed-loop testing machine at points C and D. The specimen is glued to the steel plates connected to the beams. This equipment is also able to impose shear displacement into the specimen. Shear displacement is transferred from the supports E and F through the beams to the specimen. This option, together with the physical data on the equipment, is presented in section 3.3.3.

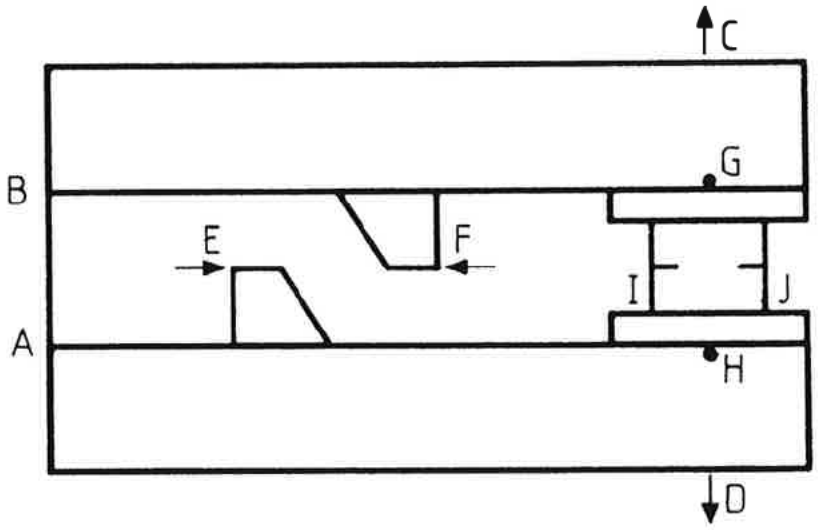

Fig. 3.5. Sketch of the test equipment developed in this project.

Tension tests are conducted in the usual manner, viz, the tests are performed in displacement controlled manner. Displacements are measured by means of a pair of clip gauges with the edges placed a few millimetre inside the notches. Since the system is statically determined and the steel sheet is relatively thin, the load transferred to the specimen is approximately equal to the load measured by the load-cell of the testing machine.

In the tension tests point D is pulled away from point C by the testing machine. Since the distance A-B is constant, the bending stiffness of the beams resists the rotation of the parts of the specimen which are located on either side of the fracture zone. Furthermore, in the plane perpendicular to the plane of the beams, the bending stiffness of the steel sheet resists the torsion of the end-points of the beams, which in turn resists the rotation of the parts of the specimen on either side of the fracture zone. However, since the distance A-B is constant whereas the distance G-H is not, unintended rotation will be imposed to the beams instead

of pure translation, which will cause uneven displacement distribution within the fracture zone. However, this can be reduced if the beams are sufficiently long.

During the construction of the equipment there were unfortunately no simple design formulas available to theoretically anticipate the performance of the equipment. Therefore, the design of the equipment is mostly based on surmises and compromises. However, the following facts were taken into consideration:

Since at that time the required stiffness of the beam could not be calculated, the stiffness of the beams was chosen as high as possible, but with the restrictions that the equipment should be light enough in order to be handled by one person, the beams should have standard profiles and it should be easy to montage various details on the beams.

Properties of the thin steel sheet should be such that, firstly it prevents the vertical relative movement and torsion of the end of the beams. Secondly, it permits rotation of the beams around their connection points to the testing machine without any considerable impact on the measured normal and shear loads. These two requirements are in conflict with each other. However, by means of simple static calculations, not given here, an optimum size for the steel sheet was calculated, which for the present configuration of the equipment and range of the tests does not introduce any significant errors.

Since the distance A-B is constant while the distance C-D is changed during the tests, the beams rotate around the connection points C and D, which gives rise to uneven displacement in the fracture zone. In order to decrease this effect, the beams should be as long as possible. However, increased length results in increased weight and decreased stiffness of the beams. Here also an optimum case should be calculated. By accepting a limited difference between the displacements on left and right sides of the fracture zone, and by means of calculations based on the rigid body motion an optimum beam length was calculated. Calculations which are not given here were carried out for both pure tension and combined tension and shear cases.

Later on, Hillerborg developed formulas by which the performance of the equipment could be examined theoretically. The formulas were based on the assumptions that a fracture process zone has extended over the whole specimen cross section, all cross sections remain plane, the material outside the fracture process zone is elastic and the load is applied with an unintended eccentricity which causes the instability. Derivation of the formulas is given in

Appendix A. The analysis of Hillerborg leads to the following formulas:

$$M_e\left(\frac{2}{hA_0\sigma}-\frac{1}{4S_{rs}}\right)=M_c\left(\frac{2}{hA_0\sigma}+\frac{1}{2I_0\dfrac{d\sigma}{dw}}+\frac{1}{4S_{rs}}\right)$$

$$M_e\left(\frac{1}{S_{rm}}+\frac{1}{2S_{rs}}\right)+M_c\left(\frac{1}{2I_0\dfrac{d\sigma}{dw}}+\frac{1}{2S_{rs}}\right)=\frac{eA_0\sigma}{S_{rm}}+\frac{1}{2L}\left(w+\frac{2A_0\sigma}{S_{rs}}\right) \qquad 3.3$$

$$\Delta w=\frac{12M_c}{b_0d_0^2}\frac{1}{\dfrac{d\sigma}{dw}}$$

M_e (Nm) is the moment acting upon the beam, M_c (Nm) the moment caused by uneven distribution along the fracture process zone, S_{rm} (Nm/rad) is in this case the rotational stiffness of the beams, S_{rs} (Nm/rad) is the rotational stiffness of the specimen. A_0, A, I_0 and $d\sigma/dw$ are described previously. Δw is the difference between displacements at right and left sides of the fracture process zone. The other notations are described in Figs. 3.1 and 3.6.

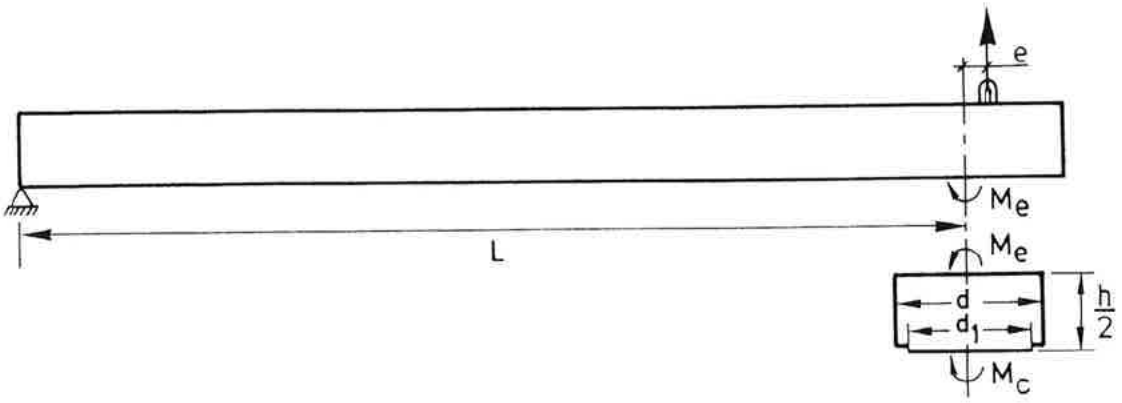

Fig. 3.6. Description of some of the notations used in equation 3.3.

The formulas can also be used for the case of torsional direction by assuming $L=\infty$. The stability criterion, equation 3.2, can be obtained from present formulas by equating the determinant of the equation system, composed of first and second formula, to zero and assuming that $hA_0\sigma$ is much lower than S_{rm} and S_{rs}.

It should be noted that the equipment is also used for combined normal and shear tests. In these tests eccentric imposed shear load and uneven distributed shear stresses on the fracture plane give rise to torsion of the specimen around its length axis. The torsion is counteracted

by the torsional stiffness of the specimen and rotational stiffness of the beams on the plane perpendicular to the plane which is shown in Fig. 3.5. In this investigation no attention has been paid to influences of torsion of the specimen on the test results.

Below, the results of analysis by means of the presented formula are described. The analysis is carried out for the specimen displayed in Fig. 3.9. The rotational and torsional stiffness of the beams are 0.87 MNm/rad and 0.12 MNm/rad respectively. However, in the torsional case the compliance of the steel sheet has also been taken into consideration, which leads to an equivalent torsional stiffness of 0.09 MNm/rad. The modulus of elasticity is assumed to be 30000 MN/m^2.

Fig. 3.7 shows the stress - displacement curve of the fracture process zone, viz σ-w curve. The numbers on the curve refer to the mean displacements at which the displacement and stress distribution along the fracture zone is calculated. The magnitude of the unintended eccentricity which may occur in practice is not known. However, with regard to the preparation and the attachment of the specimen, which will be described later, a few millimetre, of eccentricity is not inconceivable. Furthermore, the uneven distribution of the material property along the fracture process zone may also give rise to uneven displacement, which can be replaced by an equivalent unintended eccentricity. With regard to the mentioned facts, in this analysis the unintended eccentricity has been equated to 3 mm.

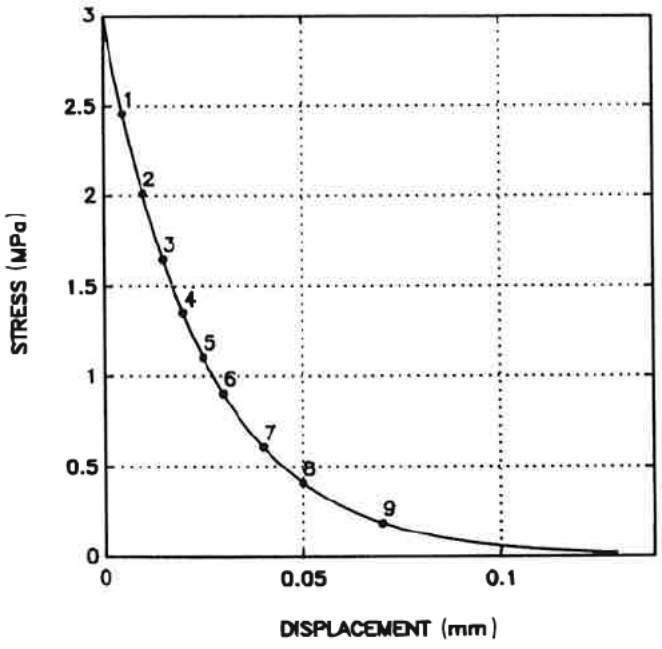

Fig 3.7. σ-w curve and mean displacements used for determination of the development of the stress and displacement along the fracture process zone.

Fig. 3.8a displays development of the displacements and stresses along the fracture process zone, in the plane of the beams. The numbers refer to the position on the mean stress - mean displacement curve. The dashed lines refer to the case of zero eccentricity. The results show that the stiffness of the beams is sufficient in this case. However, some errors are imposed due to successive inclination of the beams caused by increased distance between points G and H, but with acceptable magnitude. This conclusion has also been verified by means of finite element analysis, see Zhou (1988).

Fig. 3.8b displays development of the displacements and stresses along the fracture process zone, in the plane perpendicular to the plane of the beams. The results show that the torsional stiffness of the beams is not sufficient. The differences between displacements and stresses on either side of the fracture process zone are not acceptable.

Performance of the equipment is further tested through measurements of the displacements in different locations on the specimen. The displacements were measured by means of six clip gauges, see Fig. 3.9, where gauges 1 and 2 were coupled. Direction of the specimen is distinguished by means of line I-J, compare Figs. 3.5 and 3.9. The results are displayed in Figs. 3.10 and 3.11. In Fig. 3.10, displacement of curve number 1 is the mean value of the displacements recorded by gauges 1 and 2. The other numbers on the curves refer to the numbers of the clip gauges. Fig. 3.11a displays development of the displacements along the fracture process in the plane of the beams. In the figure the vertical axis represents the displacements and the horizontal transversal axis represents the dimensionless distance between the gauges. The solid lines represent the variation of the displacement along the line from gauge 3 on the left side of the figure to gauge 4 on the right side of the figure. The dashed lines represent the variation of the displacement along the line from gauge 5 to gauge 6. The dot on the vertical axis corresponds to the mean value of gauges 1 and 2. Fig. 3.11b displays development of the displacements along the fracture process zone in the plane perpendicular to the plane of the beams. The configuration of the figure is the same as for Fig. 3.11a but with the difference that the variation of the displacements is given in the perpendicular direction compared to the previous figure.

The results show that in the plane of the beams there are some differences between the recorded displacements in the beginning, compare curves 3 and 5 with 4 and 6 in Fig. 3.10 and the slope of the lines in Fig. 3.11a. The maximum difference between gauge-couples is approximately 0.007 mm at peak load, which decreases to 0.003 mm shortly after the peak load; note the distance between solid and dashed lines in Fig. 3.11b. Comparison between the mentioned differences reveals the fact that the higher difference at the peak load is due to the occurrence of the instability, which diminishes as the test proceeds. Furthermore, the comparison reveals the fact that the oblique translation of the beams with respect to each other introduces an error on the order of magnitude of 0.003 mm.

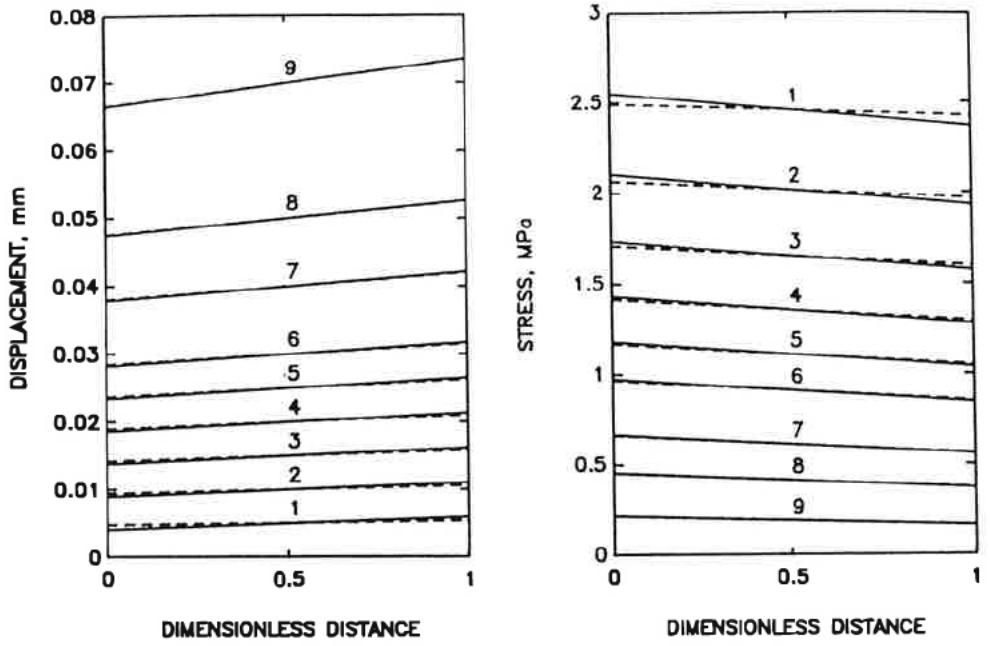

Fig. 3.8a. Development of the displacement (w) and stress (σ) along the fracture process zone in plane of the beams.

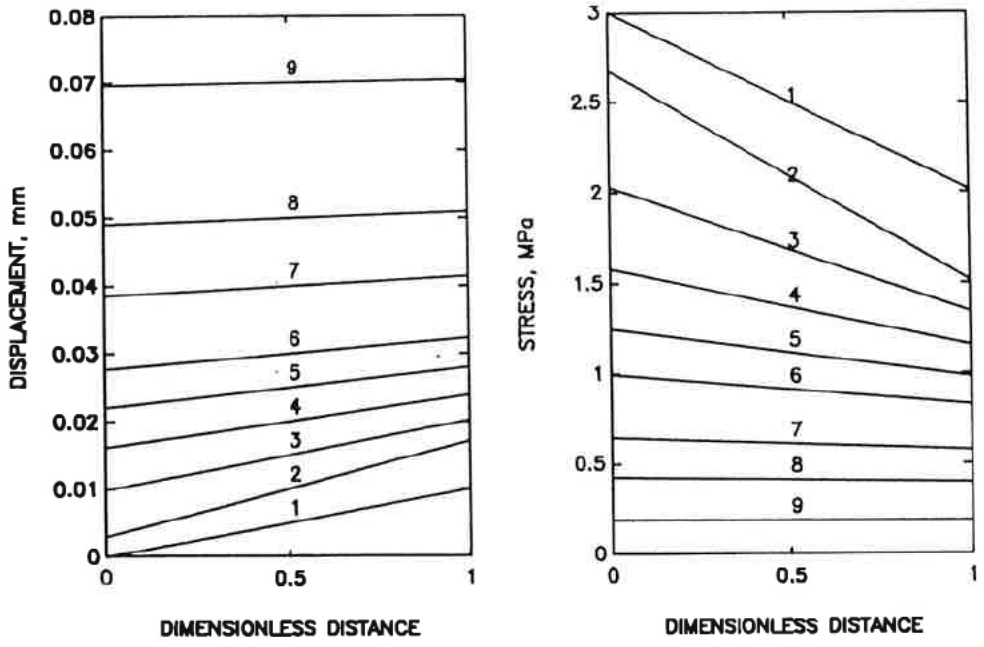

Fig. 3.8b. Development of the displacement (w) and stress (σ) along the fracture process zone in the plane perpendicular to the plane of the beams.

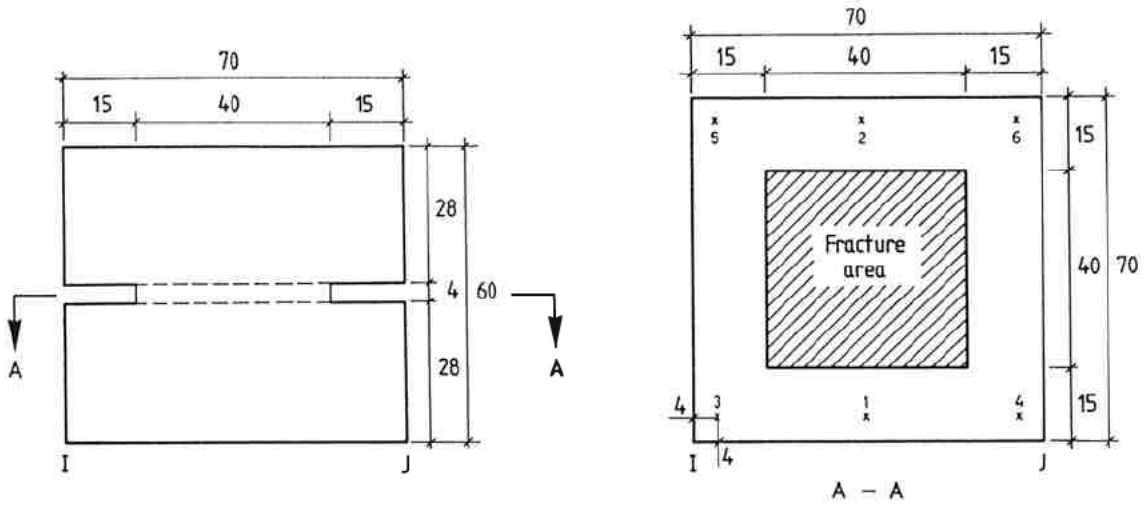

Fig. 3.9. Geometry of the specimen and locations of the clip gauges in the stability test.

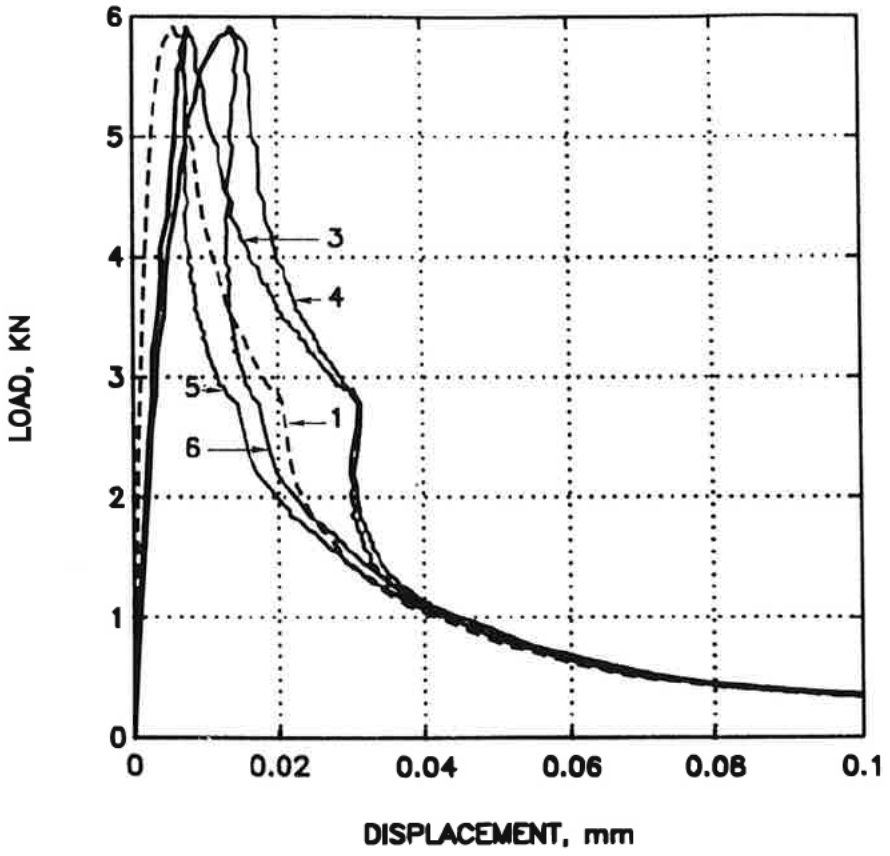

Fig. 3.10. Load - displacement curves recorded at different locations on the specimen.

Fig. 3.11b shows that at the peak load there is no instability in the plane perpendicular to the plane of the beams; note the slope of the first solid and dashed lines. However, shortly after the peak load the slope of the lines increases significantly, indicating the shift of the plane of instability. Furthermore, the figure shows that the instability of the test starts to diminish when the mean displacement approaches 0.030 mm.

In this case the instability of the tension test is also revealed by the "bump" on the mean curve, curve 1. However, it should be noted that the magnitude of the differences between the gauges could be less, if the gauges were placed in the immediate vicinity of the boundary of the fracture area. On the assumption that linear interpolation is allowed, the differences between the displacements recorded by gauges 3 (4) and 5 (6) could be reduced by approximately 35 percent. Nevertheless, this measure has no influence on the shape of curve 1, since the curve is already the mean value of the displacements on either side of the fracture area. Moreover, the results show that no compressive stresses occur on any parts of the fracture area.

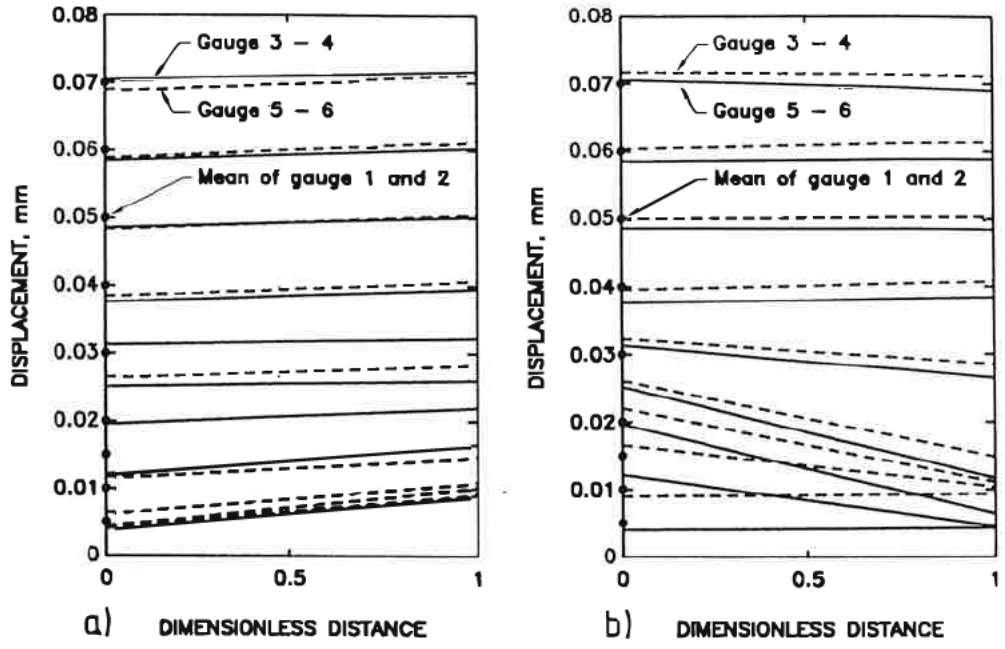

Fig. 3.11. Development of displacement along the fracture process zone; (a) in the plane of the beams, (b) in the plane perpendicular to the plane of the beams.

In this section, the governing role of the boundary conditions on the results of the tension test has been demonstrated. Moreover, an appropriate setup for such tests has been demonstrated. Although the test setup does not meet the requirements satisfactorily, it demonstrates that it

is possible to prevent the rotational instability of the tensile tests provided that the stiffness of the test arrangement satisfies the stability conditions. The result of the test shows that although the instability is not completely prevented, the displacement increases continuously anywhere along the fracture process zone and no reversible displacement is observed, which is indeed an improvement when determination of the tensile properties of fracture process zone is concerned. The design formulas (3.3) predicted the insufficient stiffness of the test arrangement. A comparison between the theoretical results and the results of the test shows that the design formulas are suitable tools for development of equipment with improved properties.

3.3 Fracture process zone exposed to normal and shear displacements - test methods

3.3.1 Introduction

As described previously, both normal and shear displacements may simultaneously occur within the fracture process zone, if the direction of the first principal tensile stress changes during crack propagation. Moreover, it was mentioned that applications of the models based on the displacement localization require the relation between the stresses and the displacements within the fracture process zone. There are several test methods developed, by which such relation can be determined. In this section some of the methods will only principally be described, while the major part is devoted to presentation of the test method developed within the current project.

3.3.2 Methods of testing

Methods of testing can principally be subdivided into two major categories, viz, methods where the external displacements (loads) are imposed in one direction and methods where the external displacements (loads) are imposed in more than one direction.

Fig. 3.12 displays some test configurations for the first category of test methods. This category of test methods cannot provide the material properties required by the FCM and similar models. However, they are suitable for verification of the models and the material properties which have been determined by means of the other test methods.

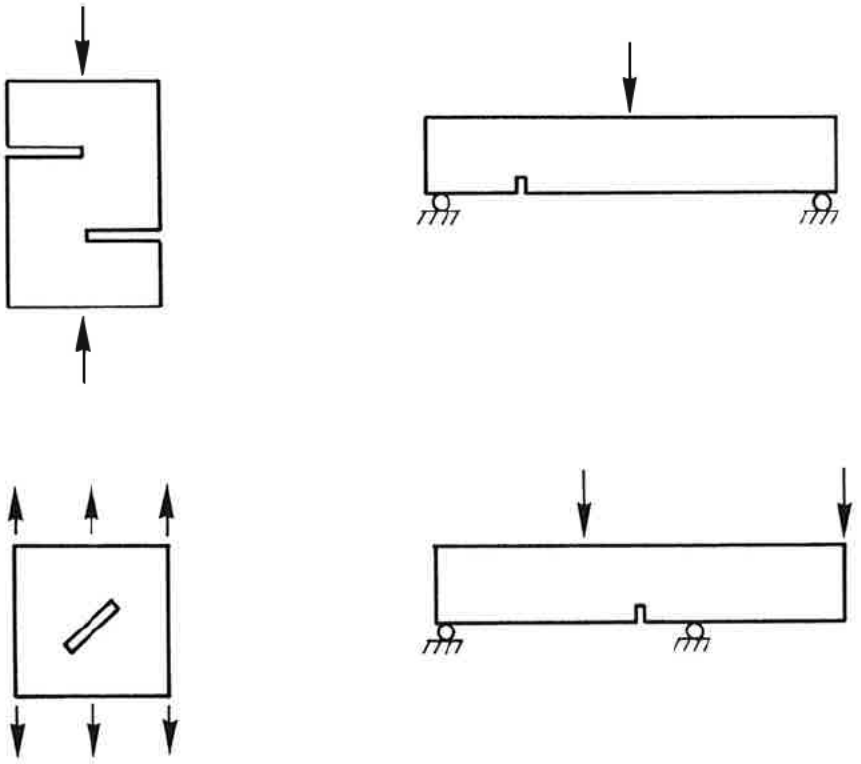

Fig. 3.12. Examples of tests where the displacements (loads) are imposed in one direction.

Fig. 3.13 displays the explanatory sketch of the second category of the test methods. In this category both normal and shear displacements (loads) are applied to the fracture process zone and are controlled externally. Several methods have been developed based on the mentioned principle. Here, some of the methods will briefly be described.

Fig. 3.14 displays the test arrangement used by Fenwick and Paulay, see Walraven (1978). Fig. 3.15a shows results of the tests. In these tests, a certain initial tensile crack was first imposed on the specimen. Afterward, shear loads were imposed stepwise; note the circles on the curves. At the end of each step, the test was stopped in order to adjust the normal displacement (crack width) back to its initial level by means of compressive load. The widths of the initial tensile cracks were varied within the interval 0.06 - 0.38 mm. Fig. 3.15b displays the displacement path of the tests, which can be obtained from Fig. 3.15a. The figure shows the area on the plane of the shear and normal displacement which is covered by the test series. By means of the test results, Fenwick and Paulay derived the following empirical expression which describes the shear stresses as a function of shear and normal displacements.

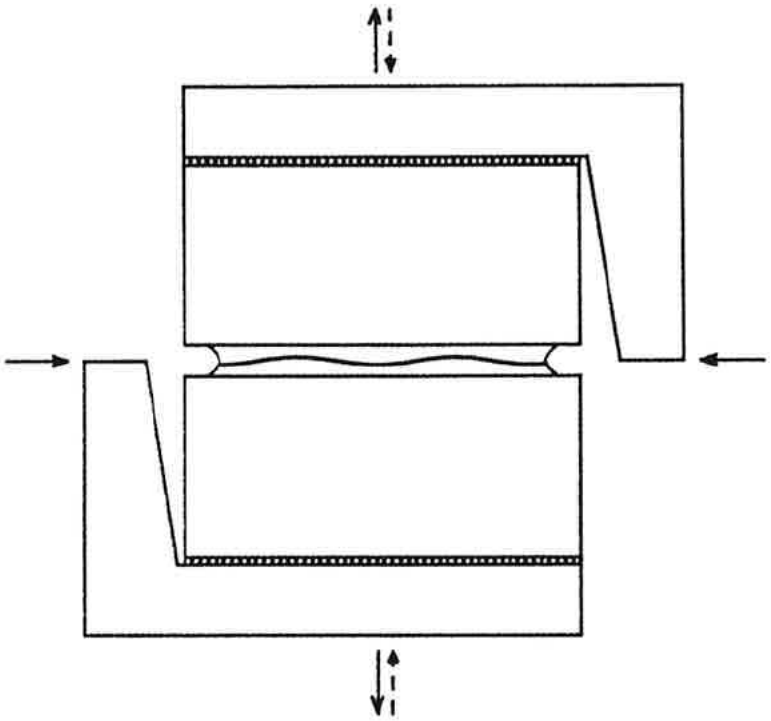

Fig. 3.13. Explanatory sketch of tests where the displacements (loads) are imposed in more than one direction.

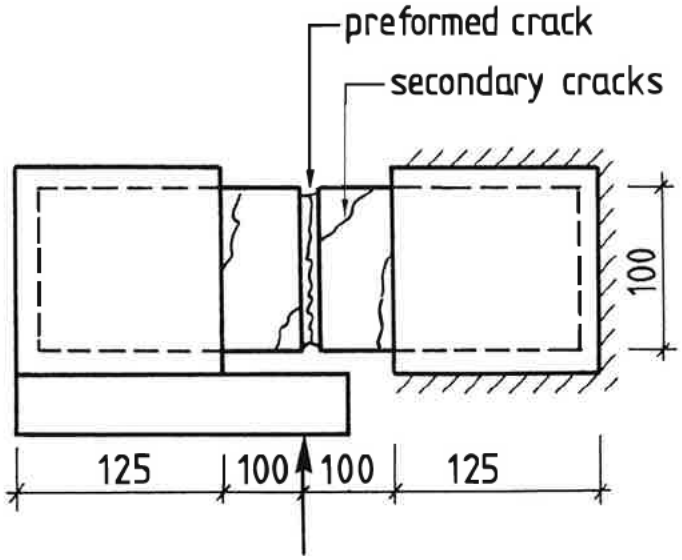

Fig. 3.14. Test equipment used by Fenwick and paulay, taken from Walraven (1978).

$$\tau = \left(\frac{0.928}{w} - 0.6584\right)\left(\sqrt{f_{cc}} - 1.4465\right)(\delta - 0.0436w) \qquad 3.4$$

τ is shear stress (N/mm^2), w and δ are normal and shear displacements (mm), f_{cc} is the compressive strength (N/mm^2). No expression is given for normal stresses.

Fig. 3.16 displays the test arrangement used by Houde and Mirza, which can also be found in Walraven (1978). The tests were carried out in the same manner as the tests according to Fenwick. By means of the test results Houde and Mirza derived the following empirical expression for the shear stress.

$$\tau = 2.06\left(\frac{1}{w}\right)^{\frac{3}{2}}\delta \qquad 3.5$$

Figs. 3.17a and 3.17b display the test arrangement used by Walraven (1980). In the tests of Walraven the push-off type of specimens was used. Prior to the shearing, tensile cracks with a certain width were imposed on the specimens. In the following stages the specimens were restrained in the direction perpendicular to the shear plane. Two types of restraint were used, namely external restraint by means of rods and internal restraint by means of stirrups, which are illustrated in the figures. The external restraint rods were also served both as load cells for measurements of the restraining stress, i.e. the compressive stress developed over the shear plane, and an instrument for adjustment of the restraint stress normal to the crack plane. Fig. 3.18 displays some of the results of Walraven achieved by the method based on external restraint. In the figure σ and τ are normal and shear stresses and w and Δ are normal and shear displacements. The numbers close to the curves are the identification numbers, where the first number describes the quality of the concrete, which in this case is a concrete with 16 mm maximum aggregate size and with approximately 33 MPa compressive strength. The second number is the initial crack width in mm, prior to the shearing. The third number is restraint stress at normal crack width of 0.6 mm. Walraven has also derived the following empirical expressions which give the normal and shear stresses as a function of both normal and shear displacements.

$$\sigma = -\frac{f_{cc}}{20} + \left(1.35w^{-0.63} + \left(0.191w^{-0.552} - 0.15\right)f_{cc}\right)\delta$$

$$\tau = -\frac{f_{cc}}{30} + \left(1.80w^{-0.80} + \left(0.234w^{-0.707} - 0.20\right)f_{cc}\right)\delta \qquad 3.6$$

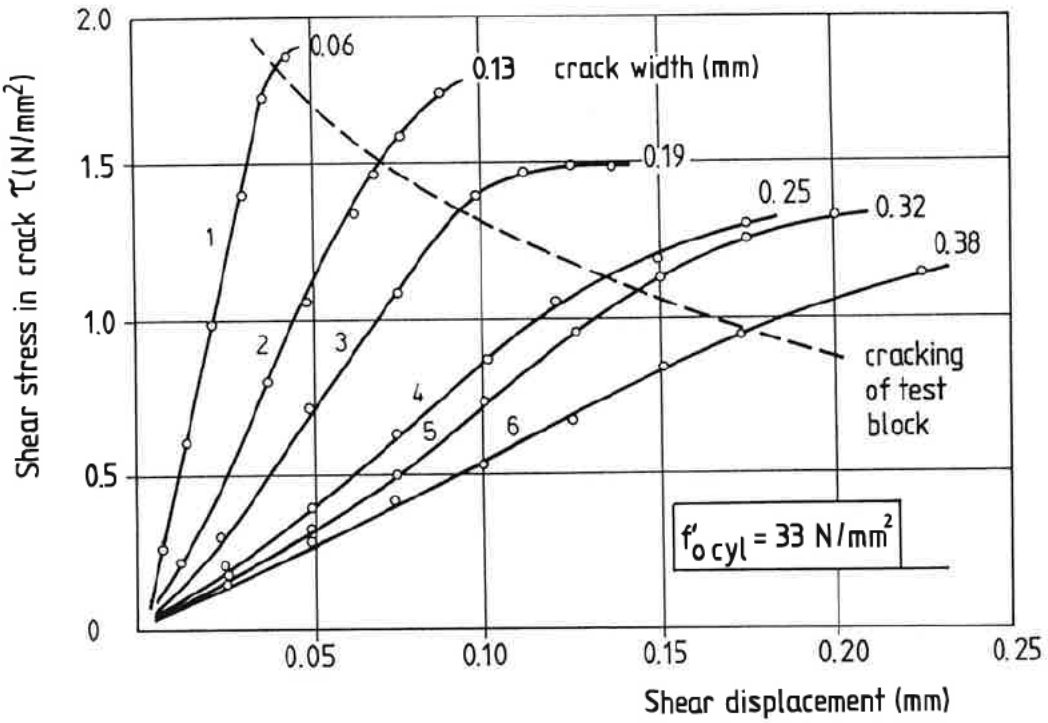

Fig. 3.15a. Results reported by Fenwick and Paulay, taken from Walraven (1978).

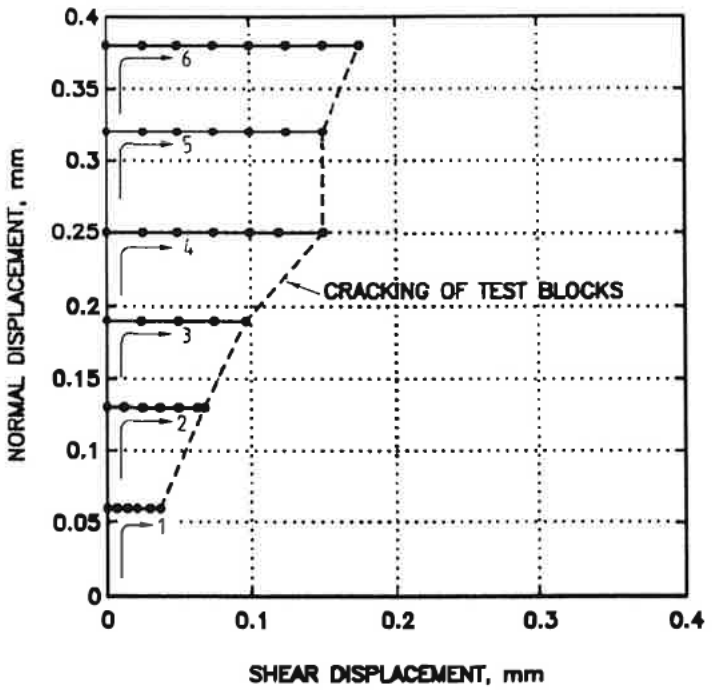

Fig. 3.15b. Displacement path of the tests reported by Fenwick and Paulay, obtained from Fig. 3.15a.

The above-mentioned methods cannot perform the combined normal and shear tests in such a way that both quantities can be varied simultaneously and continuously during the tests. However, as far as the author is aware, since the mid-eighties two independent projects have been going on with the objectives to develop an equipment which can simultaneously and continuously adjust the normal and shear quantities. One of these projects is going on in Stevin Laboratory in Delft, Netherlands and the other one is the present project. The equipment which is being developed in Stevin Laboratory is displayed in Fig. 3.19. The equipment contains two actuators which can adjust the displacements in two directions. Both actuators are servo-controlled and can be run so that a desired load path or displacement path can be obtained. The details of the equipment will not be discussed here, but can be found in Reinhardt et.al. (1987). Some results of the tests conducted with this equipment are displayed in Fig. 3.20, see van Mier et.al. (1989). In these tests, the specimens were cracked in tension. After achievement of a certain crack width which is indicated on the curves, normal load was applied to the specimens. Two load levels were tested, viz zero normal load, Fig. 3.20a, and 1000 N compressive normal load, Fig. 3.20b. Shearing started when the desired normal loads were achieved and continued under constant normal load.

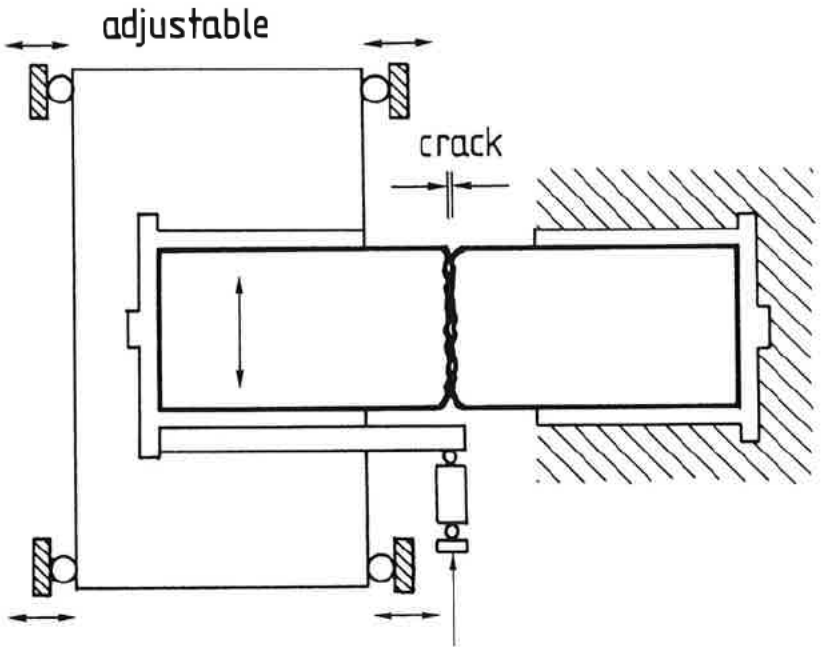

Fig. 3.16. Test equipment used by Houde and Mirza, taken from Walraven (1978).

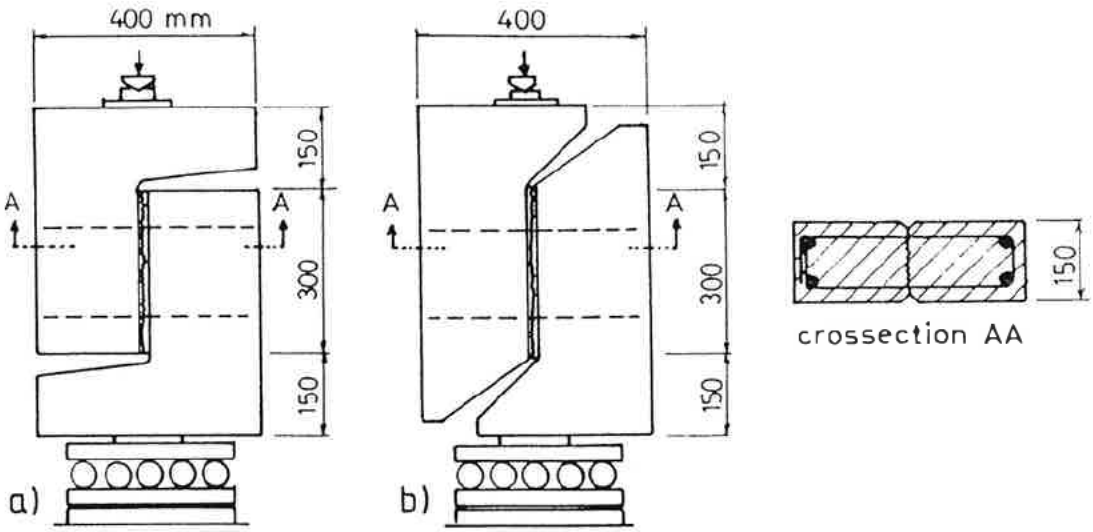

Fig. 3.17. Test arrangement used by Walraven.

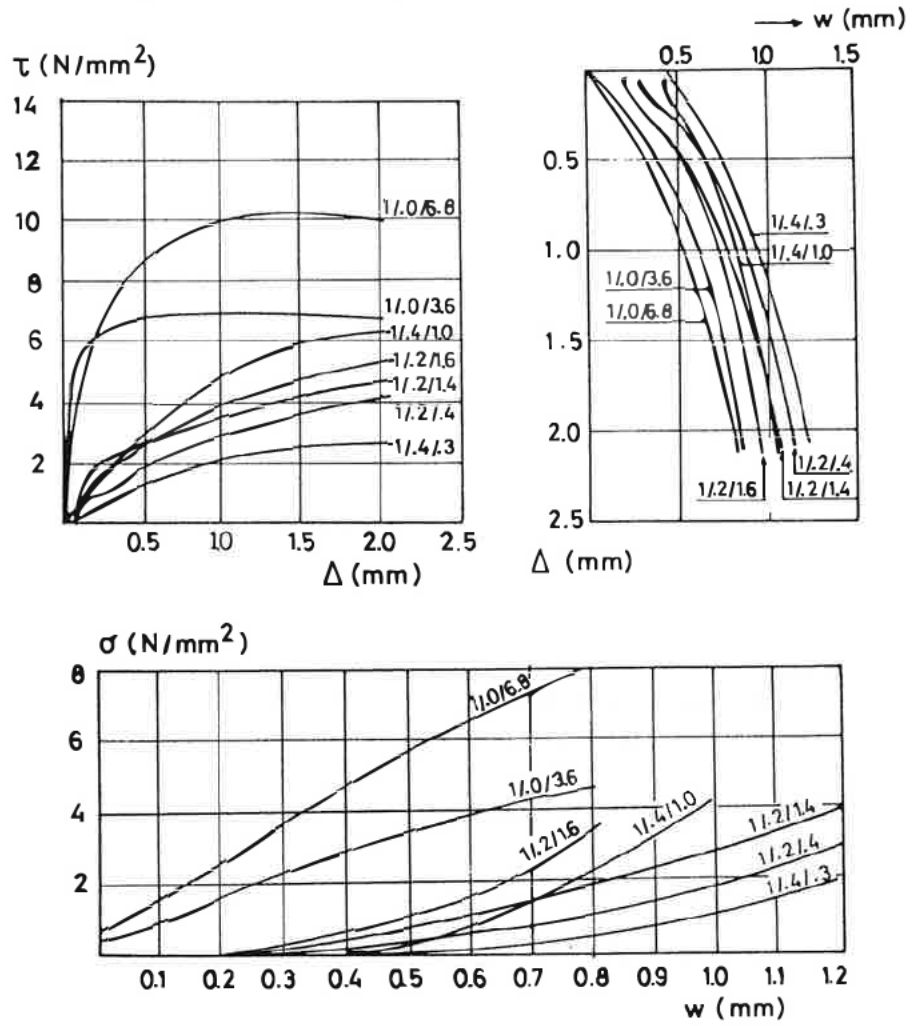

Fig. 3.18. Some of the results reported by Walraven.

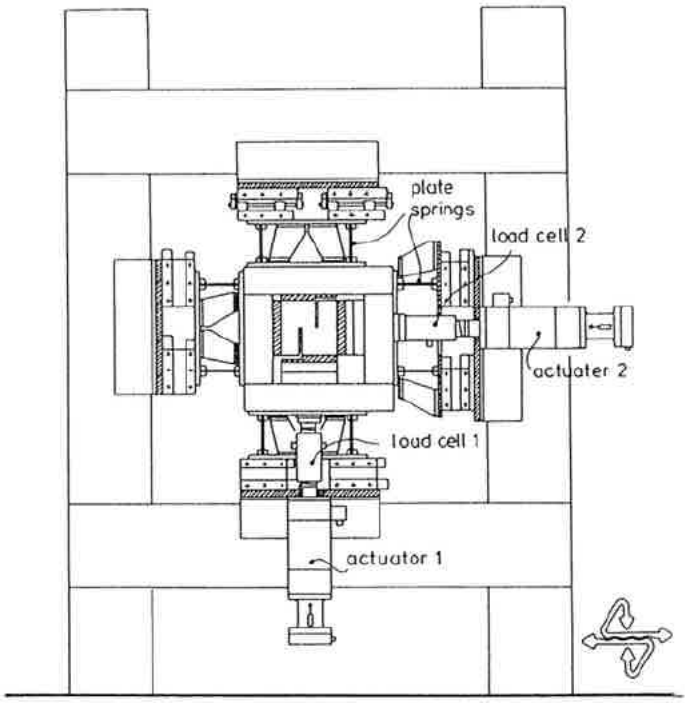

Fig. 3.19. Equipment developed in Stevin Laboratory.

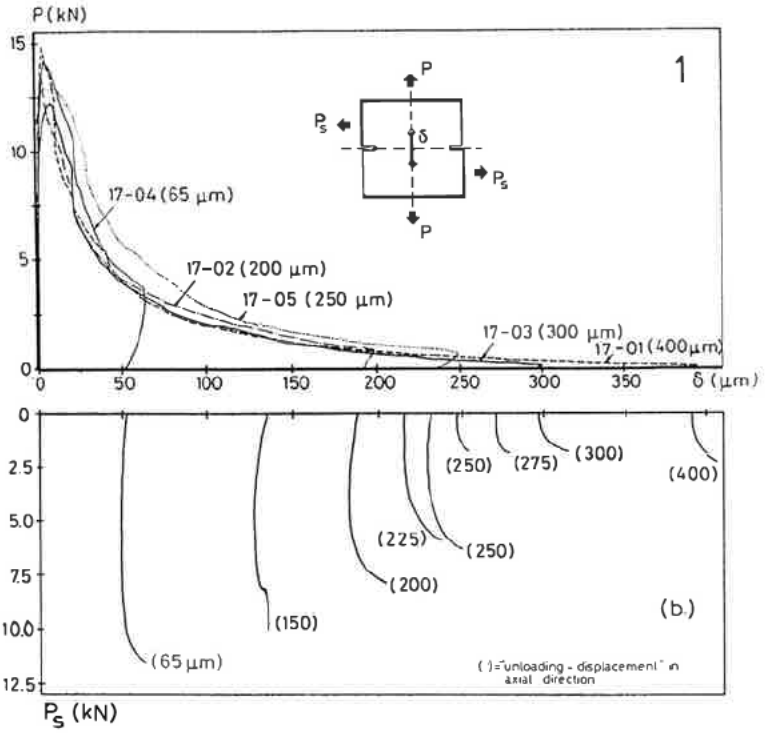

Fig. 3.20a. Load - displacement curves at constant zero normal load.

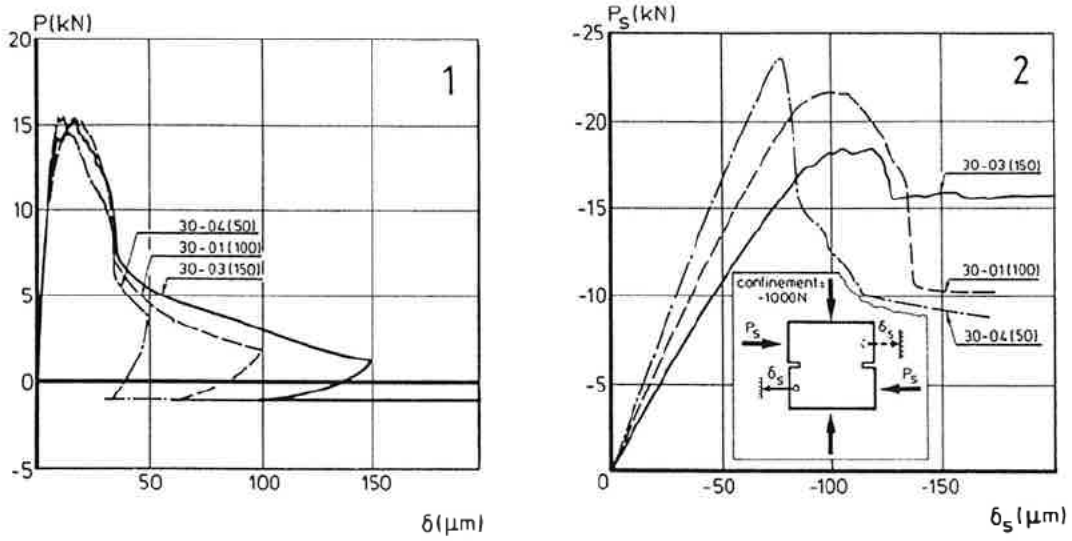

Fig. 3.20b. Load - displacement curves at constant compressive normal load, P=-1000 kN.

3.3.3 Test method developed in this project

Fig. 3.21 displays a sketch of the test equipment which was developed in this project. The function of the equipment was briefly described previously. However, details of the equipment will be described below.

As is displayed, the equipment is composed of two box-beams (1), which are connected at their ends by a thin steel sheet (2). This equipment is connected to a closed-loop and servo-controlled testing machine, which via the connection points (3) imposes the normal displacements. Shear is imposed by rotating the crank (4). The rotation of the crank is transferred by means of a flexible axle (5) to a gear box (6), which lowers the rotation. The rotation is changed into pure translation by means of a nut (7) which moves along a steel bar (8) towards a roller (9). Due to forward movement of the nut on the bar, the lower beam will be pushed via the roller, a freely sliding support (10) and a fixed support (11), while the upper beam becomes pulled via fixed support (12). Since the beams are connected via hinges to the testing machine they will rotate around their connection points. Rotation of the beams is, however, resisted by the specimen (13), which will cause shear displacements in the specimen. The specimen is glued in between two replaceable steel plates (14), which are fastened to the equipment by bolts. The lock (15) serves as a safety arrangement for transportation of the equipment and for restraint of the movement of the beams perpendicular to their plane.

The normal load is recorded by means of the load-cell of the testing machine, while the shear load is recorded by means of the strain gauges attached on the steel bar. Since the axis of the steel bar is on the plane of the fracture plane, the shear forces will not cause any moment on the fracture plane.

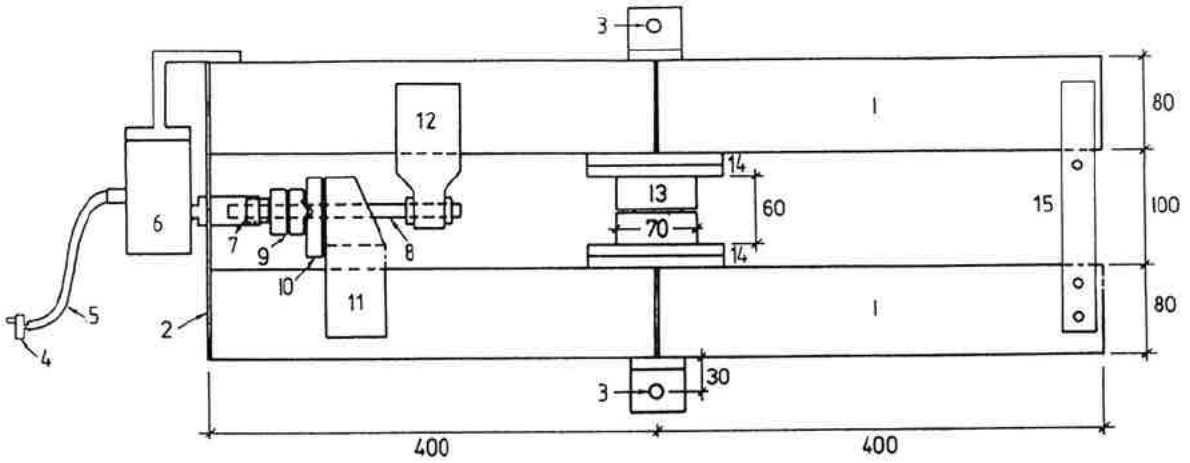

1- Box beams (height=80 mm, width=40 mm thickness=3 mm)
2- Steel sheet (height=260 mm, width=100 mm, thickness=1 mm)
3- Connection to the testing machine
4- Crank
5- Flexible axle
6- Gear box
7- Nut
8- Steel bar with strain gauges
9- Roller support
10- Freely sliding support
11- Fixed support
12- Fixed support
13- Specimen
14- Steel plates
15- Lock and freely sliding support

Fig. 3.21. Sketch of the test equipment developed in this project.

Fig. 3.22 displays the geometry and size of the specimen which is used in this investigation. In the figure, the locations of the clip gauges is also demarcated. The mean normal displacement is recorded by gauges 1 and 2 and the mean shear displacement is recorded by gauges 3 and 4. This configuration is kept throughout the investigation.

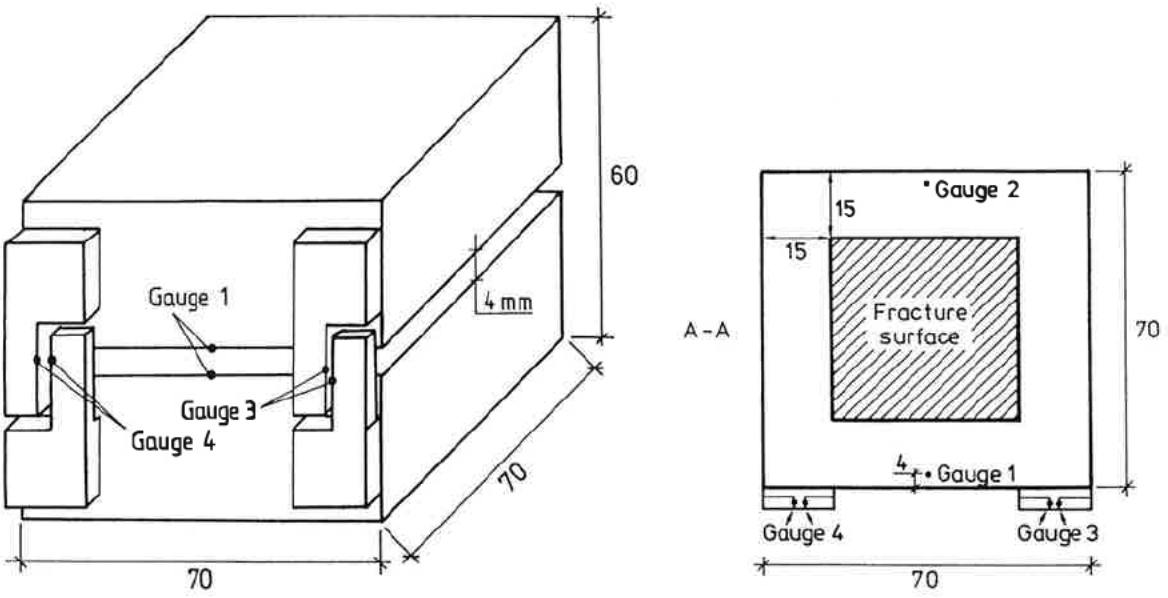

Fig. 3.22. Specimen geometry and locations of the clip gauges, in mm. Normal displacements are recorded by gauges 1 and 2. Shear displacements are recorded by gauges 3 and 4.

Fig. 3.23 shows the connection of the test equipment to the testing machine. Fig. 3.24 shows the attachment of the gauges to the specimen.

Clip gauges for the measurement of normal displacements are placed inside the notches, approximately 4 mm from the edges of the specimen, see Fig. 3.22. Fig. 3.25 displays in an exaggerated manner the interior of a notch. As is demonstrated, the edges of the clip gauges are only in touch with the PTF- (Poly Tetra Fluor Ethene) layers. The PTF-layers serve primarily as a slip layer to reduce the impact of the movements of the notch surfaces caused by shear on the accuracy of the measurement of the normal displacements. The PTF-layers serve secondarily as levelling plates in order to reduce the asperities on the notch surfaces and relative inclination of the notch planes. The position of the clip gauges is fixed by means of supports which are mounted close to the specimen on the lower part of the equipment.

Clip gauges for the measurement of shear displacements are also fixed in the same manner as clip gauges for normal displacements. However, the edges of the clip gauges together with a layer of PTF are inserted into the gap of the steel holders which are glued on the surface of the specimen, see Fig. 3.22. The holders are composed of two parts, see Fig. 3.26. As is demonstrated in Figs. 3.22 and 3.26, each part of the holder is attached to the specimen via 225 mm^2 gluing surface. As can be observed, the gluing surface is large and occupies a

relatively large area on the specimen surface. The large gluing surface is chosen in order to achieve sufficiently strong and stiff adhesion to the moist specimen surface. A consequence of this is that the displacements recorded by the clip gauges do not refer to the relative displacements between two points, but between two surfaces. Furthermore, the measured relative displacements include, besides the shear displacements of the fracture process zone, also the shear displacements which occur outside the fracture process zone. If linear elastic behaviour is assumed for the material located outside the fracture process zone, the imposed error at the maximum shear stress, which has been observed during the entire investigation, is approximately 0.004 mm. However, it should be noted that in some cases non-linear elastic behaviour is expected for the material located outside of the fracture process zone. This is caused by the secondary cracking of the specimen, which will be described later.

The equipment and the testing machine build a test setup which is able to impose normal and shear displacements (stresses) to the specimen. This setup is, however, semi-automatic, viz the normal displacements are imposed by the testing machine while the shear displacements are imposed manually. The tests can be conducted in several ways; some examples are given below.

The test can be run in a total displacement-controlled manner with a prescribed relationship between normal displacement and shear displacement. In practice this is done in the following way. The displacements are recorded by means of an X-Y recorder on which a prescribed displacement path is drawn; see dashed curves, or paths, 1 and 2 in Fig. 3.27. Consider path 1 first. During the test the testing machine imposes the displacement to the specimen with the programmed rate. By manually adjusting the rotation rate of the crank, it is possible to impose shear displacements which satisfy the relation displayed on the X-Y recorder. The same technique can be used for path 2, whereas in segment B the testing machine is on hold and in segment C there is no need to rotate the crank.

The tests can also be conducted in a load-controlled manner. However, as far as the tensile fracture process zone is concerned this is only possible when the fracture zone is developed and normal stress has turned over to compression. In this case the method of conduction is the same as above, but the X-Y recorder registers the loads instead of displacements. In the next chapter the experimental program and the tests which have been carried out with this equipment will be presented.

As mentioned earlier the specimens are glued to the equipment. The adhesive which is used is a two component epoxy, with three hours setting time.

In this investigation specimens were made of ordinary medium strength mortar and concrete, with the geometry shown in Fig. 3.22. The mix proportions of the mortar and concrete are given in Tab. 3.1.

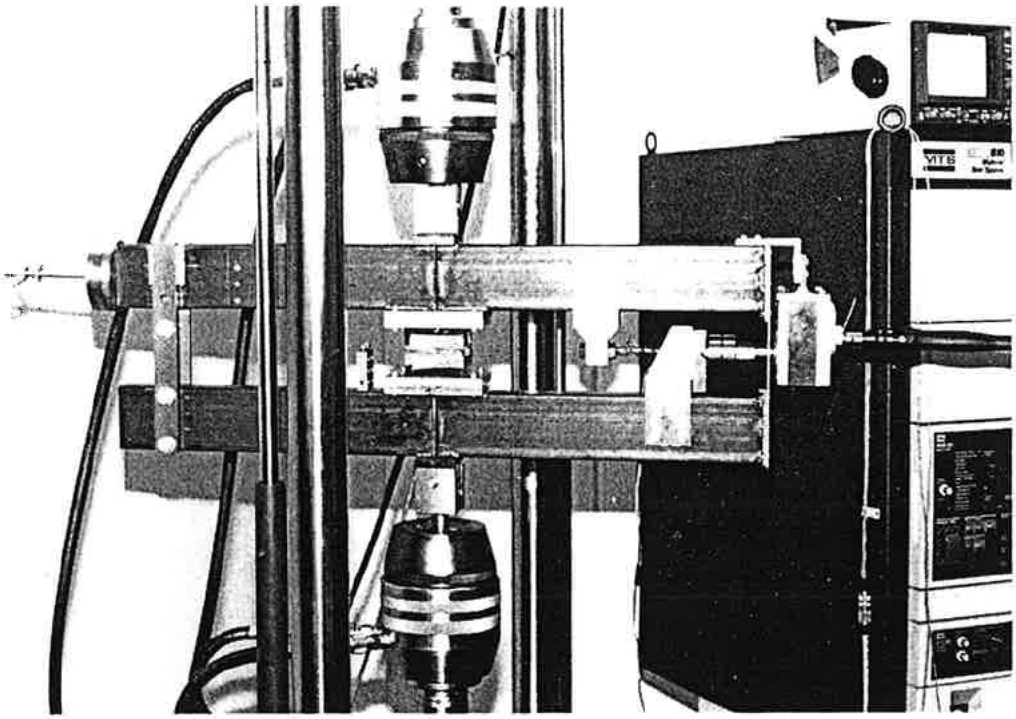

Fig. 3.23. Connection of the test equipment to the testing machine.

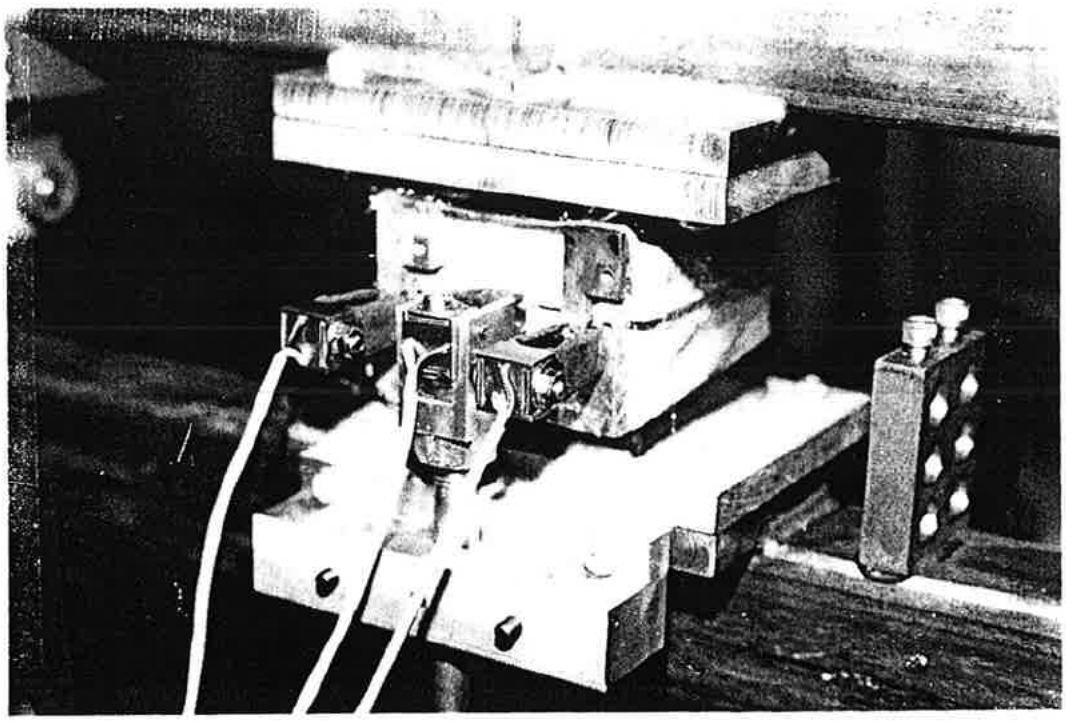

Fig. 3.24. Attachment of the clip gauges to the specimen.

COMPONENTS	MORTAR (kg/m^3)	CONCRETE (kg/m^3)
Water	200	200
Cement	400	400
Sand 0 - 2 mm	978	871
Crushed quartzite 2 - 4 mm	800	640
Crushed quartzite 4 - 8 mm	0	267

Tab. 3.1. Mix proportion of the mortar and the concrete.

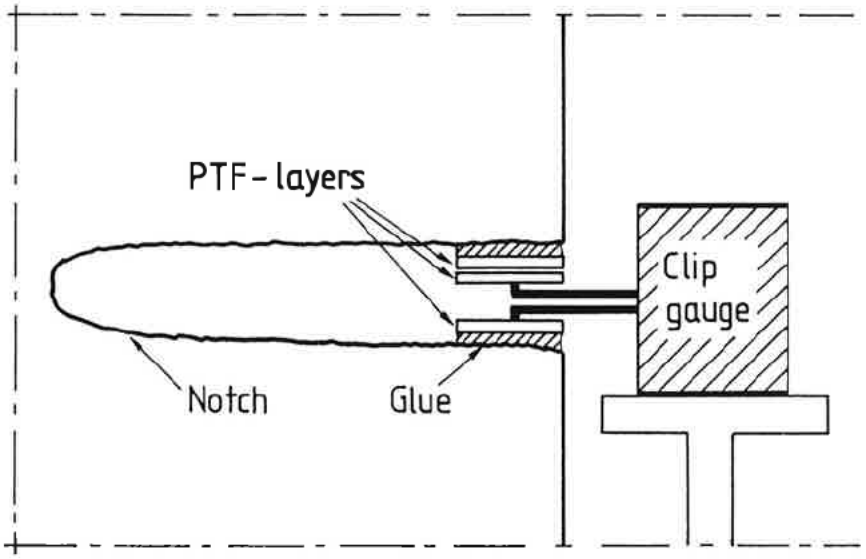

Fig. 3.25. Interior of a notch.

The compressive strength of both mortar and concrete was determined by means of water-cured, 150x150x150 mm^3 cubes at age of 28 days. The compressive strength of both materials was approximately 50 MPa.

The specimens were cast in a steel mould and were unmoulded 24 hours after casting. Most of the specimens were stored in water until the day before testing and were tested in wet conditions at the age of 28 days. In some tests, however, the conditions deviate from the described conditions, which will be pointed out successively when it is necessary. Notches were sawn by means of a diamond blade at the age of at least 21 days. Since gluing of the specimen to the testing equipment requires a sufficiently dry surface, the specimens were

taken out of the water a day before testing. However, in order to prevent shrinkage stresses close to the fracture zone, wet non-woven fabrics were inserted into the notches to compensate for the loss of moisture. Furthermore, all surfaces of the specimen except for the gluing surfaces were covered by several layers of elastic tape to prevent evaporation from the specimens. The elastic tape was not removed until the tests were completed.

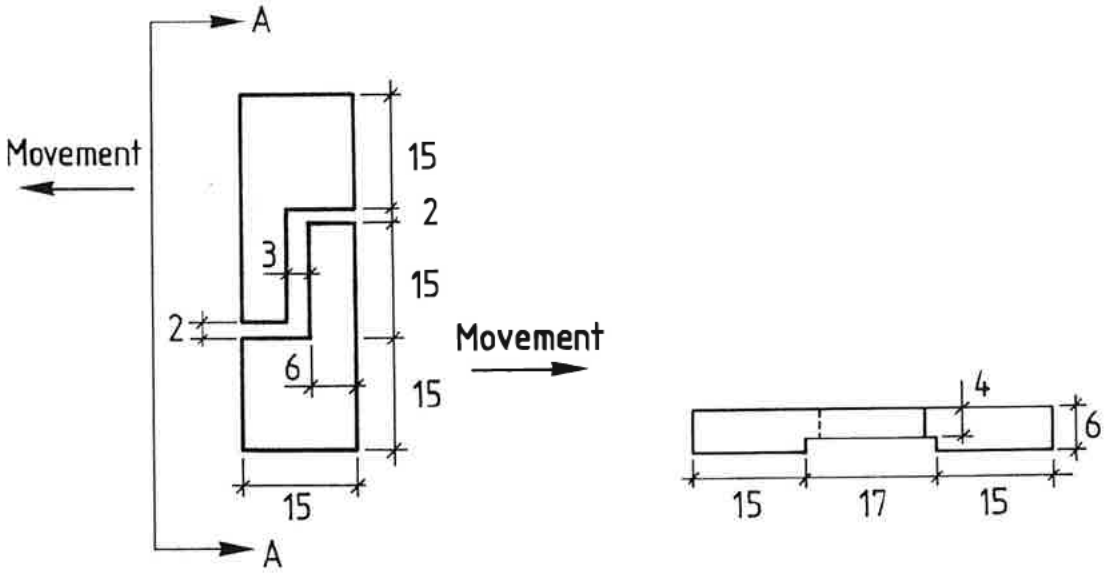

Fig. 3.26. Holders for clip gauges recording shear displacements.

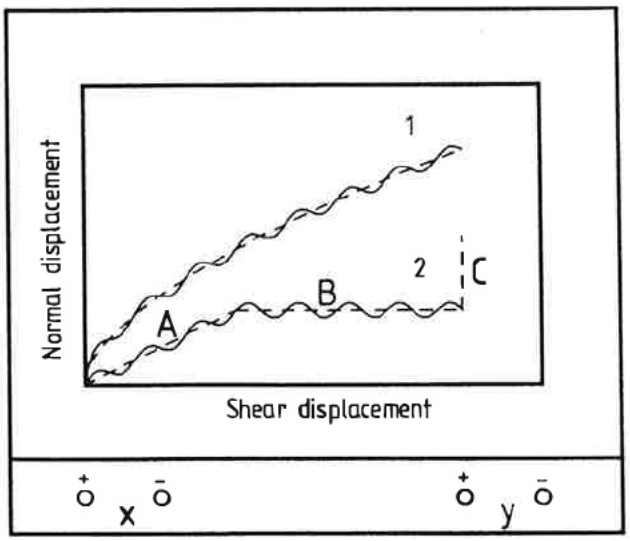

Fig. 3.27. X-Y recorder and examples of test paths.

4 Presentation of the test results

4.1 Introduction

In this chapter the results of the tests carried out with the equipment described in the previous chapter will be presented. Besides the test results, this chapter discusses crack formations within the specimen and its influences on the measured properties. Furthermore, the chapter explains some of the phenomena observed by means of an analytical model. Finally, the results of this investigation are compared with those described in Chapter 3.

4.2 Performance of the tests and general notations

One of the difficulties associated with combined normal and shear tests is the choice of the test path. By path is meant the function which describes the relation between normal and shear displacement during the entire test. Fig. 4.1 displays the δw-plane on which the displacement paths of any combined normal and shear tests can be plotted. This also includes tests where the load path has been the governing relationship. The origin of the coordinate is in point $w=\delta=0$, which coincides with the instant when a tensile fracture process zone has just been formed. Since the displacement path is not a property of the material, but a property which depends upon the geometry, composition and boundary condition of the structure, an infinite number of displacement paths can be expected to occur in practice. However, the number of paths can be significantly reduced, if only the cases of monotonic increasing normal and shear displacements and the simplest possible mathematical functions are considered. The equations below are two functions which have been chosen arbitrarily in order to control the tests.

$$w = (\tan\alpha)\,\delta \qquad 4.1$$

$$w = \beta\sqrt{\delta}$$

The first equation specifies a linear relation between normal and shear displacements, while the second equation specifies a parabolic relation between the displacements. It has been considered that in a real structure, the rate of the shear displacement ($d\delta/dw$) is zero at the instant of the initiation of the fracture process zone, and increases successively to higher values. Therefore, the description of the displacement paths through parabolas is more realistic than straight lines, which have a constant displacement rate from the instant of the initiation of the fracture process zone to the end of the test. Hence, most of the investigation

has dealt with the parabolic paths. It should be noted that there are infinite numbers of functions which satisfy the condition of gradually increasing rate, but the described parabola has been considered to be the simplest function for these tests. The variables α (degree) and β ($mm^{1/2}$) specify the set of relations which has been used. Both variables have been varied in a wide range, viz $30<\alpha<75$ and $0.4<\beta<0.9$, see Fig. 4.1. Both α and β are limited downward because in the cases of $\alpha<30°$ and $\beta<0.4$ $mm^{1/2}$ the specimens failed due to secondary crack formations, which are described in the next section.

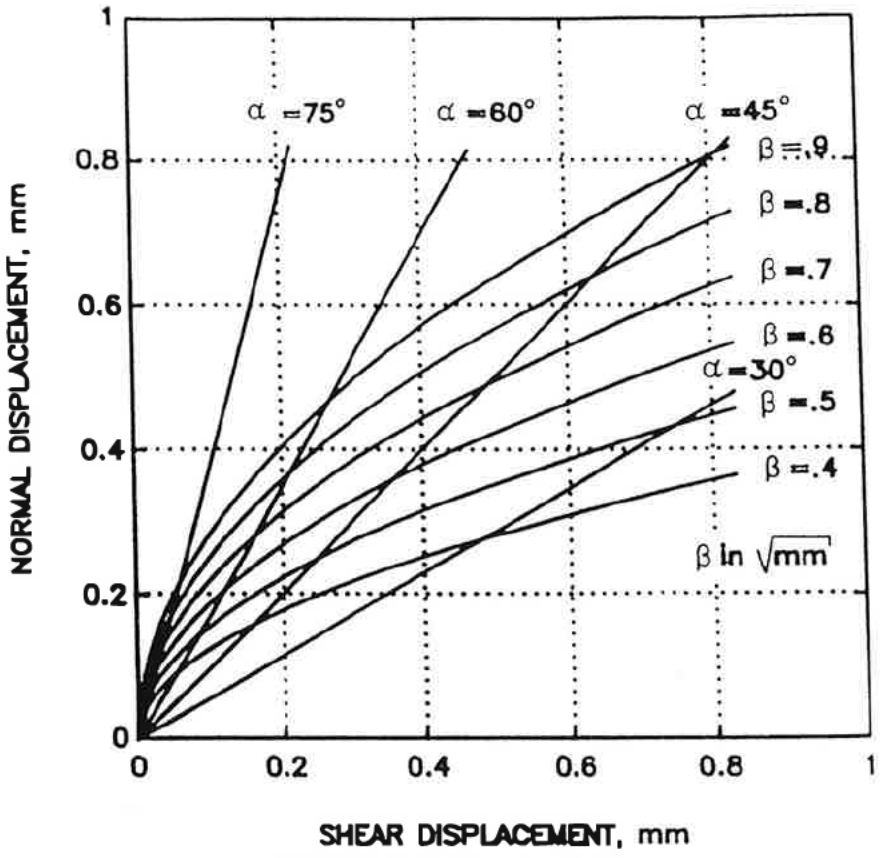

Fig. 4.1. Different displacement paths on the δw-plane.

It is not clear to the author whether the described paths reflect reality fairly. However, this possibly can be verified in two ways, namely by means of measurements of the normal and shear displacements of the several types of structures and by numerical simulations of the failure of the structures. The measurements are difficult to conduct, firstly because it is normally difficult to predict the trajectory of curvilinear crack propagation and secondly because the area near the crack is often densely cracked. Holographic measuring instruments may be very helpful in these cases. The numerical methods can be uncertain in the sense that

in order to predict true crack trajectory and true stress field around the crack, one needs to have firstly a reliable model and software which can handle a complex crack pattern and secondly access to material properties which do not deviate much from the true material properties. The later however requires, co-ordination between the analyses and the experiments. Such verifications have not been done in this investigation.

In Fig. 4.2 results of a test with a concrete specimen at the age of 28 days is displayed. Throughout the test, the specimen was subjected to monotonic increasing normal displacement. Prior to the maximum tensile stress, no shear displacements were imposed. However, when the maximum was reached the shear displacements were also imposed on the specimen, marked in Fig. 4.2a. During the test, the rate of the shear displacement was adjusted manually so that the desired relation between normal displacement and shear displacement could be obtained, noting that the normal displacements prior to the maximum tensile stress were discounted. Figs. 4.2a and 4.2b show the relation between stresses and displacements in each direction. It should be noted that the displacement in Fig. 4.2a refers to the total displacement (γ), not (w). Fig. 4.2c shows the relation between shear displacement (δ) and normal displacement after the maximum tensile stress (w), i.e. the displacement path, which is a parabola with $\beta=0.5$ mm$^{1/2}$. In the figure two curves are shown, viz the dashed curve is the desired relationship and the solid curve is the registered relationship during the test, which demonstrates the accuracy of the control mechanisms.
As can be observed, the stress - displacement curves are rough, especially at the end of the test. In order to facilitate determination of mean curves of several tests and improve the clearness of the diagrams, most of the curves presented in the following sections are smoothed, as is demonstrated in the figures.

Since the tests were very time consuming, they were run with variable rates. Fig. 4.3 shows variation of the rate of the normal displacement during the tests. As is demonstrated, during the most critical parts of the test, i.e. the first part of the descending branch of the normal stress - normal displacement curve, the rate was low. The displacement rate was increased successively when the critical part was left behind.

4.3 Crack formation

One of the major difficulties which the author was confronted with during the present investigation was the observation of the crack formation. Since the specimens were small, four-sided notched, covered with elastic tape and inserted with different measuring devices, observation of crack formations was not possible during the tests. However, most of the specimens were inspected visually after the tests. The inspection of the specimens revealed two types of crack systems, namely primary crack system and secondary crack system.

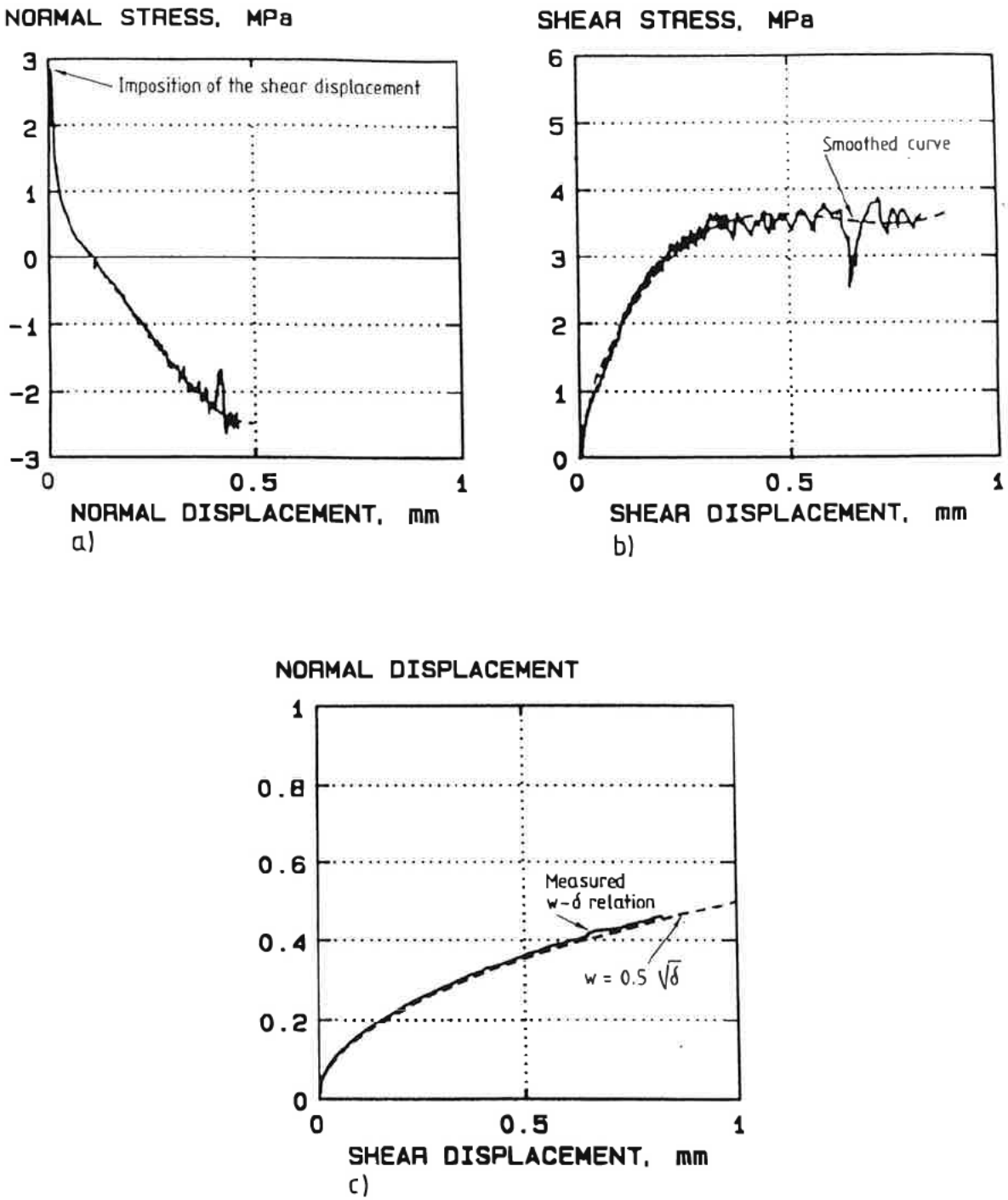

Fig. 4.2. Output of combined normal- and shear- displacement test. Parabolic path (β=0.5 $mm^{1/2}$).

Primary crack system includes the cracks within and in the immediate vicinity of the primary fracture process zone. By primary fracture process zone is meant the first zone which is formed within the volume delimited by the notches when the tensile normal stress approaches the tensile strength of the material, before imposition of shear. It should be noted that in the

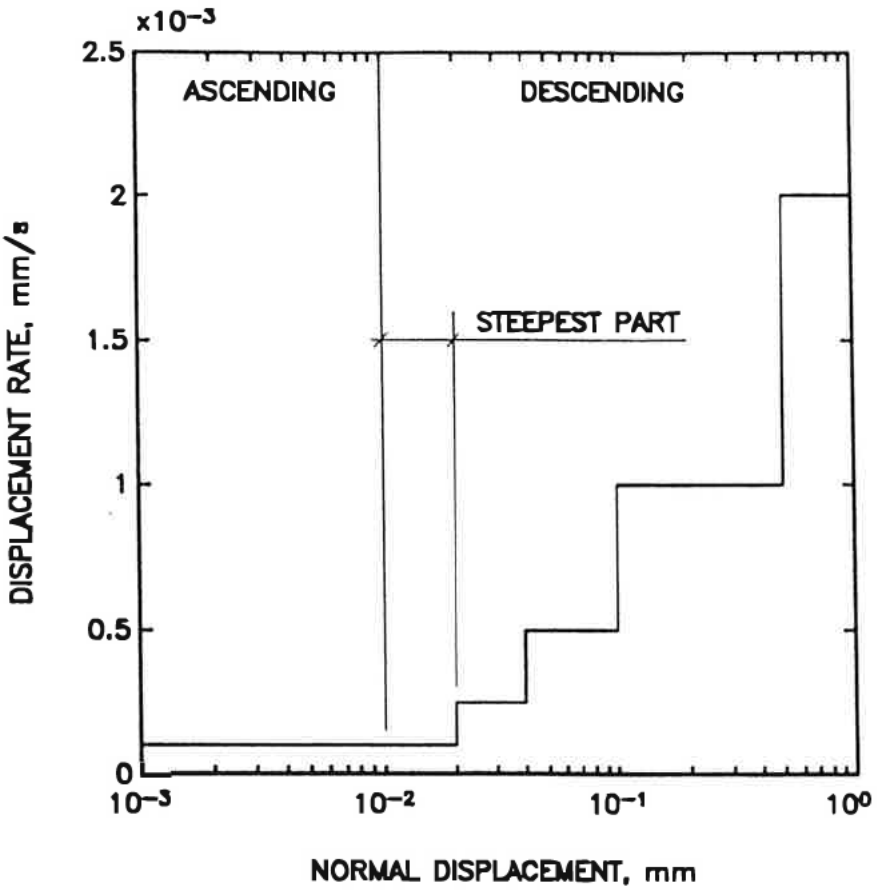

Fig. 4.3. Variation of the rate of normal displacement (γ) during the tests.

case of zero shear the final crack path will be inside the primary fracture zone.

Fig. 4.4 demonstrates the primary fracture process zone and the possible crack paths (solid lines). The secondary crack system includes cracks outside the primary fracture process zone, i.e. the cracks which occur after imposition of shear. In the same way the secondary fracture process zone can be defined, i.e. the fracture process zone which is formed outside the volume delimited by the notches. Fig. 4.4 demonstrates a possible secondary crack path (dashed line).

Figs. 4.5 and 4.6 display results of some preparatory experiments, before the start of the main series. The tests were carried out on concrete specimens at 7 days of age. Fig. 4.5 displays results of a test with the displacement path $\alpha=30°$. The specimen in this test failed due to diagonal crack. Fig. 4.6 displays the result of another test, where the normal displacement (γ) was kept constant at 0.008 mm, the maximum normal tensile stress (σ) was achieved at 0.006 mm. In this test the specimen also failed due to diagonal cracks at the end of the test.

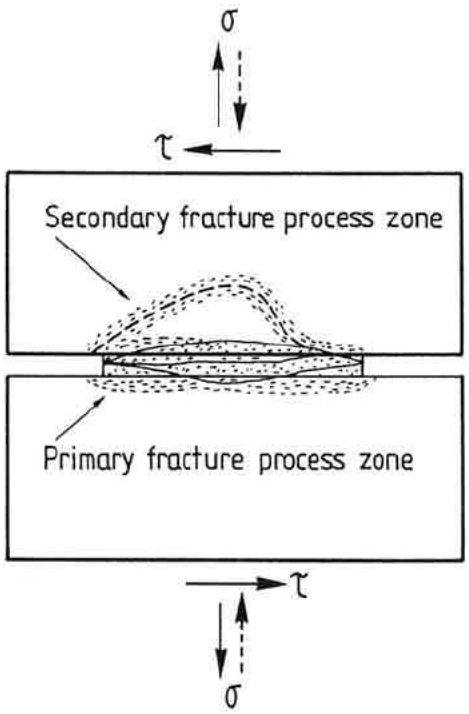

Fig. 4.4. Definition of the primary and secondary fracture process zone, and crack paths.

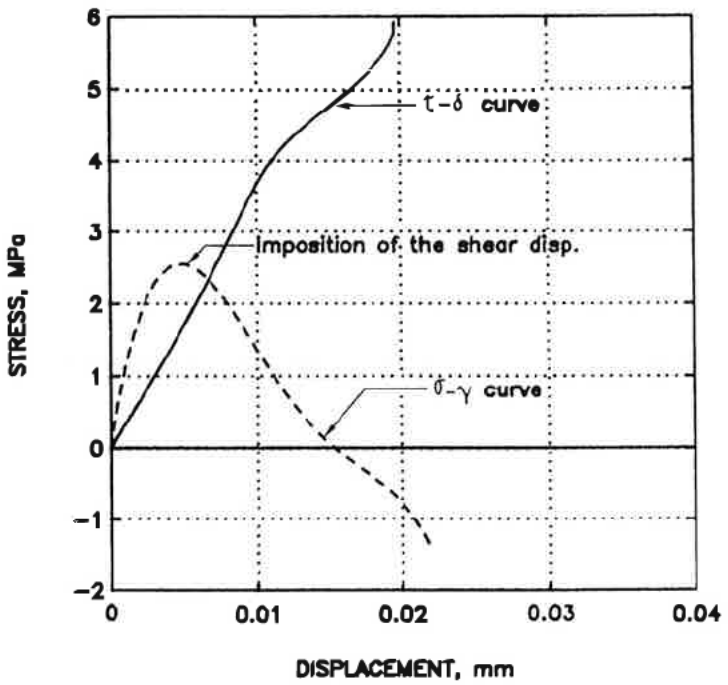

Fig. 4.5. Stress - displacement (σ-γ and τ-δ) curves for test with linear displacement path (α=30°).

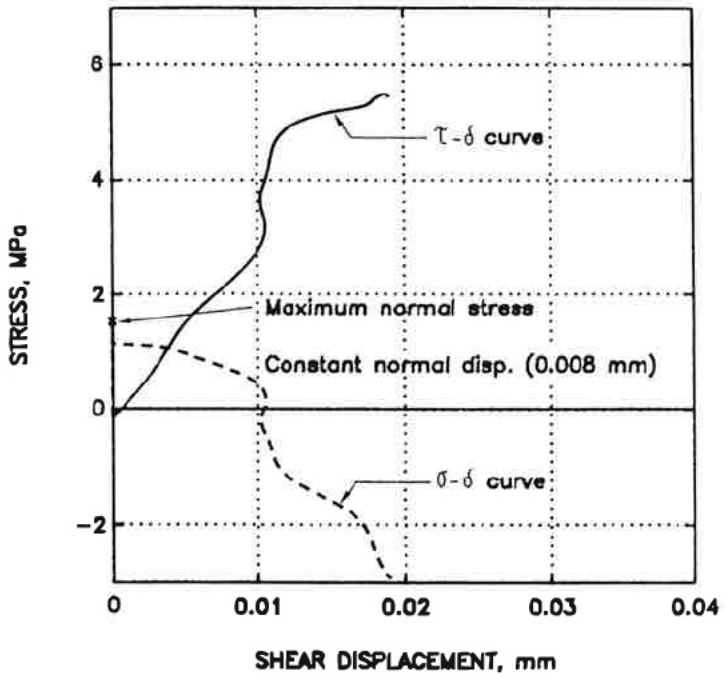

Fig. 4.6. Stress - displacement (σ-δ and τ-δ) curves for test with constant total normal displacement (γ=0.008 mm).

Fig. 4.7a shows a case where the specimen failed due to the diagonal cracking, which indeed is a type of secondary crack formation. Fig. 4.7b is a close-up of the area inside the notch which shows a crack inside the volume delimited by the notch. The crack is perpendicular to direction of the normal stress. Furthermore, the crack can be assumed to be a part of the primary fracture process zone. Hence, this is a crack path along which the specimen would fail if the shear was not applied. As can be observed the failure of the specimen did not occur along the paths within the primary fracture process zone but elsewhere.

In the above-mentioned cases, the reasons for diagonal cracking were firstly low tensile strength and secondly relatively high shear and compressive stresses at the end of the tests. As can be observed on the curves in Figs. 4.5 and 4.6, a sudden stiffening of the specimens has occurred which may suggest that the initial crack is closed or locked. In tests with the older specimens (28 days old) no specimens however, failed due to diagonal cracks. In the case of linear path $\alpha=30°$ and $\alpha=45°$ some diagonal cracks could be observed, but the final failure did not occur in the diagonal direction. Fig. 4.8 displays a case where the specimen did not fail due to diagonal cracks but demonstrates indeed a trace of diagonal cracking. As can be observed the final crack surface is not even and differs much from the crack surfaces which are usually experienced in the pure tensile failure. The reason for comparing this case with the pure tensile case is explained next.

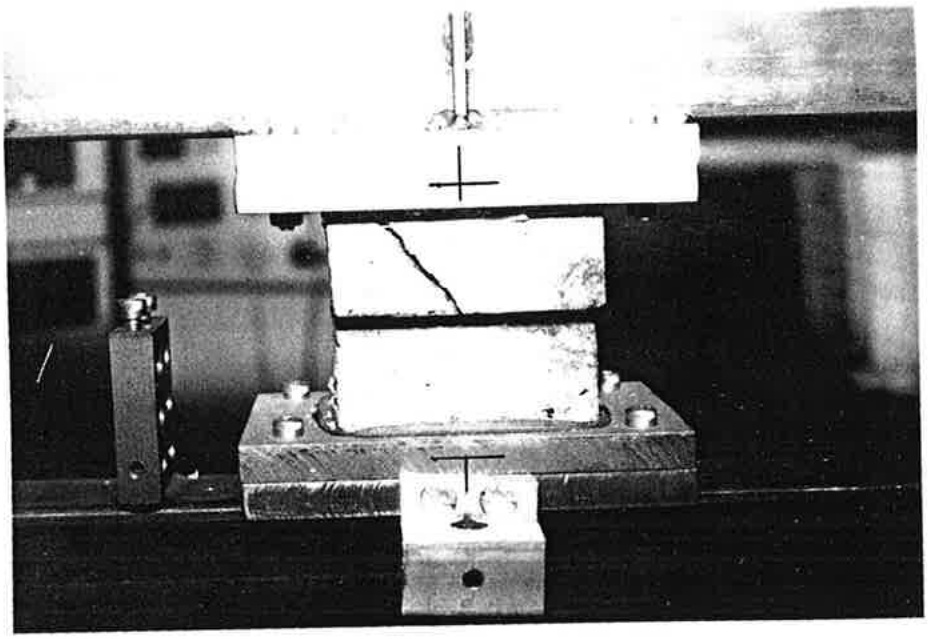

Fig. 4.7a. Failure of a specimen due to diagonal cracking.

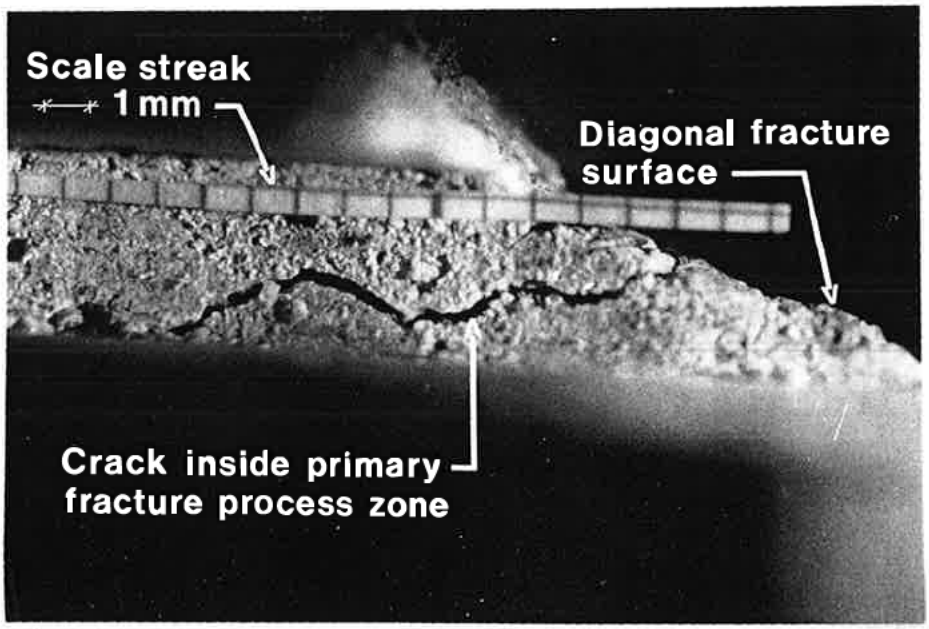

Fig. 4.7b. Close-up of the area inside the notch.

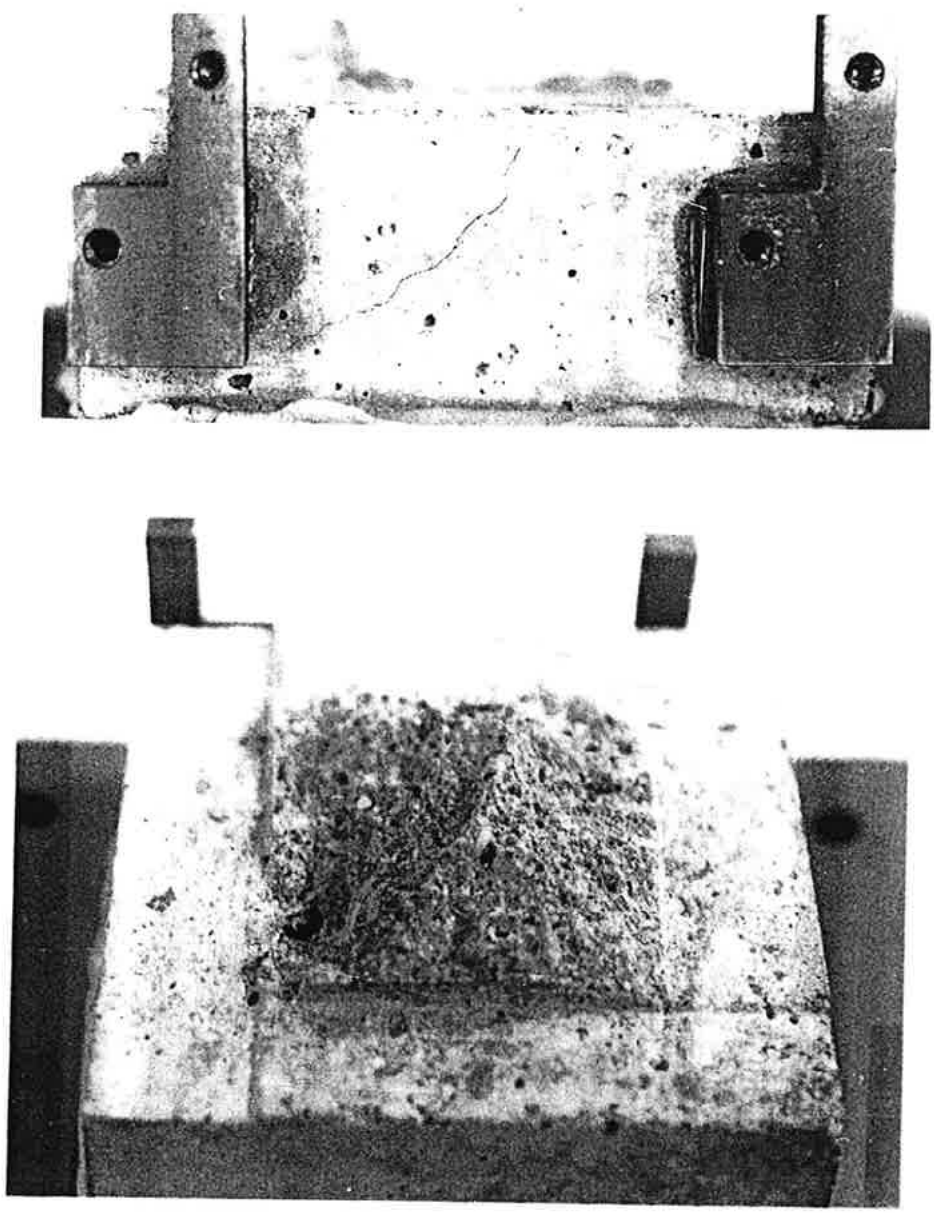

Fig. 4.8. Trace of diagonal cracks and uneven fracture surface.

In this project we are intending to determine the properties of a fracture process zone which is initiated in tensile mode and later becomes subjected to combined normal and shear displacement. Furthermore, we intend to measure properties of one single fracture process zone and not several others which may occur due to improper stress conditions. Hence, in order to determine accurate material properties, the fracture surface should not differ much from the case of pure tensile fracture surface. If such happens, it is an indication of improper stress state within the specimen. The fracture surface displayed in the Fig. 4.8 shows clearly that the crack did not propagate in the same trajectory as the original fracture process zone.

Since no analyses are performed, it is not possible to describe the prevailing stress field inside the specimen.

Fig. 4.9 displays results of a test conducted on wet concrete at the age of 28 days. The displacement path in this case was an inverted parabola with the property that the rate of shear displacement is greater than the rate of the normal displacement in the beginning. The test results show that high shear and compressive stiffness, and high shear and compressive stresses, can be expected inside the primary fracture process zone when the rate of shear displacement is much greater than normal displacement. The visual examination of the specimen showed that although final separation of the specimen did occur within the primary fracture process zone, secondary cracks were indeed apparent, demonstrating the complex stress state inside the specimen. The test result demonstrates the fact that in spite of formation of secondary fracture process zones the damage process also proceeds inside the original zone. In this special case the demolition of the primary fracture process zone had gone so far that when the rate of normal displacement become greater than the rate of the shear displacement, the final separation of the specimen occurred inside the primary fracture process zone. This is, however, in contrast to those cases where the rate of the normal displacement is much lower than the rate of the shear displacement.

Formation of secondary cracks has also been reported by Nooru-Mohamed and van Mier (1989,1991). In their latest work they used a displacement path somewhat similar to the linear path $\alpha=45°$, but with the difference that the displacement path relation was applied from the beginning of the test and not at the maximum tensile stress. They observed crack patterns which are demonstrated in Fig. 4.10. Since in these tests the shear was applied before the maximum tensile stress was reached, no crack can be observed which connects the notch tips. However, their results demonstrate clearly the fact that, in the case of high normal confinement, there is great possibility to create other crack systems than the intended one. It can be observed that in these cases compressive struts are created which can be accounted for by the shear capacity of the specimen.

A very important feature associated with the formation of secondary cracks is their influence on the overall stiffness of the specimen, which may affect the displacement measurements. Erroneous measurements of the displacements leads to incorrect adjustment when following a predetermined displacement path. This may lead to erroneous conclusions concerning the material properties.

On the basis of the above-mentioned observations, it can be concluded that determination of the fracture zone properties requires examination of the crack formation. In these types of tests one is obliged to take cracking pattern into consideration. Otherwise, the determined behaviour is not material properties but properties of the specimen. The primary aim of the present investigation is determination of properties of a fracture process zone which is

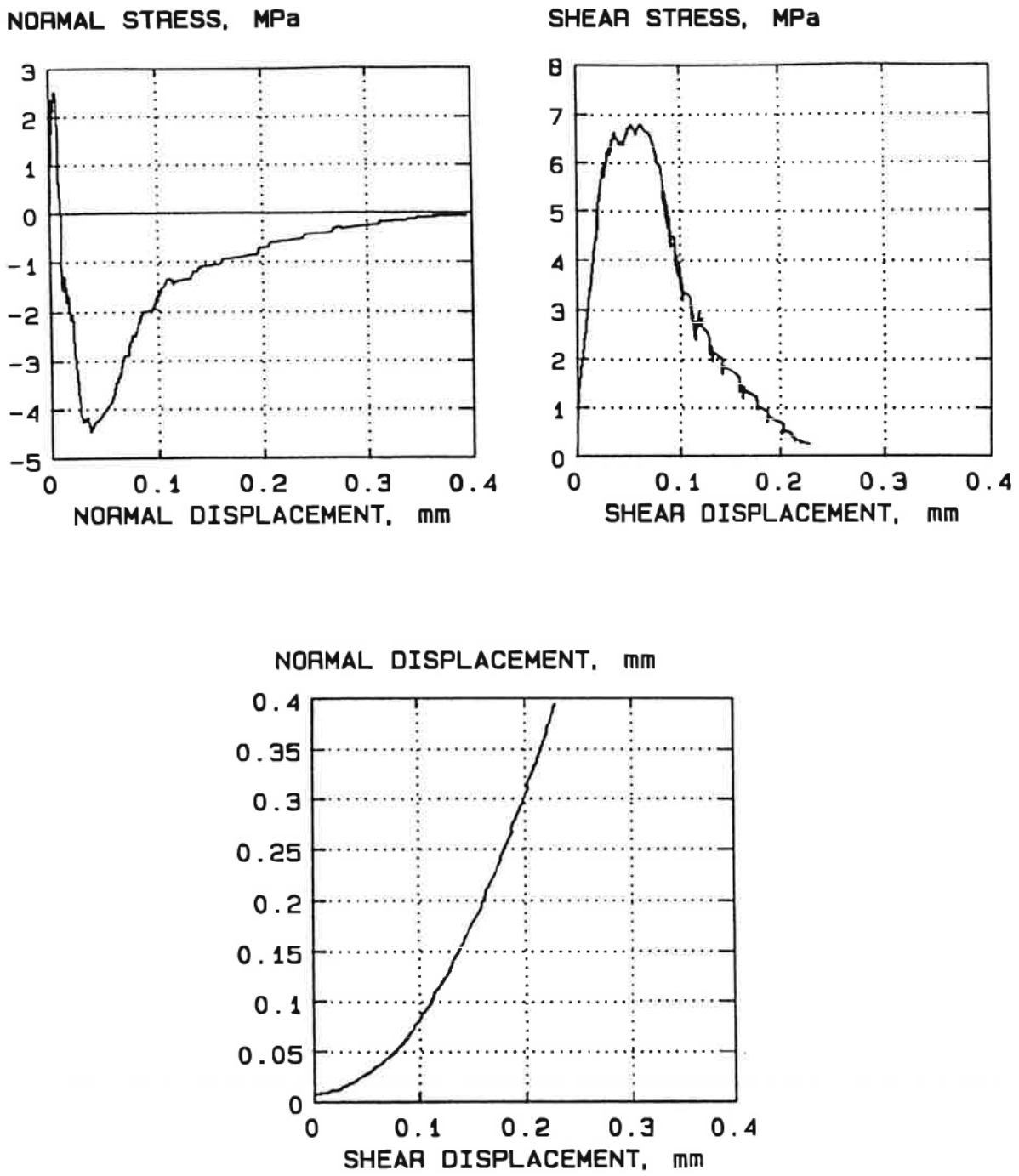

Fig. 4.9. Test with inverted parabolic displacement path ($w=7\delta^2$).

initiated in pure tensile mode and thereafter becomes subjected to combined normal and shear displacements. Sticking to this requirement, one should be assured that there are no crack formations other than the primary one. In this investigation, as much as was possible, viz by means of visual observations and comparison of the fracture surfaces with the fracture surfaces obtained in the pure tensile cases, the specimens which showed secondary cracks

were disregarded from the test series. This action, however, confined the range of the tests. Therefore the tests for the parabolic paths were confined downward to $\beta=0.4$ mm$^{1/2}$, since in the case of $\beta=0.3$ mm$^{1/2}$ traces of secondary cracks could be observed. It should be noted that in the case of the $\beta=0.3$ mm$^{1/2}$, the final crack surface was similar to the pure tensile case. Fig. 4.11 displays the result of the described test. Furthermore, the tests for the linear paths were confined downward to $\alpha=30°$. It should be noted that in the case of $\alpha=30°$ and $\alpha=45°$ secondary cracks sometimes could be observed and sometimes not, and the majority of the fracture surfaces were similar to those which are experienced in the pure tensile tests.

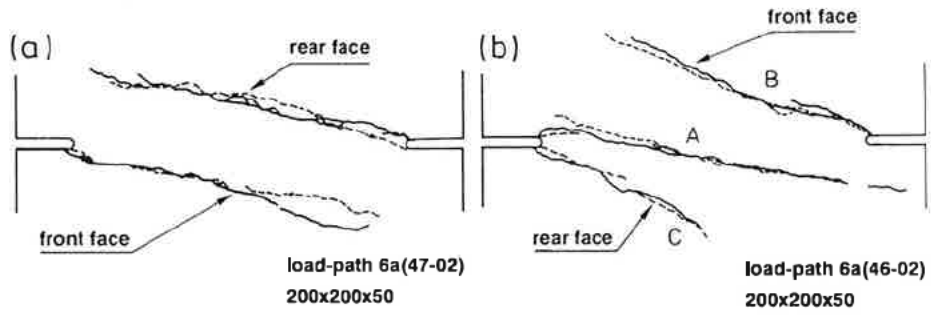

Fig. 4.10. Crack patterns observed in the tests reported by Nooru-Mohamed and van Mier (1991).

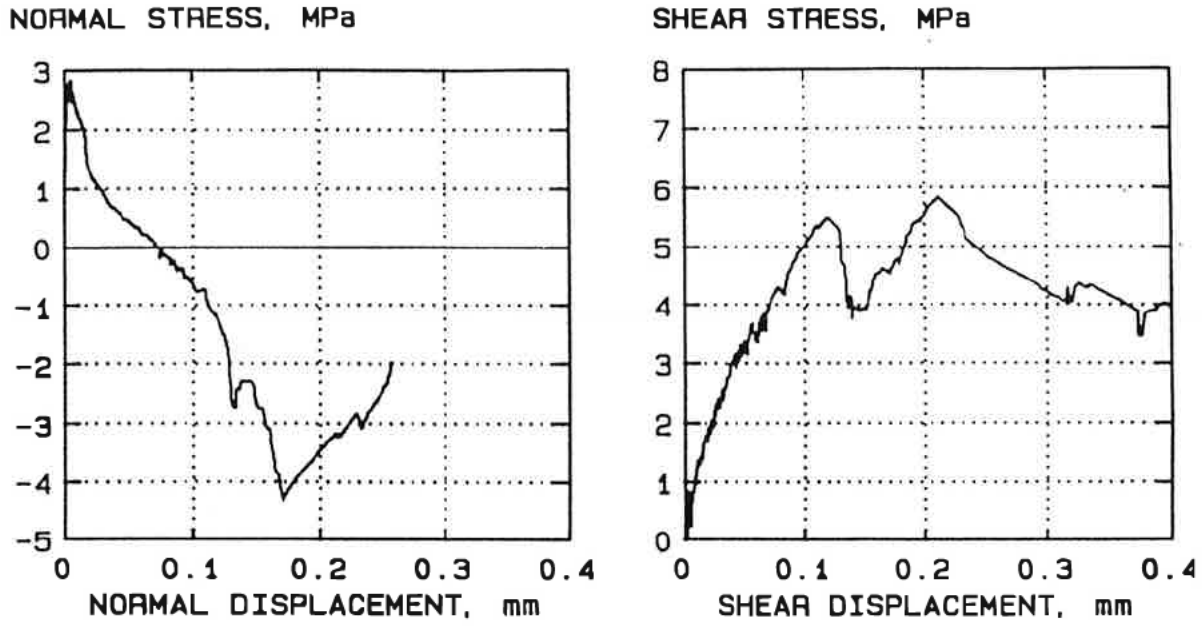

Fig. 4.11. Stress - displacement (σ-γ and τ-δ) curves for test with parabolic displacement path ($\beta=0.3$ mm$^{1/2}$).

4.4 Test results

Fig. 4.12 displays results of the tests on wet concrete specimens at the age of 28 days. The displacement paths were parabolic. The parabola parameters (β) are given in the figure. It should be noted that the normal stress - normal displacement curves are reshaped into the stress - displacement curves of the fracture process zone, viz σ-w curves. The results are mean value of at least three tests. The repeatability of the tests was satisfactory.

Fig. 4.13 displays results of the tests on mortar specimen with the same conditions as above. The curves are results of one single test.

Fig. 4.14 displays results of tests on wet concrete specimens at the age of 28 days. The displacement paths were linear. The line angles (α) are given by the figure. The curves are results of one single test. However, several tests with these paths have been carried out in order to check the repeatability of the tests. The results were not satisfactory for $\alpha \leq 45°$, due to formations of secondary cracks which were discussed in the previous section.

4.5 Discussion of results

Fig. 4.15 displays some of the normal stress - normal displacement curves with higher resolution. In the figure three parts are distinguished, viz part I $0 < w < 0.020$, part II $0.020 < w < 0.080$ and part III $w > 0.080$ (w in mm). The results show that within part I and for $\alpha \geq 60°$, $\beta \geq 0.40$ mm$^{1/2}$ there is no significant difference between the curves. Neither can any significant differences between the pure tensile test and the combined normal and shear tests within the mentioned test limits be observed. Furthermore, the results show that the curves for $\alpha \leq 45°$ differ from the other curves. Let us take a closer look at the displacement paths in Fig. 4.16. Regarding the area $w \leq 0.02$ mm, the figure shows that as far as the parabolic paths are concerned there is no considerable shear displacement. Therefore, it is not surprising that there are no differences either between varying parabolic paths, nor between the parabolic paths and the tensile test. Within the same area, $w \leq 0.02$ mm, shear displacements of the linear paths, $\alpha \geq 60°$, are much greater than the parabolic paths, but there is still no difference between the curves within part I. This may suggest that a minimum shear displacement or minimum path slope, $dw/d\delta$, is required in order to obtain noticeable changes in the slope of the normal stress - normal displacement curves. The results presented here suggest, however, a minimum shear displacement and path slope with the magnitude of approximately 0.020 mm and tan(45°).

Within part II the curves for $\alpha = 60°$ and $\beta = 0.4$ mm$^{1/2}$ start to deviate from the other curves which continue as the tensile curve. Within this part the stress becomes compressive for both displacement paths.

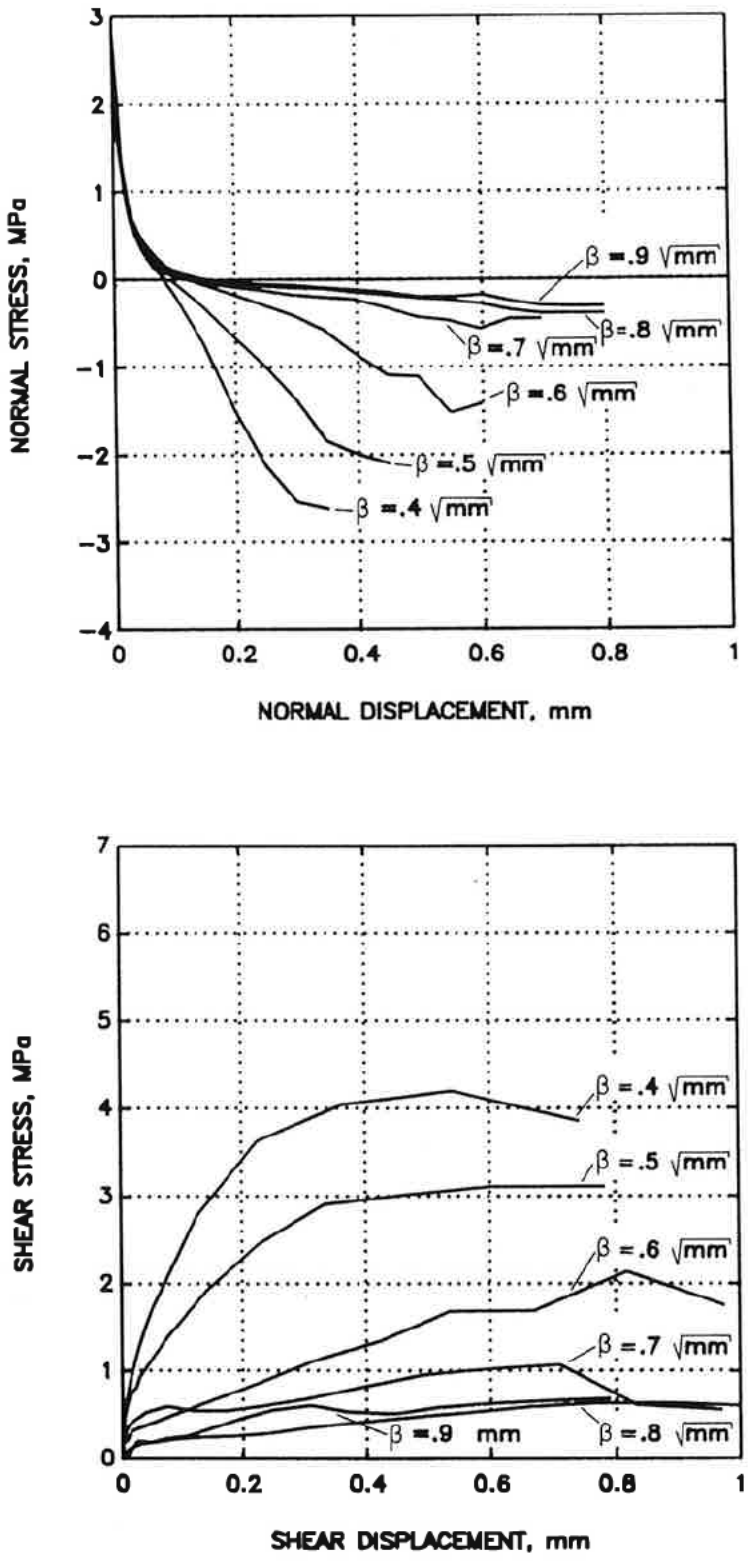

Fig. 4.12. Results of tests (σ-w and τ-δ curves) on wet concrete specimens at the age of 28 days, parabolic paths.

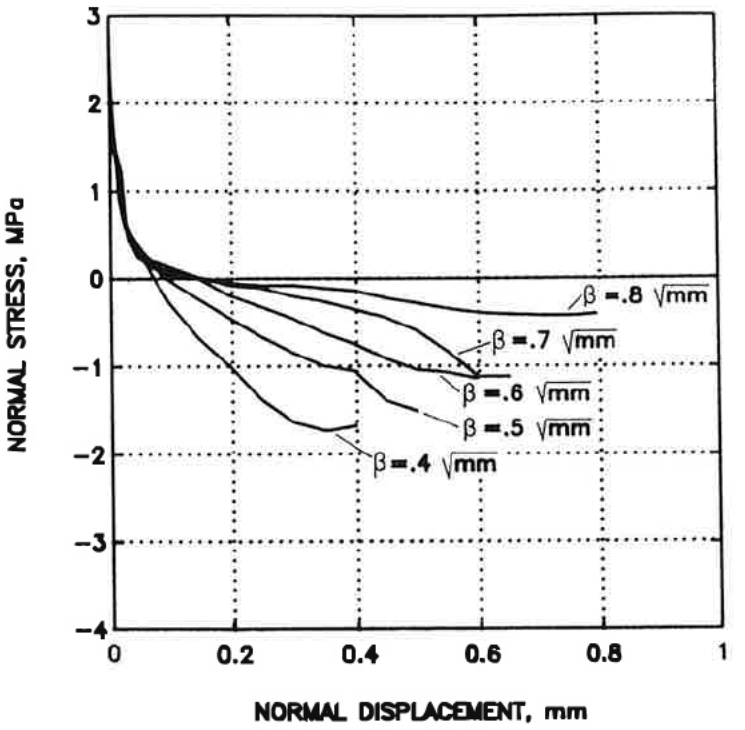

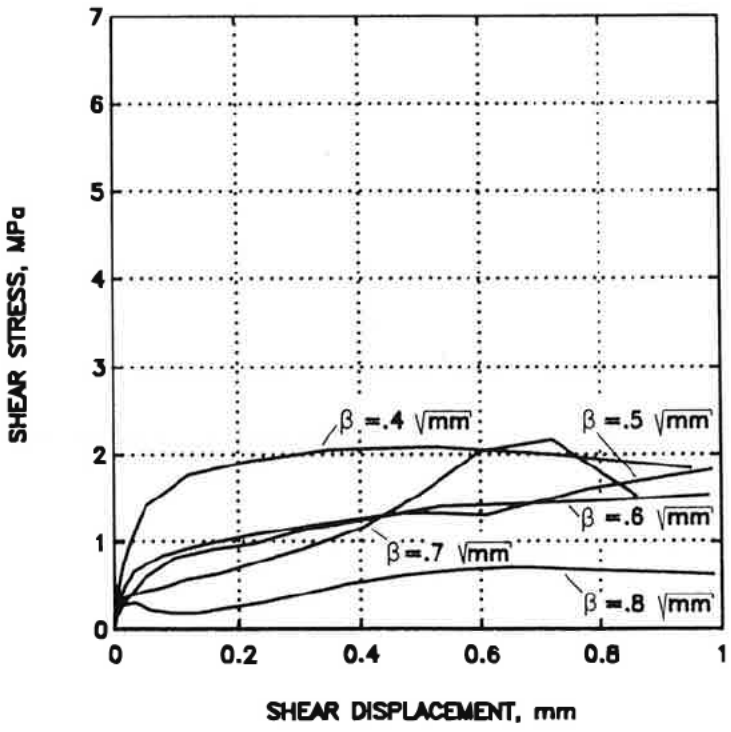

Fig. 4.13. Results of tests (σ-w and τ-δ curves) on wet mortar specimens at the age of 28 days, parabolic paths.

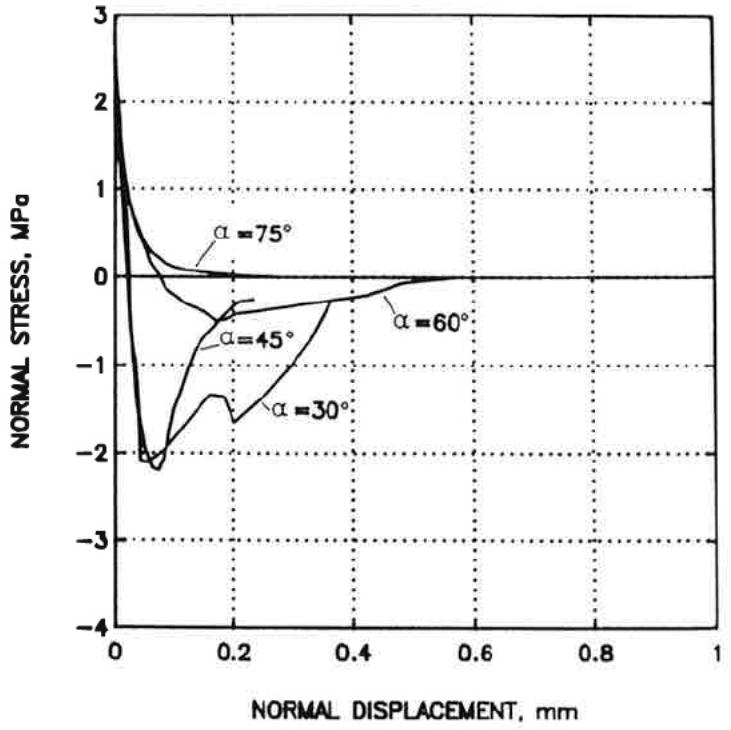

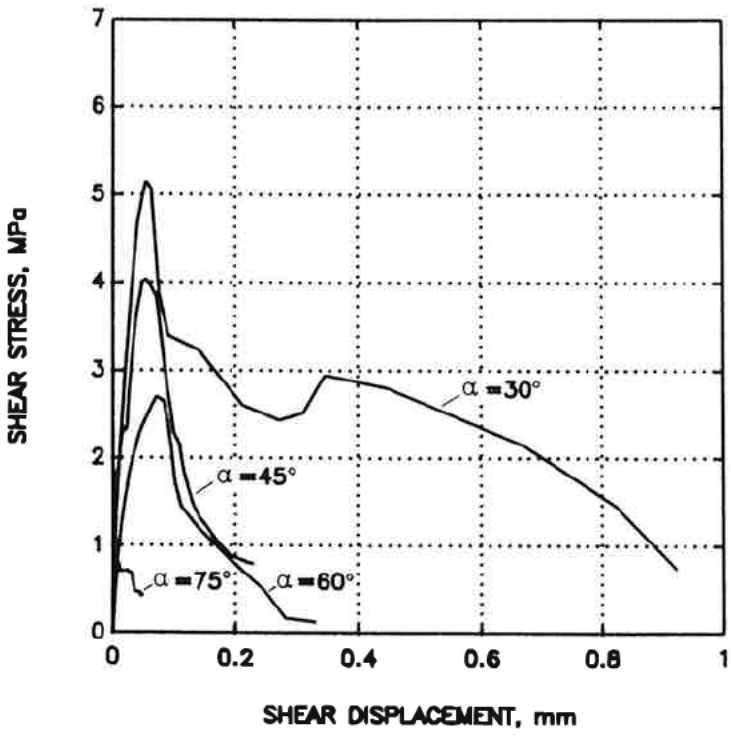

Fig. 4.14. Results of tests (σ-w and τ-δ curves) on wet concrete specimens at the age of 28 days, linear paths.

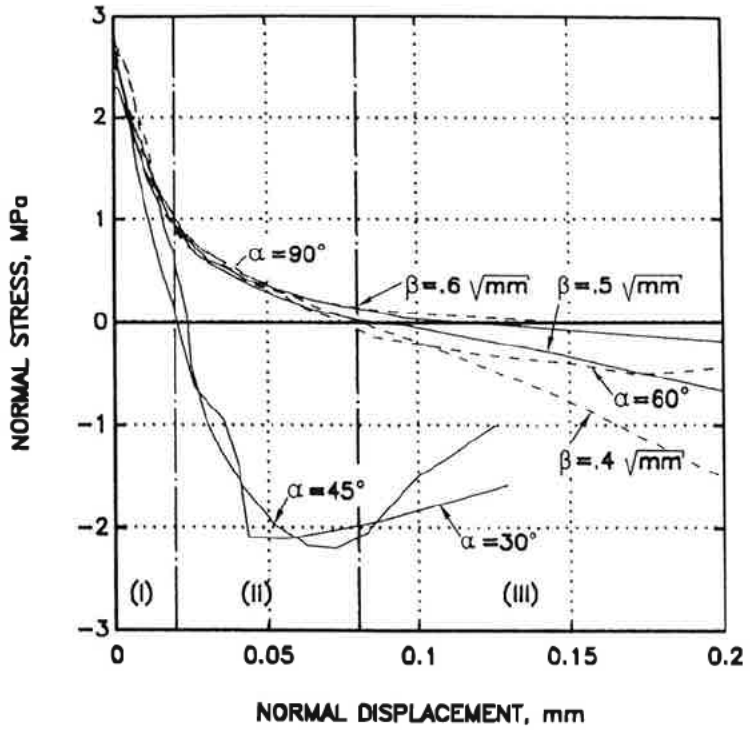

Fig. 4.15. Some of the normal stress - normal displacement curves presented in Figs. 4.12 and 4.14 with higher resolution.

Within part III all the remaining curves start to deviate from the tensile curve and finally intersect the line $\sigma=0$. As far as paths $\alpha\geq75°$ and $\beta\geq0.7$ mm$^{1/2}$ are concerned it is difficult to make any distinction between them and the tensile test until they have intersected the line $\sigma=0$.

Shear stress - shear displacement curves demonstrate that shear stress increases continuously with the increased shear displacement up to a level where in the case of the parabolic paths it bends off to a plateau (Figs. 4.12 and 4.13), while in the case of the linear paths it descends to zero (Fig. 4.14). As far as the parabolic paths are concerned, the results show that the mortar specimens behave in the same manner as the concrete specimens, but at lower stress levels, and that the differences between different parabolic paths are less distinguished. This observation reveals the important role which the size of the aggregates plays in governing the behaviour of concrete under combined axial and shear stress conditions.

The results which are presented here show that when $\alpha\geq75°$ and $\beta\geq0.8$ mm$^{1/2}$, no considerable compressive and shear stresses arise.

The presented results are based on two different sets of displacement paths. The displacements in both directions change continuously during the entire test, which controls the events inside the fracture process zone. As is demonstrated, the response of the specimen

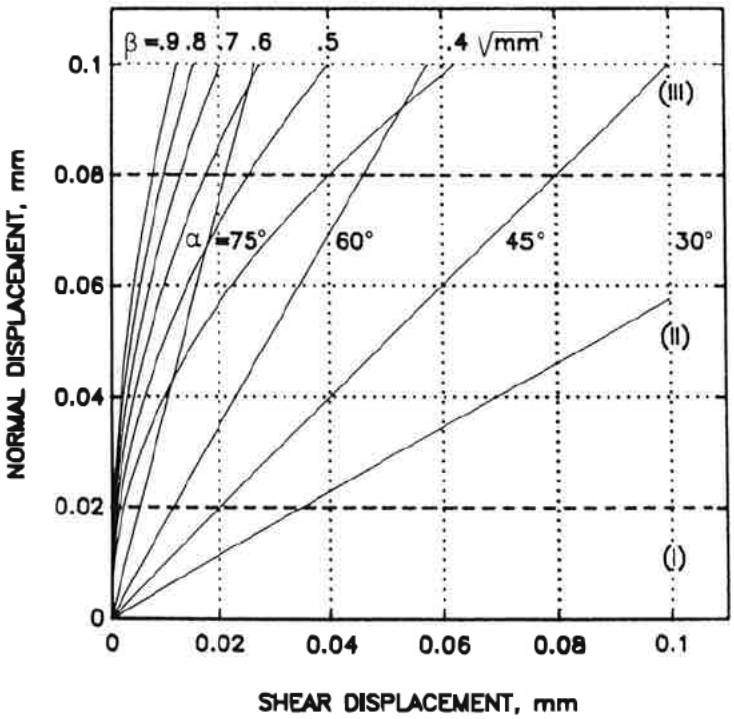

Fig. 4.16. Different displacement paths (Fig 4.1 with higher resolution).

depends upon the displacement paths; compare the linear paths with the parabolic paths. Here, the question is whether the stresses corresponding to the same point on the $w\delta$-plane which has been approached through different paths are the same or not. If the stresses are not the same, then the behaviour of the fracture process zone is path dependent. Some complementary tests have been conducted in order to illuminate the mentioned issue.

4.6 Path dependent behaviour

A "mixed-path" was composed in order to check the path dependency of the combined normal and shear tests. Fig. 4.17a displays the path, solid curve. Part (a) is a straight line with $\alpha=60°$, part (b) is a parabola with $\beta=0.4$ mm$^{1/2}$, part (c) is a straight line with slope 76° and part (d) is a parabola with $\beta=0.6$ mm$^{1/2}$. The tests are carried out on both dry and wet concrete specimens. The results are displayed in Figs. 4.17b and 4.17c. The figures also display the results of the linear and parabolic paths corresponding to $\alpha=60°$, $\beta=0.4$ mm$^{1/2}$ and $\beta=0.6$ mm$^{1/2}$.

It is interesting to compare the shape of the curves. It can be observed that shear stress - shear displacement curves pertaining to the parabolic paths increase continuously, within the displayed range, while the same curves for the linear and mixed paths show a clear maximum. The same trends can be observed in the normal stress - normal displacement

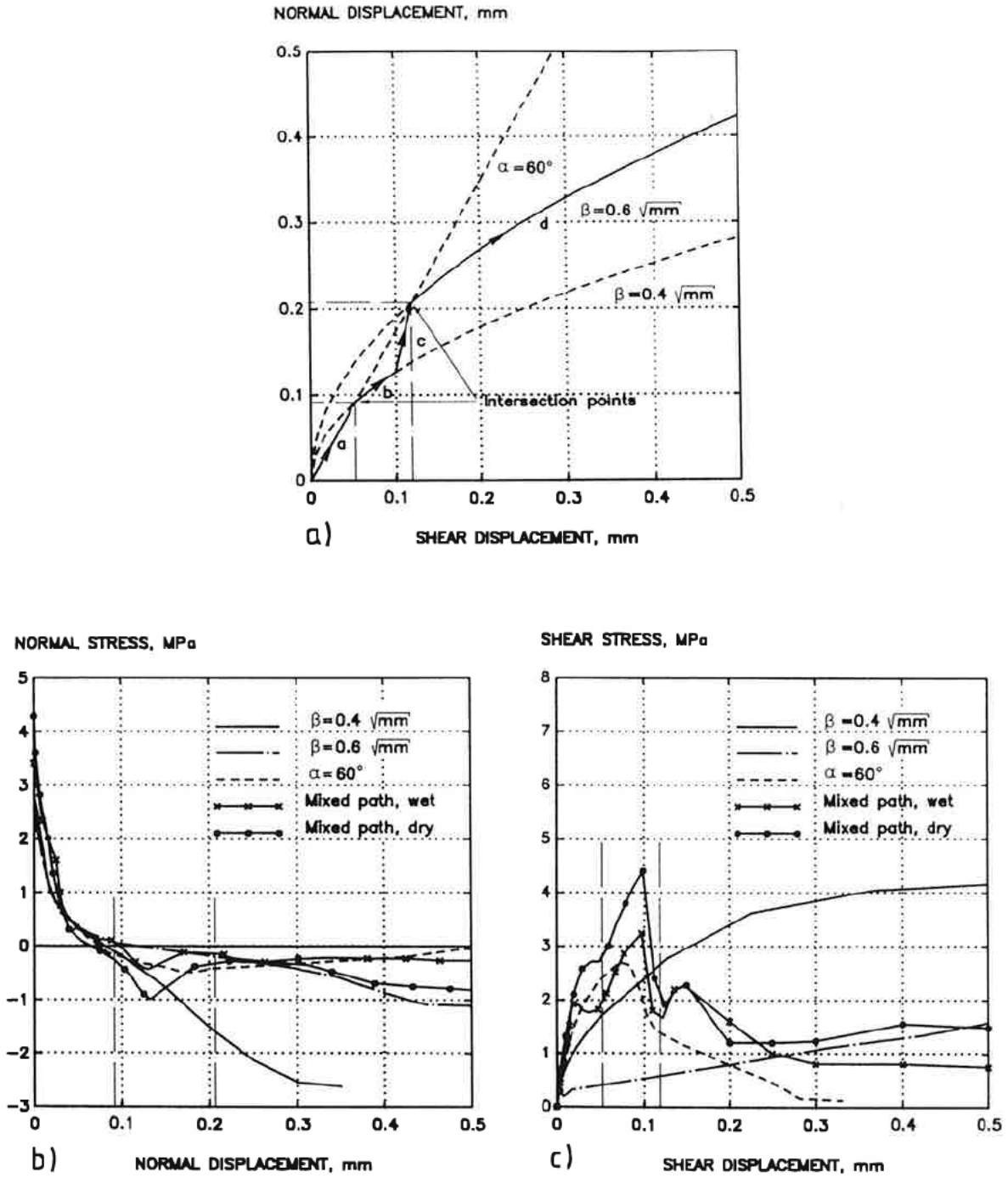

Fig. 4.17. Check of the path-dependent behaviour.

curves but in the opposite direction, i.e. there is a minimum normal stress. Furthermore, it can be observed that the ultimate compressive stresses developed in the case of linear and mixed path are very low.

It is also interesting to compare the curves at the intersection points which are indicated in Fig. 4.17a. If the behaviour of concrete is not path dependant, stresses at the intersection

points, despite different displacement paths, should be identical. At the first intersection point, the point where the linear path $\alpha=60°$ intersects with the parabolic path $\beta=0.4$ mm$^{1/2}$, the normal stresses are not much different, while the shear stresses differ somewhat. At the second intersection point, the point where the linear path $\alpha=60°$ intersects with the parabolic path $\beta=0.6$ mm$^{1/2}$, as far as normal stresses are concerned the same conclusion as before appears, while a great difference between the shear stresses is observed; compare parabolic path $\beta=0.6$ mm$^{1/2}$ with the linear and mixed path.

Another interesting observation in this context is revealed by comparing the continuation of the mixed path and the parabolic path $\beta=0.6$ mm$^{1/2}$. It can be observed that, despite identical displacement paths during the succession of the test, the curves corresponding to the tests behave entirely differently.

4.7 Cracking process within the fracture process zone

Compared to the pure tensile case, cracking of concrete due to combined normal and shear stresses is less understood. To date there is no consistent hypothesis which describes the cracking of concrete under combined stress conditions, from the instant of formation of the tensile fracture process zone to the instant of separation. Hillerborg (1989b) divides the failure process into two stages. According to Hillerborg, in the early stages, when shear stress is imposed, the small tensile micro-cracks bend off and grow in a skew direction. This gives rise to formation of compression struts which perform rotating movements causing compressive and shear stresses while the normal and shear displacement increases, Fig. 4.18. In the later stage when the real crack is formed, due to the irregular shape of the fracture surface, occurrence of the shear displacement gives rise to compressive and shear stresses, Fig. 4.19. The latter description of Hillerborg is consistent with theories of aggregate interlock. According to Hillerborg, in the intermediate stages both phenomena may occur simultaneously.

The above-mentioned mechanisms are difficult to prove experimentally. Since the structure of concrete is very complex, it is also difficult to relate them to the observed macro-mechanical behaviour. However, as far as this investigation is concerned it is possible to explain some of the observed phenomena by means of the aggregate interlock theories. Here one of the models will be presented in order to further discuss the test results. The model which will be briefly presented is developed by Walraven (1979,1980). Here only the assumptions of the model will be described and some results will be shown. The reader is referred to the references for further details.

According to the Walraven model the normal stress (σ) and shear stress (τ), caused by aggregate interlock can be calculated by the following equations.

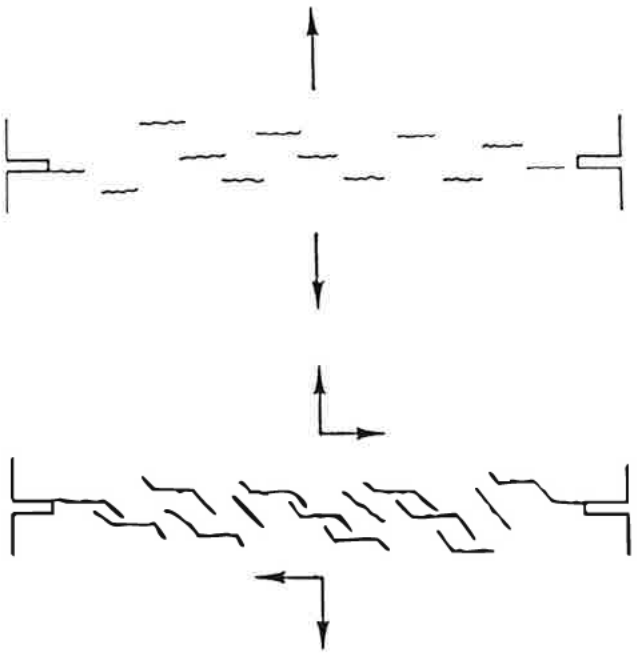

Fig. 4.18. Development of micro-cracks in combined stress conditions, taken from Hillerborg (1989b).

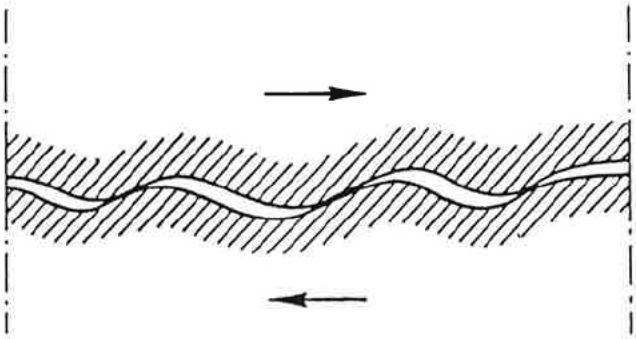

Fig. 4.19. Influences of the irregularities in a crack with a shear displacement, taken from Hillerborg (1989b).

$$\sigma = \sigma_{pu}(A_x - \mu A_y)$$
$$\tau = \sigma_{pu}(A_y + \mu A_x) \qquad 4.2$$

in which σ_{pu} is the matrix yielding stress and μ is coefficient of friction, approximately 0.4. A is the total contact surface between two sides of the specimen per unit surface of the fracture plane. The indices x and y denote the projection of the A on the xz-plane and yz-plane. Derivation of the equations for A has been based on the following assumptions:

The aggregates are infinitely rigid and strong, spherical particles which are embedded in a rigid-plastic matrix of cement paste. The aggregate size distribution is determined by means of the Fuller model.

It is assumed that prior to the imposition of the displacements, a crack with zero width exists and both normal and shear stresses are zero. Furthermore, it is assumed that the crack follows the boundary of the aggregates.

Path dependant behaviour has been neglected, i.e. the same displacements give the same contact surfaces regardless of the displacement path.

Fig. 4.20 displays schematically contacts between an aggregate particle and the matrix. Fig. 4.20a displays the situation before imposing the displacements, while Fig. 4.20b displays the situation after imposing the displacements. w and δ are the translations of the upper part relative to the lower part of the body, which is here assumed to be equivalent to the normal and shear displacements. a_x and a_y are the projections of the contact surface between the matrix and an aggregate particle on the xz-plane and yz-plane. A_x and A_y are calculated by summation of a_x and a_y over the unit fracture surface. The equations for A_x and A_y are given in Appendix B, for which numerical integration is required. Below, results of the analysis performed by this model are presented. In the analysis it has been assumed that 75 percent of volume of concrete is occupied by aggregates with 8 mm maximum fraction.

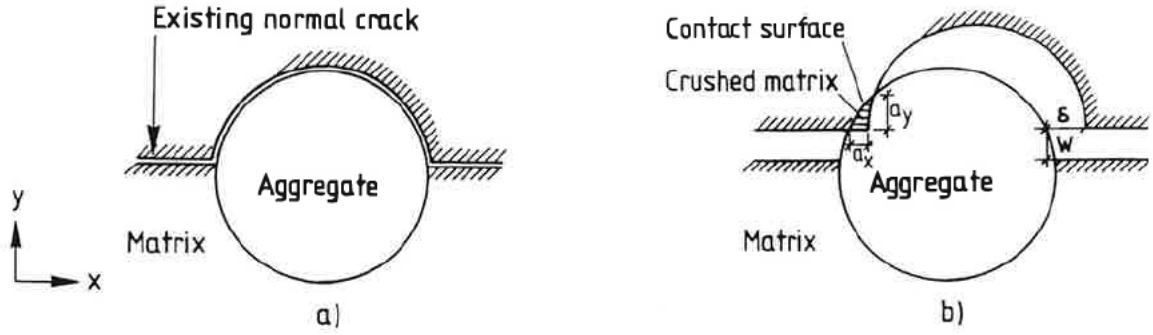

Fig. 4.20. Schematic description of contact surface between an aggregate particle and the matrix, according to Walraven (1980).

Fig. 4.21 displays development of the contact surfaces A_x and A_y as functions of shear displacement for different displacement paths. In the case of the linear paths, the theoretical results demonstrate that the contact surfaces A_x and A_y are large in the beginning but decrease as a result of the imposed displacements, and the higher α is the smaller will be the contact surfaces within the fracture zone. Furthermore, in the case of $\alpha=75°$, the contact

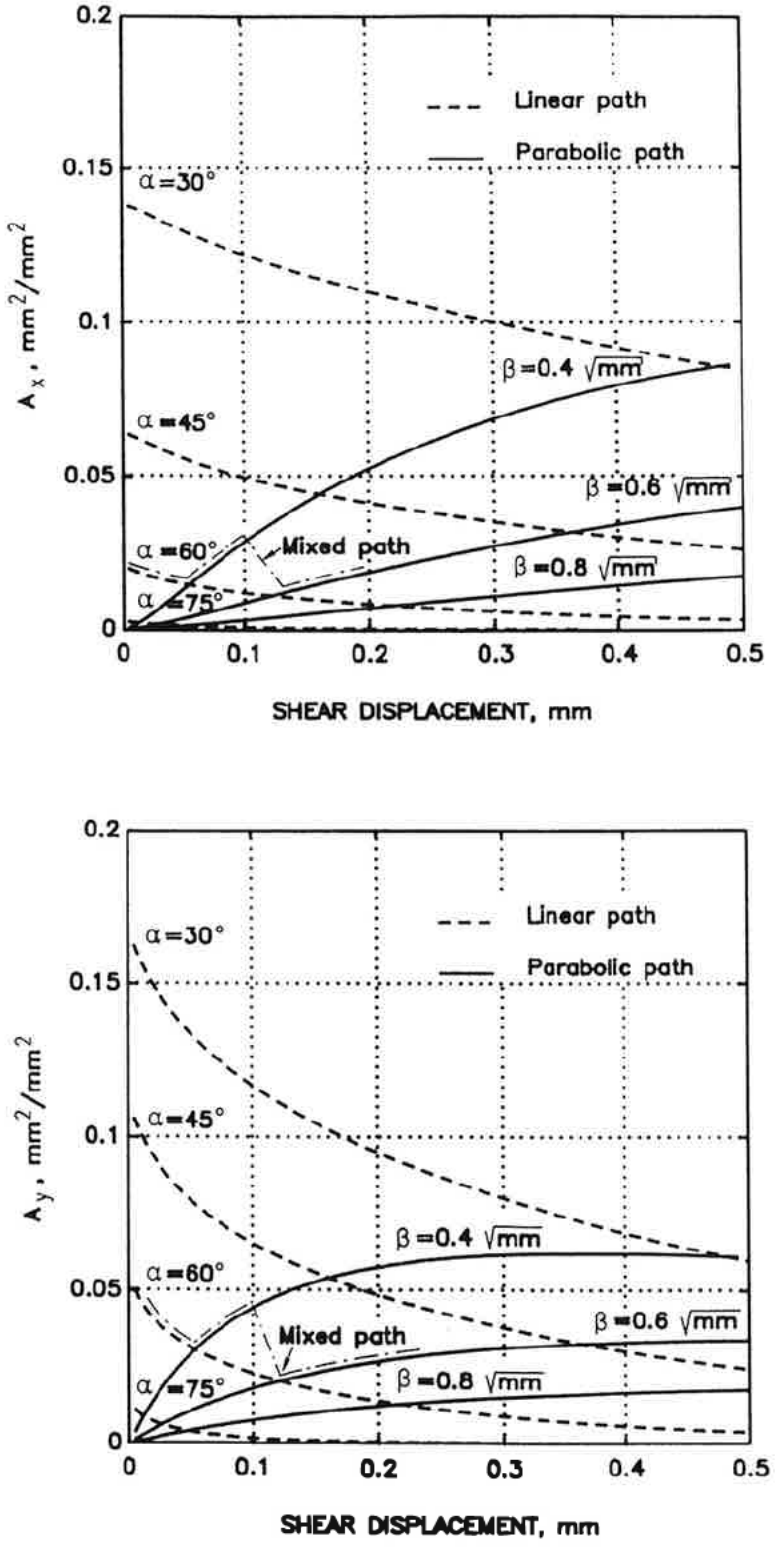

Fig. 4.21. Development of the contact surfaces A_x and A_y as functions of shear displacement.

surfaces are too small to cause any stresses of significant magnitude, while in the other cases of linear paths the larger contact surfaces lead to higher stresses. This can be observed in the test results displayed in Fig. 4.14, which show that the developed stresses in the case of $\alpha=75°$ are much lower than in the other cases.

In the case of the parabolic paths, the theoretical results demonstrate that the contact surfaces A_x and A_y are very low in the beginning, but increase successively and finally end up to a plateau as the shear displacement increases. The theoretical results also reveal the sudden changes of the shear response of the specimen when β is decreased from 0.4 to 0.6 $mm^{1/2}$, compare Fig. 4.12.

Comparison between linear and parabolic paths explains to some extent the different behaviour observed in the tests. In the experiments, the linear paths showed maximum shear stress while the parabolic path, within the test range, did not show any maximum stress. This difference can be explained by means of the different developments of the contact surfaces which are demonstrated theoretically.

The development of the contact surface is important for path depended behaviour of the fracture process zone. Greater contact surface may lead to greater damage and crushing of the material inside the fracture process zone. In Fig. 4.21 development of the contact surface for the mixed path is also given. As was mentioned, the stress - displacement curves of the last part of the mixed path (parabola $\beta=0.6$ $mm^{1/2}$) did not coincide with the pure parabolic path $\beta=0.6$ $mm^{1/2}$. As is demonstrated by the theoretical curves, prior to the intersection of the two paths, the developments of the contact surfaces in these two cases are much different. The larger contact surface in combination with higher stresses in the beginning of the mixed path may have caused crushing of the material or may have forced a new fracture process zone in the vicinity of the primary fracture process zone.

Fig. 4.22 displays the theoretical development of the stresses as functions of the displacements. Shear stress - shear displacement curves are displayed by solid curves, while normal stress - normal displacement curves are displayed by dashed curves. The stresses are dimensionless, viz stresses in equation 4.2 have been divided by σ_{pu}. As can be observed the shear stress for the linear path $\alpha=60°$ is not zero at zero shear displacement. This is due to the fact that the matrix is regarded as rigid-plastic material. As can be observed the theoretical curves to some extent look like the experimental curves. The shear stress corresponding to the linear path decreases rapidly while the shear stresses corresponding to the parabolic paths increase. Furthermore, the developed compressive stress in the case of the linear path is much lower than in the parabolic paths, which were also observed in the tests. As is demonstrated in the figure, development of the compressive stress is delayed in the case of the parabolic paths, which can be explained by the fact that in the beginning the compressive stresses are counteracted by the tensile stresses caused by the friction, note Fig.

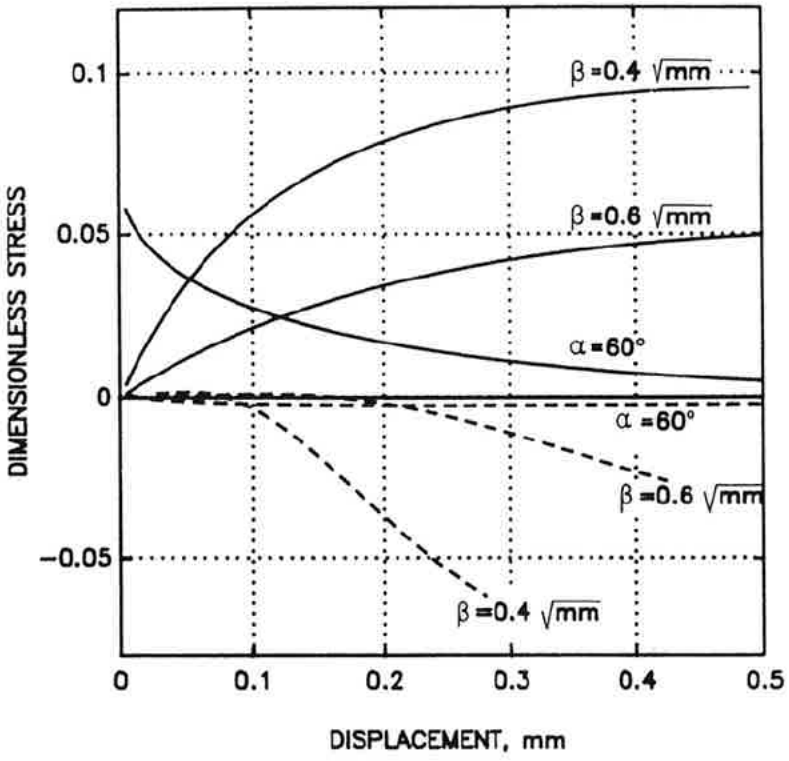

Fig. 4.22. Theoretical development of the stresses σ/σ_{pu} and τ/σ_{pu} as functions of displacements w and δ.

4.21 and equation 4.2. This is also the theoretical reason for the poor development of the compressive stresses in the case of a linear path.

The Walraven model highlights some of the phenomena which were observed in the experiments. However, it should be noted that the model neglects some crucial effects, like existence of the tensile fracture process zone, non-spherical particles, crushing of the aggregates, variation of the coefficient of friction and formation of new contact surfaces as a result of crushing of the former surfaces.

4.8 Empirical expression adopted to the test results

Since the mechanism of cracking as well as path dependent behaviour of concrete are not well understood it has been difficult to derive a micro-mechanical model which describes the observed behaviour. Instead empirical expressions have been developed. The expressions are fitted to the stress - displacement curves which are displayed in Fig. 4.12 (parabolic paths for concrete), see following expressions:

$$\sigma = 2.8\left(e^{-40w} - 2.5e^{-5\beta^3}\arctan\delta\right)$$

$$\tau = 10e^{-3.6\beta^{1.4}}\left(\arctan\frac{\delta}{\beta^2}\right)^{0.5} \qquad 4.3$$

with

$$\beta = \frac{w}{\sqrt{\delta}}$$

The expressions are valid for the domain on the δw-plane which is confined by the parabola $w \geq 0.40\delta^{1/2}$, $w \geq 0$ and $\delta \leq 0.8$ mm. In the following parts the term "test domain" refers to the described domain. The expressions are not based on any material model, but are chosen entirely arbitrarily. The expressions predict the results of the parabolic paths fairly well. However, it should be noted that the best prediction is achieved for $\beta = 0.4$ mm$^{1/2}$, while prediction of the results of the parabolic path $\beta = 0.6$ mm$^{1/2}$ is not as good as for the other ones. The predicted and experimental curves of the mentioned paths ($\beta = 0.4$ and 0.6 mm$^{1/2}$) are compared in Fig. 4.23.

As mentioned above, the expressions in 4.3 are fitted to the parabolic paths and are valid for the test domain described previously. In 4.24 the stress - displacement curves of the linear path $\alpha = 60°$ predicted by the expressions in 4.3 are compared with the stress - displacement curves of the linear path obtained by experiment. It should be noted that the linear path ($\alpha = 60°$) intersects with the parabola $\beta = 0.4$ mm$^{1/2}$ (the lower limit of the test domain) at the point $\delta = 0.053$ mm, $w = 0.092$ mm, i.e. the points on the linear path $\alpha = 60°$ with $\delta \leq 0.053$ mm and $w \leq 0.92$ mm are located outside the test domain. The point is indicated on the figure. The predicted curves are outcomes of the fitting of the arbitrary expressions to the results of the parabolic paths. Consequently, the predicted stresses correspond to the displacements which are intersection points between the line $w = (\tan 60°)\delta$ and parabolas with varying β. Fig. 4.25a displays intersection between the line and several parabolas. The figure also partly displays the domain where the expressions in 4.3 are applicable. Fig. 4.25b displays the rate of the shear displacement ($d\delta/dw$) as a function of the normal displacement (w) and the displacement paths, up to the intersection points between the linear and parabolic paths.

In the case of the σ-w curves Fig. 4.24 shows that there is good agreement between the predicted curve and the test result. In the case of the τ-δ curves the agreement is not as good as for the previous case, especially outside the test domain. The reason for disagreement between the predicted and experimental τ-δ curves inside the test domain is due to differences in the displacement paths, which was discussed previously. Another important

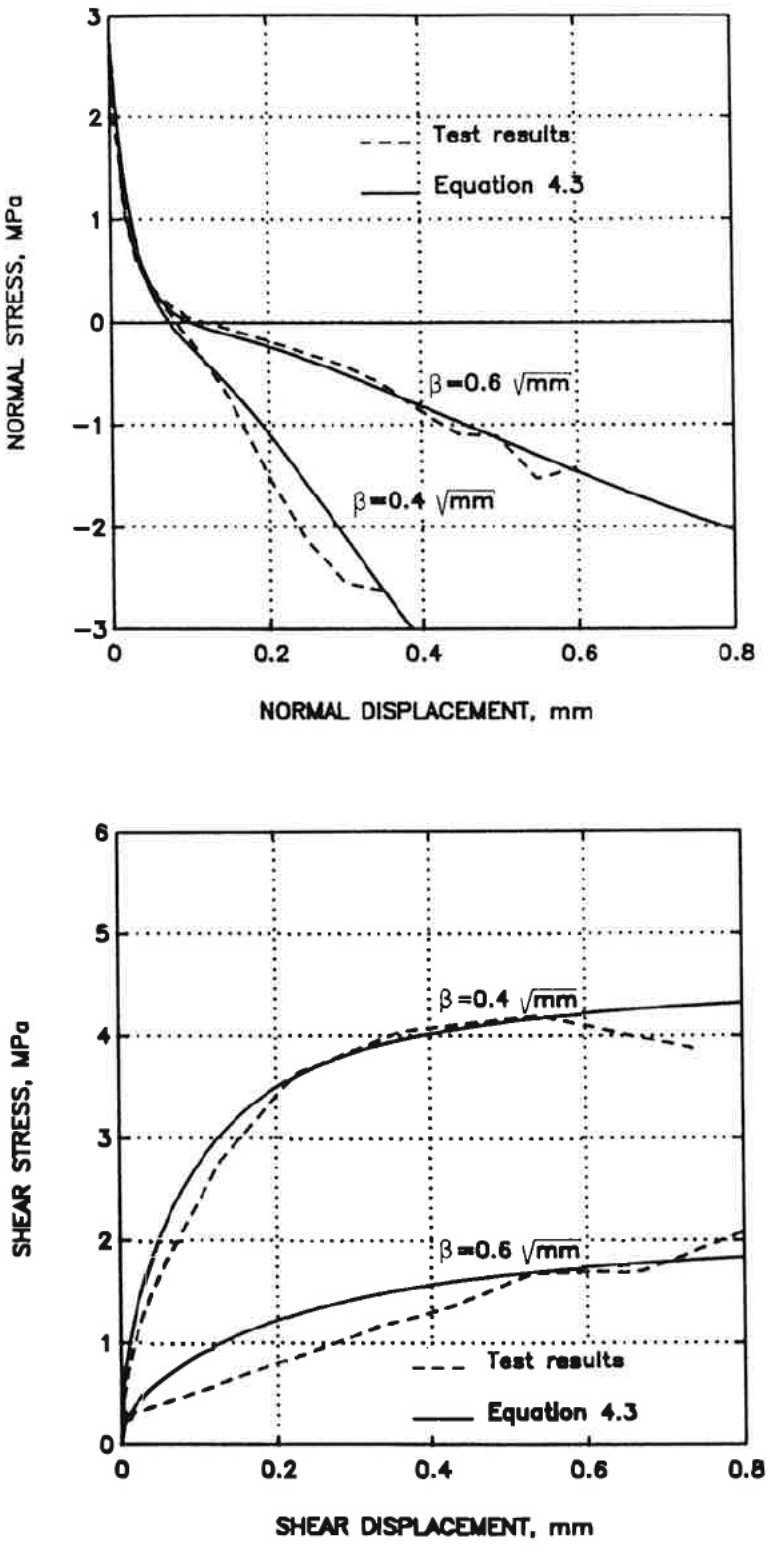

Fig. 4.23. Comparison between empirical expressions and test results.

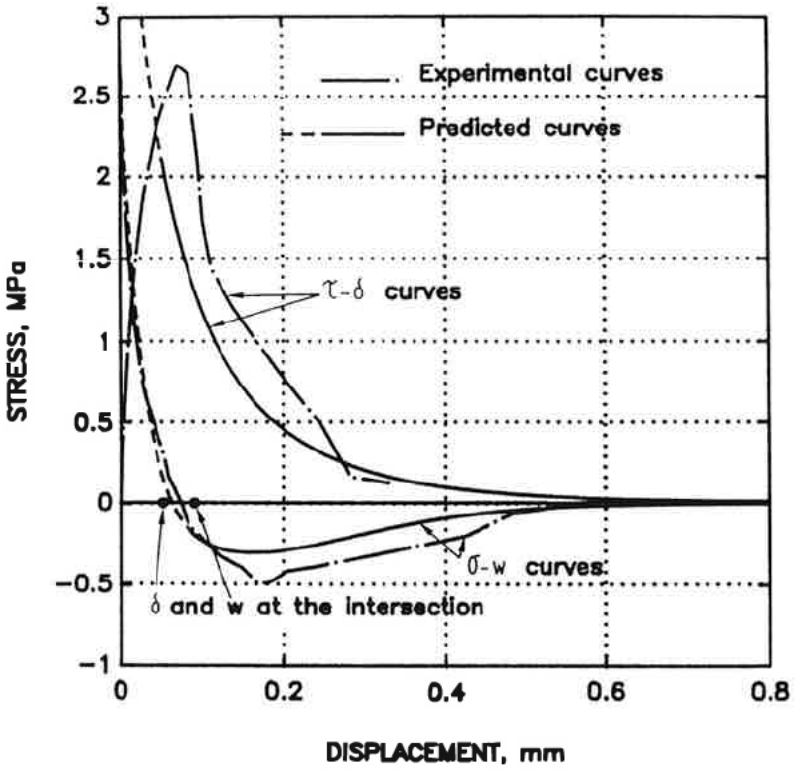

Fig. 4.24. Comparison between predicted and experimentally obtained stress - displacement curves (linear path $\alpha=60°$).

subject is the variation of the rate of shear displacement. As can be observed in Fig. 4.25b the rate of shear displacement is constant in the case of the linear path while it increases linearly in the case of the parabolic paths. If a path with a successively increasing shear displacement rate from zero to a constant level was tested instead of the mentioned linear path, for instance the dashed curve in Fig. 4.25b, better agreement would be obtained between the experiment and the expressions in 4.3.

Disagreement between the experimental and the predicted τ-δ curves outside the test domain is explained by the fact that the expressions in 4.3 are developed without any attention to the test results outside the domain.

The aim of this investigation has been determination of the elements of the stiffness matrix of the fracture process zone, i.e C_{11}, C_{12}, C_{21} and C_{22} in equation 2.11, which are defined as follows:

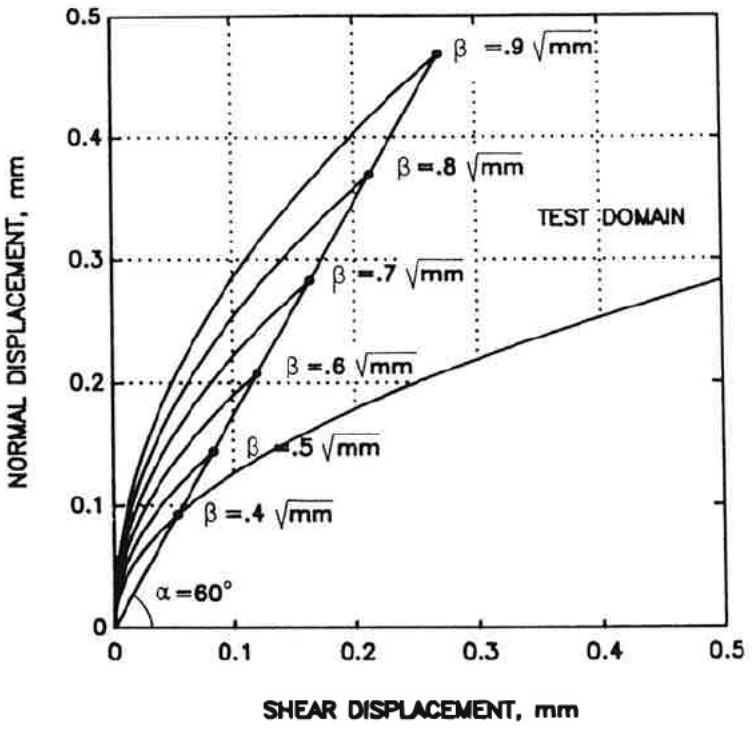

Fig. 4.25a. Intersection points between the linear path (α=60°) and parabolic paths.

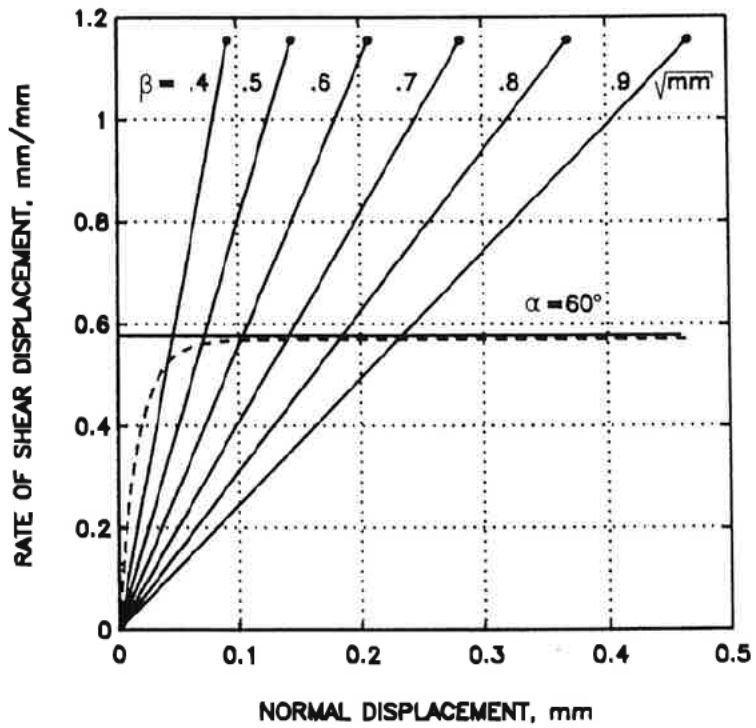

Fig. 4.25b. Rate of shear displacement as function of w and β.

$$C_{11} = \frac{\partial \sigma}{\partial w} \qquad C_{12} = \frac{\partial \sigma}{\partial \delta}$$

$$C_{21} = \frac{\partial \tau}{\partial w} \qquad C_{22} = \frac{\partial \tau}{\partial \delta} \qquad 4.4$$

As previously described, the tests are conducted with a constant parabolic displacement path which is the basic assumption as far as the expressions in 4.3 are concerned. Therefore, the correct stiffness elements can only be obtained by differentiation of the equations in 4.3 with the condition of constant β throughout the fracture process. However, with the conditions which were discussed previously, viz non-constant shear displacement rate during the initiation of the fracture process zone and displacement paths within the limits of the test domain, the expressions in 4.3 can be used for determination of C_{11}, ... and C_{22} with acceptable accuracy. The differentiation of the expressions in 4.3 is given in Appendix C.

4.9 Comparison of the results with other tests

In this section the results of the parabolic paths will be compared with the results reported by the other investigators, see Chapter 3. It was mentioned that the test paths used by them differ from the paths used in this investigation. The intention of this section is to further demonstrate the complex and path dependent behaviour of concrete under combined normal and shear stress conditions.

In order to facilitate the reshaping of the curves, only the empirical expressions are used. Furthermore, since some of the results do not contain any expressions for the normal stresses, only the shear stress - shear displacement expressions are compared.

Below, one additional empirical expression, besides those which are given in Chapter 3, will be introduced. The expression is given by Bazant (1980), and is based on the tests reported by Paulay and Loeber. The expression is shown below:

$$\sigma = -\frac{a_1}{w}(a_2 |\tau|)^p$$

$$\tau = \tau_u r \frac{a_3 + a_4 |r|^3}{1 + a_4 r^4} \qquad 4.5$$

with

$$r = \frac{\delta}{w} \; ; \qquad \tau_u = \tau_0 \frac{a_0}{a_0 + w^2}$$

$$p = 1.3\left(1 - \frac{0.231}{1 + 0.185w + 5.63w^2}\right)$$

$$\tau_0 = 0.245 f_{cc} \; N/mm^2 \; ; \quad a_0 = 0.01 D_a^{\,2} \; mm^2$$

$$a_1 = 0.000534 \; N/mm \; ; \quad a_2 = 145 \; mm^2/N$$

$$a_3 = \frac{2.45}{\tau_0} \; N/mm^2 \; ; \quad a_4 = 2.44\left(1 - \frac{4}{\tau_0}\right) N/mm^2$$

Figs. 4.26a and 4.26b display the comparison of the different empirical expressions for the parabolic paths β=0.4 mm$^{1/2}$ and β=0.6 mm$^{1/2}$. The figures reveal that the stresses obtained in this investigation are lower than those in the other investigations. Besides the general differences such as concrete quality, concrete composition and aggregate size, the differences in the test paths have caused the observed discrepancy.

In the tests reported by Fenwick et.al. and Houde et.al. the specimens were sheared under constant normal displacement. The results presented in this investigation show that high shear displacement rates (dδ/dw) cause stiffer shear behaviour and lead to higher final stresses. Hence, it is not surprising that the shear stresses in the present investigation are lower than the shear stresses reported by Fenwick et.al. and Houde et.al.

The difference between the results of Walraven and of the present investigation is explained by the fact that in Walraven's tests shear was initiated when the normal stresses were zero or compressive. Furthermore, the rate of the shear displacement (dδ/dw) after initiation was higher than the rates reported here.

The above-mentioned comparisons demonstrate again the influence of the test paths on the behaviour of the material. Furthermore, the investigation show that cases with simultaneously increasing normal and shear displacements lead to lower final shear stresses, compared to cases when the displacements are increased one at a time to the same point on the δw-plane; note Fig. 4.26.

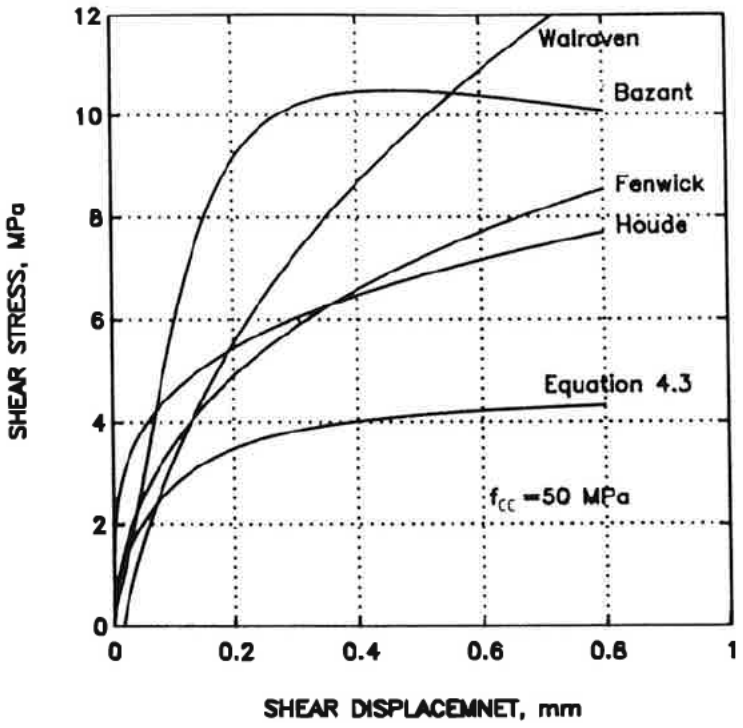

Fig. 4.26a. Shear stress - shear displacement curves according to the different empirical expressions for parabolic path $\beta=0.4\ mm^{1/2}$.

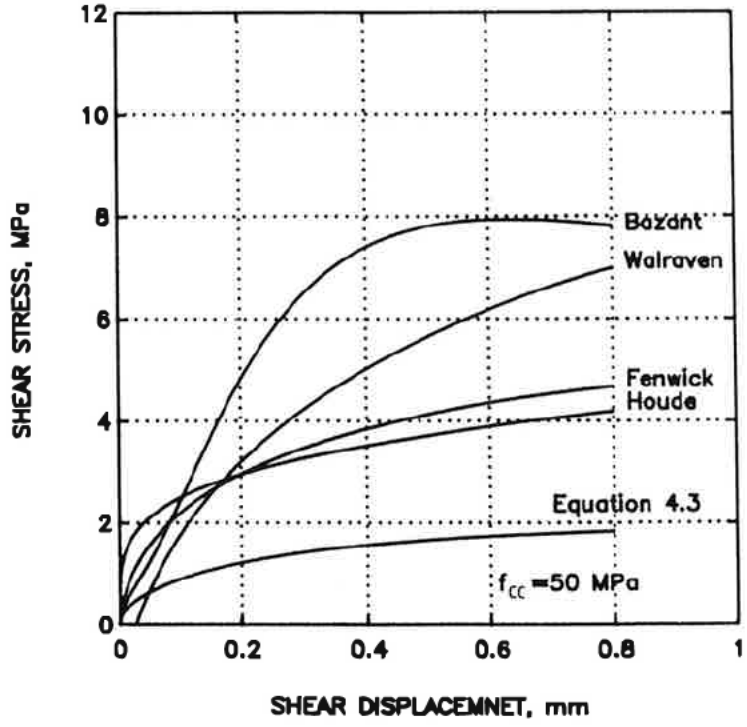

Fig. 4.26b. Shear stress - shear displacement curves according to the different empirical expressions for parabolic path $\beta=0.6\ mm^{1/2}$.

5 Conclusions and future work

5.1 Conclusions

Within the framework of the present investigation an equipment for determination of the softening properties of the concrete was developed. The properties of interest are the relations between the stresses and displacements inside the fracture process zone. On the basis of the test results presented in Chapters 3 and 4 it can be concluded that:

Test arrangements similar to the equipment developed within this project are suitable for determination of tensile properties of concrete, provided that the stiffness of the components of the equipment are sufficiently high. Furthermore, the design expressions developed for the equipment reveal the factors influencing the performance of the equipment, which facilitates the design of new arrangements with improved properties.

It has been demonstrated that it is possible to expose the fracture process zone to simultaneously varying normal and shear displacement without any uncontrollable events.

It has been demonstrated that the stress-displacement response of the fracture process zone is highly influenced by the displacement path. It has been shown that to approach a point on the δw-plane by two different paths leads to different stresses and different shapes of the stress-displacement curves.

The test method for the combined normal and shear test developed in this project is suitable for determination of the properties of the fracture process zone. However, the applicability of the test method is restricted within a certain area on the δw-plane.

5.2 Future work

In Chapter 2 the theoretical basis of the present investigation is described. It would be appropriate if the author could present some theoretical applications of the model for cases when the fracture process zone is influenced by combined normal and shear displacements. Since the author did not have access to any software which could carry out such applications, and further development of the software was not possible within a reasonable period of time,

the theoretical applications have been postponed to the future. Nevertheless, the author wishes to treat the following subjects first.

The behaviour of the specimen during the entire test, i.e. stress and displacement distribution on the fracture surface, formation of secondary cracks and their influence on the measured properties.

Uneven distribution of shear stresses. (This leads to torsion of the specimen around its length axis. Hence, it is necessary to evaluate the influences of the unevenly distributed shear stress on the measured properties.)

Behaviour of structures and the relation between normal and shear displacements occurring in practice.

As far as experimental studies are concerned the author wishes to consider the following subjects.

Improvement of the stiffness of the test arrangement.

Evaluation of the influence of the uneven distributed normal displacement in the beginning of the test on the development of the normal and shear stresses.

Prevention of torsion of the specimen due to unevenly distributed shear.

The study of different types of concrete admixture.

A closer study of the path dependant behaviour of concrete.

Performance of cyclic tests.

Appendix A. Derivation of the instability equations

In this appendix the derivation of the instability equations for the test equipment described in section 3.2 is given. It should be noted that most of the notations used in this appendix are described in section 3.2. Nevertheless, some additional notations will be described as they appear during the derivation.

Assumptions:

The fracture process zone has extended over the whole specimen.

All cross sections remain plane.

Rotation of the cross section A-A (θ_c), see Fig. A.1, will cause a difference (Δw) in deformations between the right and the left side of the fracture process zone. Thus the relation between θ_c and Δw is as follows:

$$2\theta_c = \frac{\Delta w}{d_0}$$

2 is due to symmetry.

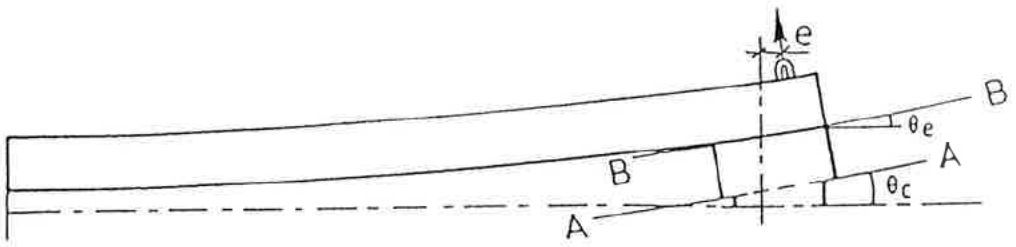

Fig. A1. Notations used in the approximate analysis. See also Fig. 3.6.

The stress at the right and the left side of the fracture process zone is given by the relation:

$$\sigma' = \sigma \pm \frac{1}{2}\Delta w \frac{d\sigma}{dw}$$

where σ is the mean stress in the fracture process zone and $d\sigma/dw$ is the slope of the σ-w curve, see Fig. 3.7.

The uneven distribution of stress in the fracture process zone causes the moment M_c, see Fig. 3.6.

$$M_c = \frac{b_0 d_0^2}{6} \cdot \frac{1}{2} \Delta w \frac{d\sigma}{dw} = \frac{b_0 d_0^3}{6} \theta_c \cdot \frac{d\sigma}{dw} \qquad \text{A.1}$$

The difference between rotations in sections A-A and B-B is due to the bending of the specimen as a beam. The moment which causes this rotation is the mean value of M_e and M_c. Thus:

$$\theta_e - \theta_c = \frac{M_e + M_c}{2} \cdot \frac{h}{2EI} = (M_e + M_c) \cdot \frac{3h}{Ebd^3} \qquad \text{A.2}$$

The rotation θ_e depends on bending of the supporting beam, see Fig. A1, and the extension of the specimen.

$$\theta_e = \frac{1}{S_{rm}} (\sigma b_0 d_0 e - M_e) + \frac{1}{L} \left(\frac{\sigma b_0 d_0 h}{2bdE} + \frac{w}{2} \right) \qquad \text{A.3}$$

The centre-line of the specimen is displaced by distance (a), see Fig. A.2, due to the rotations θ_e and θ_c.

$$a = \frac{\theta_e + \theta_c}{2} \cdot \frac{h}{2}$$

The displacement (a) causes a difference between M_c and M_e.

$$M_e - M_c = \sigma b_0 d_0 a$$

Inserting the expression for (a) gives

$$M_e - M_c = \sigma b_0 d_0 \cdot \frac{\theta_e + \theta_c}{2} \cdot \frac{h}{2} \qquad \text{A.4}$$

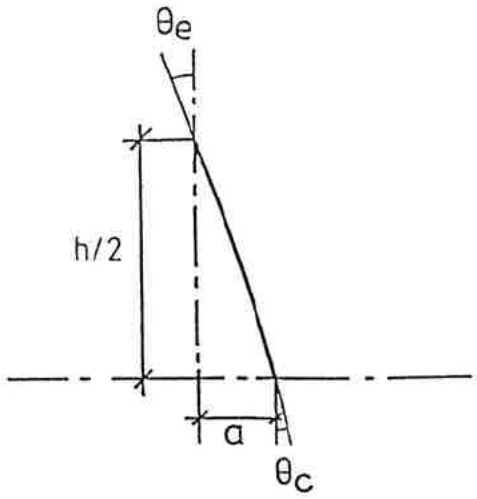

Fig. A2. Displacement of the centre-line.

Equations A.1 and A.2 give

$$\theta_c = M_c \frac{6}{b_0 d_0^3} \cdot \frac{dw}{d\sigma} \qquad \text{A.5}$$

$$\theta_e = (M_e + M_c) \cdot \frac{3h}{Ebd^3} + M_c \cdot \frac{6}{b_0 d_0^3} \cdot \frac{dw}{d\sigma} \qquad \text{A.6}$$

Equations A.3 and A.6 give

$$M_e \left(\frac{1}{S_{rm}} + \frac{3h}{Ebd^3} \right) + M_c \left(\frac{6}{b_0 d_0^3} \cdot \frac{dw}{d\sigma} + \frac{3h}{Ebd^3} \right) = \frac{\sigma b_0 d_0 e}{S_{rm}} + \frac{h}{2L} \left(\frac{\sigma b_0 d_0}{Ebd} + \frac{w}{h} \right) \qquad \text{A.7}$$

Equations A.4, A.5 and A.6 give

$$M_e\left(\frac{2}{\sigma b_0 d_0 h}-\frac{3h}{2Ebd^3}\right)=M_c\left(\frac{2}{\sigma b_0 d_0 h}+\frac{6}{b_0 d_0^{\,3}}\cdot\frac{dw}{d\sigma}+\frac{3h}{2Ebd^3}\right) \qquad \text{A.8}$$

Reshaping of A.7 and A.8 give

$$M_e\left(\frac{1}{S_{rm}}+\frac{1}{2S_{rs}}\right)+M_c\left(\frac{1}{2I_0\dfrac{d\sigma}{dw}}+\frac{1}{2S_{rs}}\right)=\frac{eA_0\sigma}{S_{rm}}+\frac{1}{2L}\left(\frac{2A_0\sigma}{S_{ns}}+w\right) \qquad \text{A.9}$$

$$M_e\left(\frac{2}{hA_0\sigma}-\frac{1}{4S_{rs}}\right)=M_c\left(\frac{2}{hA_0\sigma}+\frac{1}{2I_0\dfrac{d\sigma}{dw}}+\frac{1}{4S_{rs}}\right) \qquad \text{A.10}$$

where

$$A_0 = b_0 d_0$$

$$I_0 = \frac{b_0 d_0^{\,3}}{12}$$

$$I = \frac{bd^3}{12}$$

$$S_{ns} = \frac{2EA}{h}$$

$$S_{rs} = \frac{2EI}{h}$$

Finally equation A.1 gives

$$\Delta w=\frac{12M_c}{b_0 d_0^2}\cdot\frac{1}{\dfrac{d\sigma}{dw}} \qquad \text{A.11}$$

Appendix B. Equations for determination of the aggregate-matrix contact surfaces, A_x and A_y

In this appendix, equations for A_x and A_y are given. The derivations of the equations can be find in Walraven (1979 and 1980).

Case A: $\delta < w$

$$A_x = \int_{\frac{w^2+\delta^2}{\delta}}^{D_{max}} p_k \cdot \frac{4}{\pi} \cdot F(\frac{D}{D_{max}}) \cdot G_2(\delta,w,D) \cdot dD$$

$$A_y = \int_{\frac{w^2+\delta^2}{\delta}}^{D_{max}} p_k \cdot \frac{4}{\pi} \cdot F(\frac{D}{D_{max}}) \cdot G_1(\delta,w,D) \cdot dD$$

Case B: $\delta > w$

$$A_x = \int_{2w}^{\frac{w^2+\delta^2}{w}} p_k \cdot \frac{4}{\pi} \cdot F(\frac{D}{D_{max}}) \cdot G_4(\delta,w,D) \cdot dD + \int_{\frac{w^2+\delta^2}{w}}^{D_{max}} p_k \cdot \frac{4}{\pi} \cdot F(\frac{D}{D_{max}}) \cdot G_2(\delta,w,D) \cdot dD$$

$$A_y = \int_{2w}^{\frac{w^2+\delta^2}{w}} p_k \cdot \frac{4}{\pi} \cdot F(\frac{D}{D_{max}}) \cdot G_3(\delta,w,D) \cdot dD + \int_{\frac{w^2+\delta^2}{w}}^{D_{max}} p_k \cdot \frac{4}{\pi} \cdot F(\frac{D}{D_{max}}) \cdot G_1(\delta,w,D) \cdot dD$$

with

$$G_1(\delta,w,D) = D^{-3}\left(\sqrt{D^2-(w^2+\delta^2)}\cdot\frac{\delta}{\sqrt{w^2+\delta^2}}\cdot u_{max} - wu_{max} - u_{max}^2\right)$$

$$G_2(\delta,w,D) = D^{-3}\left[\left(\delta - \sqrt{D^2-(w^2+\delta^2)}\cdot\frac{\delta}{\sqrt{w^2+\delta^2}}\right)u_{max}\right.$$

$$+ (u_{max}+w)\cdot\sqrt{\frac{1}{4}D^2-(w+u_{max})^2} - w\sqrt{\frac{1}{4}D^2-w^2}$$

$$\left. + \frac{1}{4}D^2\arcsin\frac{2(w+u_{max})}{D} - \frac{1}{4}D^2\arcsin\frac{2w}{D}\right]$$

$$G_3 = D^{-3}\left(\frac{1}{2}D-w\right)^2$$

$$G_4 = D^{-3}\left(\frac{\pi}{8}D^2 - w\sqrt{\frac{1}{4}D^2-w^2} - \frac{D^2}{4}\arcsin\frac{2w}{D}\right)$$

$$F\left(\frac{D}{D_{max}}\right) = 0.727\left(\frac{D}{D_{max}}\right)^{0.5} - \left(\frac{D}{D_{max}}\right)^2 + 0.144\left(\frac{D}{D_{max}}\right)^4$$

$$+ 0.036\left(\frac{D}{D_{max}}\right)^6 + 0.016\left(\frac{D}{D_{max}}\right)^8 + 0.010\left(\frac{D}{D_{max}}\right)^{10}$$

$$u_{max} = \frac{-w(w^2+\delta^2) + \sqrt{w^2(w^2+\delta^2) - (w^2+\delta^2)[(w^2+\delta^2)^2 - \delta^2 D^2]}}{2(w^2-\delta^2)}$$

p_k = volume aggregate/volume concrete.
D = size of aggregate.
D_{max} = maximum aggregate size.

Appendix C. Differentiation of the stress - displacement relationships

Differentiation of the expressions in 4.3 with variable β gives:

$$C_{11} = \frac{\partial \sigma}{\partial w} = 2.8\left(-40e^{-40w} + \frac{37.5\beta^3}{w} \cdot e^{-5\beta^3} \cdot \arctan\delta \right)$$

$$C_{12} = \frac{\partial \sigma}{\partial \delta} = -2.8e^{-5\beta^3}\left(\frac{37.5}{2} \cdot \frac{\beta^5}{w^2} \cdot \arctan\delta + \frac{2.5}{1+\delta^2} \right)$$

$$C_{21} = \frac{\partial \tau}{\partial w} = -10e^{-3.6\beta^{1.4}}\left(\arctan\left(\frac{\delta}{w}\right)^2 \right)^{0.5} \cdot \left(\frac{5.04\beta^{1.4}}{w} + \frac{w\delta^2}{w^4+\delta^4} \cdot \frac{1}{\arctan\left(\frac{\delta}{w}\right)^2} \right)$$

$$C_{22} = \frac{\partial \tau}{\partial \delta} = 10e^{-3.6\beta^{1.4}}\left(\arctan\left(\frac{\delta}{w}\right)^2 \right)^{0.5} \cdot \left(\frac{2.52\beta^{3.4}}{w^2} + \frac{w^2\delta}{w^4+\delta^4} \cdot \frac{1}{\arctan\left(\frac{\delta}{w}\right)^2} \right)$$

In the case of constant parabola paths (β constant) both C_{12} and C_{21} are zero while the remaining elements are as follows:

$$C_{11} = 2.8\left(-40e^{-40w} - 5e^{-5\beta^3} \frac{w\beta^2}{\beta^4+w^4} \right)$$

$$C_{22} = 10e^{-3.6\beta^{1.4}} \frac{\beta^2}{2(\beta^4+\delta^2)\left(\arctan\frac{\delta}{\beta^2}\right)^{0.5}}$$

References

Alexanderson, J. (1982) Proportionering av betong, in **Betong Handbok**, Material, AB Svensk Byggtjänst, Sweden, pp. 544-567.

Bažant, Z.P. and Gambarova, P. (1980) Rough cracks in reinforced concrete. **Journal of the Structural Division**, No. ST4, April, pp. 819-842.

Bäcklund, J. (1982) **Brottmekanik.** Report 82-18, Department of Aeronautical Structures and Materials, The Royal Institute of Technology, Stockholm, Sweden.

Carlsson, J. (1976) **Brottmekanik.** Ingenjörsförlaget AB, Sweden.

Erdogan, F. and Sih, G.C. (1963) On the crack extension in plates under plane loading and transverse shear. **Journal of Basic Engineering.**, 85, 519-527.

Fagerlund, G. (1982) Struktur, in **Betong Handbok**, Material, AB Svensk Byggtjänst, Sweden, pp. 171-197.

Gustafsson, P.J. (1985) **Fracture Mechanics Studies of Non-Yielding Materials Like Concrete.** Report TVBM-1007, Division of Building Materials, Lund Institute of Technology, Lund,Sweden.

Hassanzadeh, M., Hillerborg, A. and Zhou, F.P. (1987) Tests of material properties in mixed mode I and II, in **Fracture of Concrete and Rock** (eds S.P. Shah and S.E. Swartz), Proc. SEM-RILEM International Conference, Houston, Texas, pp. 138-149.

Hellan, K. (1984) **Introduction to Fracture Mechanics.** McGraw-Hill Inc., U.S.A.

Hillerborg, A. (1984) **Kompendium i Byggnadsmateriallära FK**, Division of Building Materials, Lund Institute of Technology, Lund, Sweden.

Hillerborg, A. (1989a) Stability problems in fracture mechanics testing, in **Fracture of Concrete and Rock** (eds S.P. Shah, S.E.Swartz and B. Barr), Elsevier Applied Science, pp. 369-378.

Hillerborg, A. (1989b) Mixed-mode fracture in concrete, in **Proceedings of the Seventh International Conference on Fracture**, Houston, Texas, March 20-24, pp. 2259-2268.

Hordijk, D.A., Reinhardt, H.W. and Cornelissen, H.A. (1987) Fracture mechanics parameters of concrete from uniaxial tensile tests as influenced by specimen length, in **Fracture of Concrete and Rock** (eds S.P. Shah and S.E. Swartz), Proc. SEM-RILEM International Conference, Houston, Texas, pp. 138-149.

Hordijk, D.A., van Mier, J.G.M. and Reinhardt, H.W. (1989) Material properties, in **Fracture Mechanics of Concrete Structures,** RILEM Report, (ed L. Elfgren), Chapman and Hall,pp. 67-121.

Ingraffea, A.R. and Saouma, V. (1985) Numerical modelling of discrete crack propagation in reinforced and plain concrete, in **Fracture Mechanics of Concrete** (eds G.C. Sih and A. Ditommaso), Martinus Nijhoff publishers, pp. 171-225.

Mindess, S. (1983) The application of fracture mechanics to cement and concrete, in **Fracture Mechanics of Concrete** (ed F. Wittmann), Elsevier, pp. 1-25.

Modéer, M. (1979) **A Fracture Mechanics Approach to Failure Analyses of Concrete Materials.** Report TVBM-1001, Division of Building Materials, Lund Institute of Technology, Lund, Sweden.

Nooru-Mohamed, M.B. and van Mier, J.G.M. (1989) Fracture of concrete under mixed-mode loading, in **Fracture of Concrete and Rock - Recent Developments** (eds S.P. Shah, S.E. Swartz and B. Barr), Elsevier Science Publishers, London/ New York, pp. 458-467.

Nooru-Mohamed, M.B. and van Mier, J.G.M. (1991) Size effects in mixed-mode fracture of concrete, in **Fracture Processes in Concrete, Rock and Ceramics** (eds J.G.M. van Mier, J.G. Rots and A. Bakker), Proceedings of the International RILEM/ESIS Conference, E & FN SPON, pp. 461-471.

Ouchterlony, F. (1981) **Review of Fracture Toughness Testing of Rock.** Swedish Detonic Research Foundation, Stockholm, Sweden.

Petersson, P.E. (1981) **Crack Growth and Development of Fracture Zones in Plain Concrete and Similar Materials.** Report TVBM-1006, Division of Building Materials, Lund Institute of Technology, Lund, Sweden.

Raiss, M.E., Dougill, J.W. and Newman, J.B. (1990) Development of fracture process zone in concrete. **Magazine of Concrete Research.**, 42, 193-202.

Reinhardt, H.W., Cornelissen, H.A. and Hordijk, D.A. (1987) Mixed mode fracture tests on concrete, in **Fracture of Concrete and Rock** (eds S.P. Shah and S.E. Swartz), Proc. SEM-RILEM International Conference, Houston, Texas,pp. 324-337.

Remmel, G. (1990) Study on tensile fracture behaviour by means of bending tests on high-strength concrete. **Darmstadt Concrete.**, 5, 155-162.

RILEM-REPORT (1989) **Fracture Mechanics of Concrete.** (ed L. Elfgren), Chapman and Hall.

Rots, J.G. (1988) **Computational Modelling of Concrete Fracture.** Delft University of Technology, Department of Civil Engineering, Delft, The Netherlands.

Smadi, M. and Slate, F.O. (1989) Microcracking of high and normal strength concrete under short- and long-term loadings. **ACI Materials Journal.**, March-April, 117-127.

van Mier, J.G.M. and Nooru-Mohamed, M.B. (1988) **Geometrical and Structural Aspects of Concrete Fracture.** Stevin Laboratory, Delft University of Technology, Delft, The Netherlands.

van Mier, J.G.M., Nooru-Mohamed, M.B. and Schlangen, E. (1989) Experimental analysis of mixed mode I and II behaviour of concrete, in **Analysis of Concrete Structures by Fracture Mechanics.** (eds L. Elfgren and S.P. Shah), Proceedings of the International RILEM Workshop, Chapman and Hall, pp. 32-43.

van Mier, J.G.M (1991) Mode I fracture of concrete: Discontinuous crack growth and crack interface grain bridging. **Cement and Concrete Research.**, 21, 1-15.

Walraven, J.C. (1978) **Mechanisms of Shear Transfer in Cracks in Concrete: A survey of literature.** Report 5-78-12, Stevin Laboratory, Delft University of Technology, Delft, The Netherlands.

Walraven, J.C. (1979) **Experiments on Shear Transfer in Cracks in Concrete: Analysis of results.** Report 5-79-10, Stevin Laboratory, Delft University of Technology, Delft, The Netherlands.

Walraven, J.C. (1980) **Aggregate Interlock: A theoretical and experimental analysis.** Delft University press, Delft University of Technology, Delft, The Netherlands.

Wolinsky, S., Hordijk, D.A., Reinhardt, H.W. and Cornelissen, H.A. (1987) Influence of aggregate size on fracture mechanics parameters of concrete. **The International Journal of Cement Composites and Lightweight Concrete.**, 9, 2, 95-103.

Zhou, F.P. (1988) **Tensile Fracture Behaviour and Structural Response of Cementitious Materials.** Report TVBM-1008, Division of Building Materials, Lund Institute of Technology, Lund, Sweden.